

RAPID TWO-PHOTON HOLOGRAPHIC SCAN MICROSCOPY  
WITH INDIVIDUAL QUANTUM DOTS  
AND ITS APPLICATIONS IN BIOLOGICAL SAMPLES

BY

RUOBING ZHANG

DISSERTATION

Submitted in partial fulfillment of the requirements  
for the degree of Doctor of Philosophy in Biophysics and Computational Biology  
in the Graduate College of the  
University of Illinois at Urbana-Champaign, 2010

Urbana, Illinois

Doctoral Committee:

Professor Paul R. Selvin, Chair, Director of Research  
Professor Robert B. Gennis  
Assistant Professor Maria Spies  
Assistant Professor Yingxiao Wang

UMI Number: 3455905

All rights reserved

INFORMATION TO ALL USERS

The quality of this reproduction is dependent upon the quality of the copy submitted.

In the unlikely event that the author did not send a complete manuscript and there are missing pages, these will be noted. Also, if material had to be removed, a note will indicate the deletion.



UMI 3455905

Copyright 2011 by ProQuest LLC.

All rights reserved. This edition of the work is protected against unauthorized copying under Title 17, United States Code.



ProQuest LLC  
789 East Eisenhower Parkway  
P.O. Box 1346  
Ann Arbor, MI 48106-1346

# Abstract

Two-photon (2P) excited fluorescence microscopy is particularly advantageous for imaging biological specimens since it offers reduced scattering, deep sample penetration, and intrinsic confocality when excited with point excitation. Here we report the first 2-photon microscopy of individual quantum dots in biological environment. Near-complete suppression of blinking and of photobleaching was achieved. Three schemes of 2-photon excitation are shown: 1) widefield, 2) diffraction-limited spot scanning with a single rastered spot, or 3) a multi-point excitation scheme employing a  $9 \times 9$  matrix hologram that increases the scan rate by 80 fold. An array detector (EMCCD camera) was also used as a detector for 2-photon scanning microscopy, providing faster whole image acquisition and superior detection capabilities compared to a conventional single point detector (a PMT). Wide-field 2-photon excitation was used to resolve the step size of individual Myosin V motors *in vitro*, indicating the 2-photon field does not damage the ATPase of myosin. We validated the helical spatial arrangement of LamB receptors on live *E. coli* cells with the 2-photon fast hologram scan microscopy. The endocytosis of epidermal growth factor (EGF) receptors in breast cancer cells was verified by imaging quantum dot labeled fixed cell sample with the technique. The strong colocalization of EGFR and HGFR (c-Met) in the same clusters in EGF/HGF stimulated breast cancer cell was also revealed. Moreover, we obtained 3D localization at less than 3 nanometer accuracy and fast 3D imaging at confocal resolution, while doing no harm to the cell samples.

# Acknowledgements

At this point of the dissertation, I would like to express my sincere thanks and appreciation to the people that helped me in my Ph.D. journey as well as in my whole past life, without whom I can never have my achievement today.

First of all I want to sincerely thank my Ph.D. advisor, Prof. Paul Selvin, for his all-through support during my time in his lab. He is not only knowledgeable and talented but also patient and understanding. I appreciate very much the opportunity he gave me to pursue my academic interest.

I then would like to thank all the people who work, or used to work, together with me in Selvin's lab. They are great colleagues in work and warm friends in life. My appreciation goes to all of them. Especially, I would like to thank Eli Rothenberg, who generously helped me in the project we worked on in the past year, from raising inspiring ideas and teaching me hands-on experimental skills. I would also like to thank Paul Simonson for instructing me to use PhILM.

I also would like to thank University of Illinois, where I have had a great part of my life and really enjoyed the world-class academic environment. Special thanks go to Prof. Yingxiao Wang, Prof. Robert Gennis, Prof. Maria Spies for supporting me as my committee. I also thank Peking University, where I spent my youth and started my academic road.

At the end I want to give my immense gratitude to my father and my mother, who initially aroused my curiosity in this universe and granted me the intelligence to understand it. They are my first and best mentors and friends. I will never be the person as who I am today without them.

# Table of Contents

Chapter I	Introduction.....	1
1.1	The Basics of Fluorescence.....	1
1.2	Single-molecule Fluorescence Techniques and Fluorescence Microscopy.....	3
1.3	Fluorescence Imaging with One Nanometer Accuracy (FIONA).....	7
1.4	Two-photon Excitation Microscopy.....	9
1.5	Membrane Receptors Direct Viral Targeting on Host Cells.....	11
1.6	Cancer and Growth Factor Receptors.....	13
1.7	Figures.....	15
Chapter II	Two-photon Excitation of Quantum Dots Under Ambient Condition...22	
2.1	Quantum Dots.....	23
2.2	Individual Quantum Dots Imaged with 2-Photon Excitation in Aqueous Solutions.....	25
2.3	Suppression of Emission Intermittence of Quantum Dots.....	27
2.4	Myosin V Stepping Assay with Wide-field 2-Photon Excitation.....	28
2.5	Materials and Methods.....	29
2.6	Figures.....	32
Chapter III	Fast Two-photon 3D Scan Microscopy with Holographic Excitation..42	
3.1	Configurations of the Microscopy.....	43
3.2	Excitation: the Holographic Matrix.....	45
3.3	Acquisition: EMCCD vs. PMT.....	46
3.4	Materials and Methods.....	50
3.5	Figures and Tables.....	53
Chapter IV	Imaging of LamB Receptors on <i>E.coli</i> .....	62
4.1	Introduction.....	62

4.2	Spatial Characteristics of LamB Receptors.....	63
4.3	Materials and Methods.....	64
4.4	Figures.....	66
Chapter V EGFR and c-Met in Human Breast Cancer Cells.....		69
5.1	Introduction.....	69
5.2	Imaging Individual QD-labeled Receptors.....	71
5.3	2P QD Hologram Scan Microscopy in Combination with PhILM.....	72
5.4	Endocytosis of EGFR.....	76
5.5	Colocalization of EGFR and c-Met in Clusters.....	77
5.6	Materials and Methods.....	79
5.7	Figures and Tables.....	81
Chapter VI FIONA in 3D Space.....		92
6.1	Introduction.....	92
6.2	Three-dimensional FIONA via 2-photon Sectioning.....	94
6.3	Discussion.....	95
6.4	Methods.....	97
6.5	Figures.....	98
References.....		106

# Chapter I

## Introduction

Fluorescence imaging has been one of the most powerful techniques to reveal the secrets of the micro biological world as well as in chemistry, physics and engineering. With a many varieties, it is widely applied on various biological samples, from a single protein or DNA molecule to whole cells to live tissues as long as they can be labeled with fluorophores. With fluorescence techniques, scientists are able to characterize the motion of motor proteins [1-4], investigate the interaction between protein and DNA molecules [5-7], watch the cells' response to the environmental mechanical stimulation [8, 9], or localize the cancer tumors among healthy tissues [10], etc.. In the past decades, a variety of fluorescence imaging techniques at single molecule level have been greatly developed, and reached nanometer accuracy of localization and super resolution below the diffraction limit. The thesis focuses on the development of an innovative 3D fluorescence imaging technique with two-photon parallel excitation, and its applications in cell biology research.

### 1.1 The Basics of Fluorescence

Fluorescence is the emission of photons by the decay of orbital electrons from the higher energy quantum states to their ground states. The electrons were

usually excited to the higher quantum states by the absorption of light or other electromagnetic radiation at another wavelength. In most cases, the excitation wavelength is shorter than the emission wavelength.

Fluorescence is one kind of luminescence, while the other kind is phosphorescence. Fluorescence is defined as a molecule relaxes to the ground state from the excited singlet state and emits a photon, while phosphorescence refers to the case that the excited molecule first takes an intersystem crossing (ISC), flipping from the singlet state to the triplet state which has lower energy, and then relaxes to the ground state and emits a photon.

The Jablonski diagram (Fig. 1.1) shows all processes that may occur in the luminescence emission. Internal conversion (IC) is the radiationless transition between two electronic states with the same multiplicity. The lifetime of fluorescence, which is defined as the average time that a molecule remains in the excited singlet state before decaying to the ground state, is usually  $10^{-9}$  -  $10^{-8}$  second. In contrast, phosphorescence lifetime, referring the time an excited molecule stays in the triplet state, is much longer, ranging from  $10^{-3}$  to 1 second.

Fluorescence offers scientists a very sensitive way to detect the signals from the physical, chemical or biological samples. With modern technical advances in optics (e.g. high numerical aperture objectives) and electronic devices (e.g. CCD cameras with electron multiplying gain), the detection of fluorescence signal can be performed at very low concentration of sample molecules – in fact, single molecule level. The breakthrough in single molecule fluorescence detection and imaging opens a new world of directly investigating

the behaviors of individual biomacromolecules as well as the teamwork among them, also known as single molecule biophysics.

## 1.2 Single-molecule Fluorescence Techniques and Fluorescence Microscopy

Ever since the pioneering work done by Hirschfeld at 1976 [11], Moerner *et al* at 1989 [12], Orrit *et al* [13] and Shera *et al* at 1990 [14], single-molecule fluorescence techniques have been widely developed and profoundly changed the researches in biological topics. Many methods were invented to characterize the behavior and interactions of individual molecules in various aspects. Fluorescence Imaging at One Nanometer Accuracy (FIONA) uses the Gaussian fitting of the point spread function (PSF) of pixelated fluorescence spot on the charge-coupled device (CCD) to localize a single fluorophore down to one nanometer accuracy and, when the fluorophore labels a motor protein such as myosin V, myosin VI and kinesin, to characterize the motion of the molecular motors [1-4]. With single-molecule FRET, people are able to measure the distance and the distance change between two chosen labeling fluorophores by monitoring the (change of) relative emission intensity of them, and thus can reveal the interaction of two individual molecules (e.g. DNA and the helicase) or the conformational change of one single molecule [5-7]. Single molecule fluorescence detection provides direct information from each individual molecule and the statistical distribution of an assembly of molecules. It reveals the characters and detailed processes of the microscopic components that are

covered under the macroscopic behavior of the entirety in a conventional ensemble measurement [15]. This is very critical in understanding heterogeneous systems such as all biological samples [16].

In another direction, people have also been able to extend the accurate localization of one single molecule to tons of densely labeling fluorophores and therefore to reach super resolution that is below the diffraction limit. So far the super-resolution imaging techniques based on single-molecule fluorescence include Photoactivation Localization Microscopy (PALM) [17, 18], Stochastic Optical Reconstruction Microscopy (STORM) [19-21] and Photobleaching and Intermittency Localization Microscopy (PhILM) [22]. The principle is the accumulation of stochastic localization events. Researchers recorded a large amount of fluorescent imaging data, in which fluorophores are on or off in one image or another. The switching on and off of the fluorophores are either completely intrinsic (PhILM) or controllable by the researcher to some extent (STORM). Then through image math, individual fluorescent spots can be isolated from adjacent ones and localized to nanometer (or tens of nanometer) accuracies. The aggregate of these accurately localized individual spots will delineate the microscopic sample labeled by the fluorophores.

Fluorescence microscopy is a large class of imaging techniques. Generally, the samples are pre-labeled with fluorophores, e.g. organic dyes, fluorescent proteins, fluorescent beads, or quantum dots. Then in most cases, a laser is used to excite the fluorophores to emit fluorescence. The emission is recorded by a photo-sensitive device such as a CCD, a photomultiplier tube or an

avalanche photodiode, or directly watched by eyes. Most of the conventional microscopes use wide-field excitation, also known as epifluorescence microscopes, which have a collimated laser beam illuminating a part of the sample and excite all fluorophores inside the illumination area. Naturally, this non-discriminative excitation method generates high background, especially for cell samples, and may cause photo-damage to the areas that is not in focus or under imaging. Apparently, with epifluorescence microscopy, it is hard to differentiate single molecule fluorescence signals from the ensemble background.

In the past decade, the total internal reflection fluorescence microscopy (TIRFM) revolutionized the fluorescence imaging and makes single molecule fluorescence detection possible and convenient [23]. In classic optics, when a ray of light, travelling from a medium with a larger index of refraction to a medium with a smaller index of refraction, hits the boundary of the two media at an incident angle larger than a particular critical angle, all the light will be reflected back to the first medium and no light can pass through the media boundary, which is named total internal reflection (TIR). The critical angle can be determined by

$$\theta_c = \arcsin\left(\frac{n_2}{n_1}\right) \quad (1.1)$$

where  $n_1$  is the higher index of refraction of the medium that the light travels in, while  $n_2$  is lower index of refraction of the second medium.

However, the modern optics shows that under TIR condition, an evanescent wave would propagate across the boundary surface (Fig. 1.2). The

intensity of the penetrating evanescent wave at a certain height  $z$  from the interface is given by

$$I(z) = I_0 e^{-z/d} \quad (1.2)$$

where  $I_0$  is the original intensity right on the interface and  $d$  is the penetration depth, which could be determined by:

$$d = \frac{\lambda * (n_2^2 \sin^2 \theta - n_1^2)^{-0.5}}{2\pi} \quad (1.3)$$

where  $\lambda$  is the wavelength of the light,  $n_1$  and  $n_2$  are the refractive indices of the media and  $\theta$  is the incident angle.

The penetration depth is generally around 100 – 200 nm, e.g. the green laser as a penetration depth of 150 nm [24]. In this case, only those fluorophores within the range of the penetration depth will be excited and emit photons. Thus in a much diluted sample, people can easily realize single molecule imaging by laying down a discrete mono-molecular layer onto the surface. Moreover, the limited excitation also greatly reduces the background from the bulk solution.

Figure 1.3 illustrates two types of TIRFM, the prism-type and the objective-type, both of which are widely used in modern single molecule imaging as well as other microscopic experiments. The prism-type TIRFM is reported to have higher signal to noise ratio (SNR) [25], but the objective TIRFM, realized with high numerical aperture (NA) objective, also has much superior SNR to conventional wide-field microscopes. The advantage of objective-type TIRFM lies in the better detection efficiency and the ease to set up and use.

### 1.3 Fluorescence Imaging with One Nanometer Accuracy (FIONA)

One of the most influential advancements in single molecule microscopy in the past decade is the Fluorescence Imaging with One Nanometer Accuracy (FIONA). This potent technique opens the era of the accurate fluorescence imaging beyond the diffraction limit. It is not only the central experimental method for biomolecular tracking, but also the foundation of many new super-resolution microscopies which rely on the accumulation of stochastic localizations of individual fluorophores (e.g. SHRIMP [26], PALM [17, 18], STORM [19-21], PhILM [22]) or colocalization of multi-color fluorophores (e.g. SHREC [27]).

Diffraction limit is the fundamental end line of the maximal resolution of any classical optical system, which is attributed to diffraction. The full width at half maximum (FWHM) of a diffraction-limited spot is  $0.61\lambda/NA$ , where NA is the numerical aperture of the objective. For the widely used high NA oil immersion objective, the NA is 1.45. So the diffraction-limited FWHM is  $\lambda/2.38$ , and in routine estimation it can be approximated as  $\sim\lambda/2$ . For example, when the emission is at 600 nm, the FWHM of the diffraction-limited fluorescence spot would be about 300 nm. That is to say, no matter how hard people image the spot – reducing the background, minimizing the drift, or increasing the excitation power – they cannot get resolution any better than the diffraction-limited FWHM,  $\sim 300$  nm, with the current optical elements. This limit remained as the end line for scientists to get more accurate images in the past decades.

However, FIONA is capable of breaking this limitation. It has been well known that the intensity vs. spatial coordinate distribution follows the Airy pattern,

which is very well approximated by a 2D Gaussian function. So, the point spread function of a fluorescence spot in a pixelated image can be fitted into a particular 2D Gaussian distribution. Mathematically, the center of this Gaussian distribution can be determined with surprisingly higher accuracy. Therefore, the position of the fluorescence spot, represented by the center of the PSF, can be localized to an amazingly high accuracy, easily reaching one nanometer (Fig. 1.4) [1, 28, 29]. The accuracy is defined as the standard error of the mean of the Gaussian distribution ( $\sigma_{\mu}$ ), and is given by:

$$\sigma_{\mu_i} = \sqrt{\frac{s_i^2}{N} + \frac{a^2}{12} + \frac{8\pi s_i^4 b^2}{a^2 N^2}} \quad (1.4)$$

where  $i$  indicates the  $x$  or  $y$  direction,  $s$  is the standard deviation of the Gaussian fit,  $N$  is the total collected photon number,  $a$  is the effective pixel size of the image which equals the CCD pixel size divided by the total magnification of the microscope, and  $b$  is the background noise in the image, defined as the standard deviation of the background intensity. The first term in the equation represents the photon noise, the second term comes from the finite pixel size of the detector, and the last term indicates the error coming from background noise. Obviously, the accuracy will improve as the total photon number increases, which means that brighter fluorescence will bring higher localization accuracy and better resolution.

FIONA has been successfully applied in resolving the stepping modes of motor proteins such as myosin V, myosin VI, kinesin, etc [1-3]. It convincingly proved that the myosins and the kinesins took hand-over-hand walk instead of

inchworm motion. FIONA was also applied on *in vivo* motor protein tracking, showing that the myosins and kinesins, moving on different kinds of tracks, could cooperate between one another to transport the same cargo to its destination [4, 30]. The innovative technique was also extended from 2D to 3D [31] by calibrating the PSF profile of defocused spots at various heights off the focus plane. However, the accuracy in the z direction determined by the defocusing method, is not as satisfying as the x and y accuracies in the focus plane, and will get worse rapidly as the z goes more off the focus, and thus has limited imaging depth. In the thesis, a new, more accurate 3D FIONA method based on 2-photon scan microscopy will be introduced, of which the z direction has similar localization accuracy with x and y.

## 1.4 Two-photon Excitation Microscopy

As it is mentioned above, epifluorescence microscopy does not provide discriminative excitation along the distance perpendicular to the surface, z, and thus creates huge fluorescence background as well as causes unwanted photo-damages. The TIRFM partially solves the problem by limiting the excitation to a thin layer of about 100 – 200 nm above the surface. However, this in turn has intrinsic disadvantage and limitation that the TIRFM cannot image the sample beyond this thin layer. In other words, the TIRF imaging is limited to 2D and incapable of depicting the whole picture of the 3D sample such as most cells and tissues.

In order to do 3D imaging at high depths while keep discriminative excitation, people have developed a variety of techniques. Two-photon (2P) excitation microscopy is one of the most commonly used [32]. The 2P excitation is the excitation of a fluorophore by two photons with lower energy (i.e. smaller frequency and longer wavelength) than required in one photon (1P) excitation. The fluorophore will emit a single photon of which the wavelength is only determined by its intrinsic characters (i.e. the type of the fluorophore, the chemical structure, etc.). That is to say, the emission via 2P excitation is the same as via 1P excitation. The 2P excitation is a one quantum event. Each excitation photon usually carries half of the energy that is needed to excite the fluorophore, so the wavelength for the 2P excitation is roughly double of the wavelength used for 1P excitation. Since the 1P excitation spectra of most fluorophores are 400 – 600 nm, the 2P excitation usually uses laser at 700 – 1000 nm, a.k.a the infrared (IR) range.

Naturally, as the 2P excitation requires two photons to be absorbed by the fluorophore at the same time, the probability of the simultaneous absorption and the following excitation is much lower than in 1P excitation. Therefore, much denser laser power is needed in 2P excitation. Scientists utilized this unique character to create discriminative excitation and reduce background (Fig. 1.5) [32]. Briefly, the laser is focused to a tiny spot, diffraction limited in size, and the power is finely adjusted that only those fluorophores inside this tiny focal volume can be sufficiently excited while all other molecules outside this excitation spot will not. This is the key advantage of 2P excitation in comparison to 1P excitation

which may require additional optical elements (e.g. a pin hole) to reject the out-of-focus emission. Meanwhile, the localized 2P excitation greatly reduces the unwanted photo-damage to the rest of the sample.

However, there are two major drawbacks of 2P excitation. The first is that most organic-based fluorophores that are the major probes to label biological samples have very small 2P absorption cross-sections, as well as poor photostability, so that their brightness and survival time are inadequate to image at single molecule level. The second is that as the excitation is localized in a tiny, diffraction limited spot, researchers have to scan the excitation spot in all three dimensions over quite a long distance with many steps to accomplish a whole picture of the sample, which is extremely slow and time consuming so that this scanning microscopy cannot be applied on imaging relatively dynamic samples such as live cells and live tissues. This thesis will introduce a new scan method, employing alternative acquisition device to conventional detectors, to accelerate the imaging rate by 80 folds or potentially more.

## 1.5 Membrane Receptors Direct Viral Targeting on Host Cells

Targeting and binding on a particular membrane receptor is the first step for a virus to invade a cell [33-35], and holds high specificity for each virus-receptor pair to determine the range of the cell that the virus will seek as a host. Following the attachment are penetration that the virus enters the host cell via acceptor mediated endocytosis or membrane fusion, uncoating of the viral capsid by enzyme-catalyzed degradation, replication of viral genome and proteins and

the assembly of them, and then the release of the new generation of viruses from the host cell. In the aforementioned processes, the receptor binding may affect those subsequent steps of infection. Either directly or through involved pathways, the bound receptors would modulate the structure of the lipid bi-layer membrane, the organization of cytoskeletons and thus affect the viral penetration and transportation processes and viral pathogenesis [33, 36, 37].

The finding and binding of a virus to a receptor on the cell membrane may involve different kinds of viral motion and virus-receptor interactions. Before rigidly bound to a target receptor, the virus may spend a certain amount of time in moving around with weak interaction along the aggregate of receptors [34]. Reports have shown the effect on virus-receptor targeting by the receptor concentration near the virus [34, 36, 38], membrane lipid environment, actin filament arrangement and receptors aggregation, etc.. A very well established model system in virus targeting researches is the *Escherichia coli* bacterium and its virus, bacteriophage  $\lambda$  [39, 40]. Phage  $\lambda$  binds to the maltose pore LamB receptor (lambda receptor) on the *E.coli* membrane [39] and then delivers its genome into the bacterial cell [39-44]. The interaction between the phage  $\lambda$  and the LamB receptor has been extensively studied [39, 40, 43-46]. A former post-doctorate researcher in our lab suggested a model [47] based on his quantitative experiments that the virus' motion in finding the receptor includes three different modes: free diffusion, motion on the surface of the host cells, and attachment. He argued that after the virus approaches a host cell by free diffusion in the aqueous solution and before it is specifically bound to a receptor, the virus would move

along the patterned LamB receptor aggregates on the cell surface, which is dominated by a weak and reversible interaction between the virus and the LamB receptors.

To validate the motion of virus along LamB receptor aggregates with weak interaction between each other was predominant after the virus came to the vicinity of a host cell via free diffusion, the researcher had to compare the virus' movement trajectories and the spatial arrangement of the LamB receptors on *E.coli* membrane [47] (Fig. 1.6). The virus trajectories were shown by tracking the localization of a fluorescently labeled virus in a time-lapse movie via FIONA. In order to reveal the special organization of LamB receptors on *E.coli* cells, the researcher densely labeled the receptors by quantum dots and imaged the cells with a wide-field fluorescence microscope. Apparently, the helical spatial arrangement of the LamB receptors in the epifluorescence image is vague and questionable. In the thesis, clear spatial characteristics of LamB receptors on the surface of *E.coli* cells will be imaged through our new 2-photon quantum dot microscopy.

## 1.6 Cancer and Growth Factor Receptors

Growth factors (GF) are a large family of natural substances that are capable of stimulating cell growth. They are usually small proteins or steroid hormones, and can bind to growth factor receptors on the cell membrane with high specificity and affinity. After the binding occurs, growth factors receptors will be activated and initiate diverse cascades of signal transduction, and lead to

genome replication, cell growth, proliferation and differentiation [48] (Fig. 1.7). As the growth factors play key roles in cell growth, division and apoptosis, it is not surprising that many growth factor receptors have been proved proto-oncogenic and can lead to malignant cell proliferation, i.e. cancer.

Epidermal growth factor receptor (EGFR, or ErbB-1, or HER-1 in human cells) and hepatocyte growth factor receptor (HGFR, or c-Met) are two important growth factors in most mammalian and human cells. The former is commonly seen in epidermal cells and the EGF can be secreted by many extracellular glands. The latter exists in epithelial cells and endothelial cells, while the origin of the HGF is restricted to mesenchymal cells. In breast tissue, abnormal signaling of the both growth factors can facilitate malignant cell growth and promote the occurrence of breast cancer.

After activation via ligand binding, the EGFR and the HGFR may be endocytosed into the cell plasma and function there. Scientists also suggested that they might form homo-clusters or even co-localize in a hetero-clusters. Investigation in the dimerization/oligomerization and transportation of the both receptors will be enlightening for the understanding of breast cancer pathogenesis and therapy. In the thesis, the application of our new-type 3D 2-photon quantum dot microscopy on the EGFRs and HGFRs in breast cancer cells will be described and discussed.

## 1.7 Figures

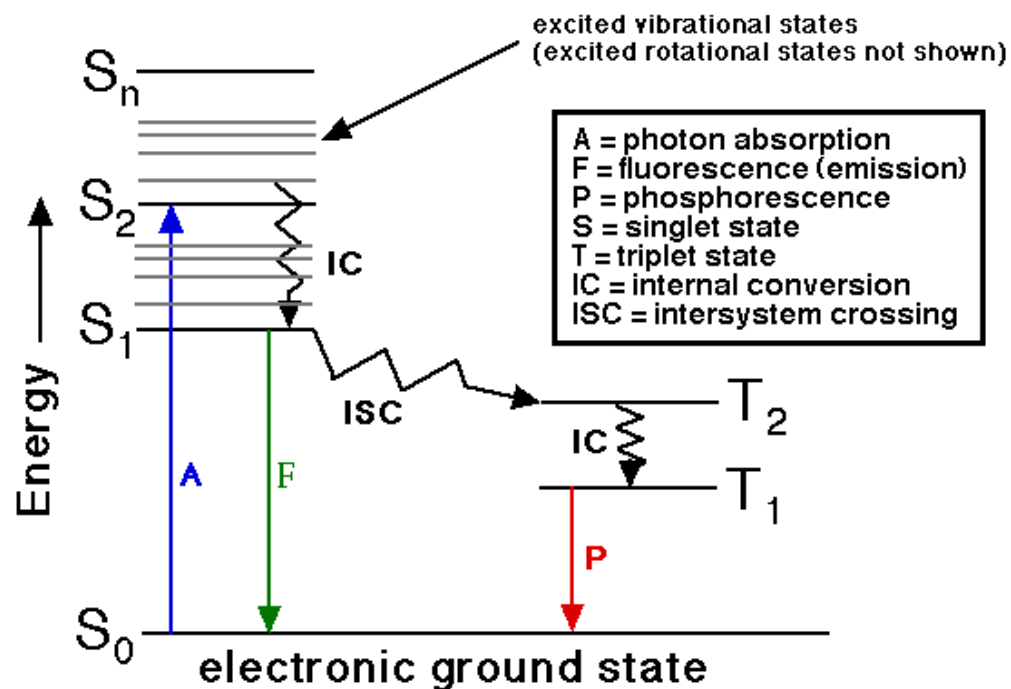


Figure 1.1 | Jablonski diagram of fluorescence and phosphorescence. (Picture from Chemicool.com)

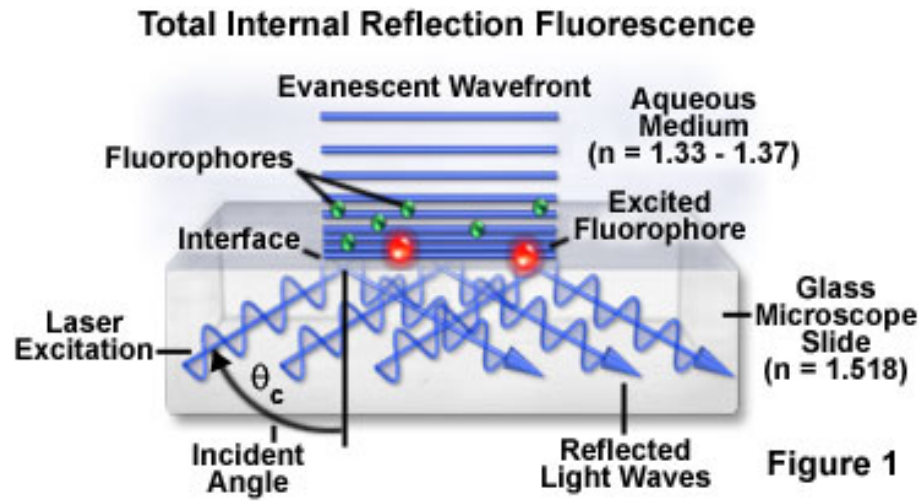


Figure 1.2 | Illustration of total internal reflection excitation. The depth of evanescent wave is usually 100 – 200 nm. (Picture from Microscopyu.com)

### TIRFM Instrument Configurations

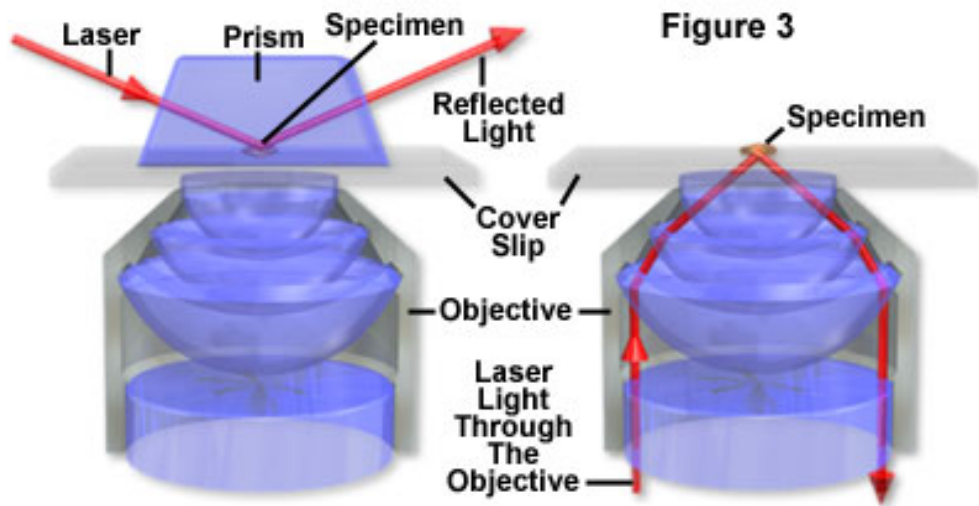


Figure 1.3 | Illustration of total internal reflection fluorescence microscopy (TIRFM). Left, prism-type TIRFM. Right, objective-type TIRFM. (Picture from Olympus.com)

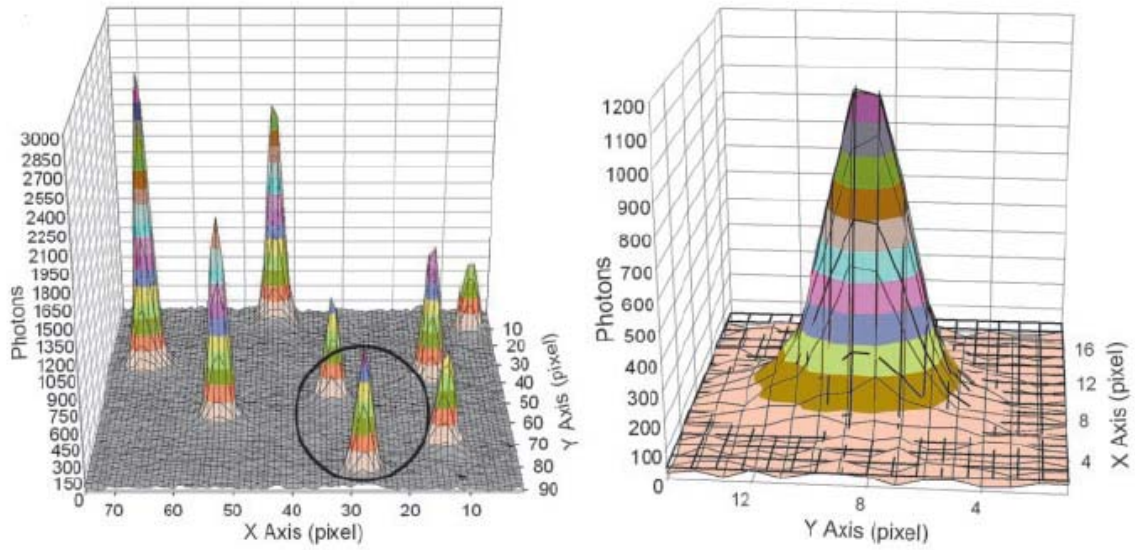
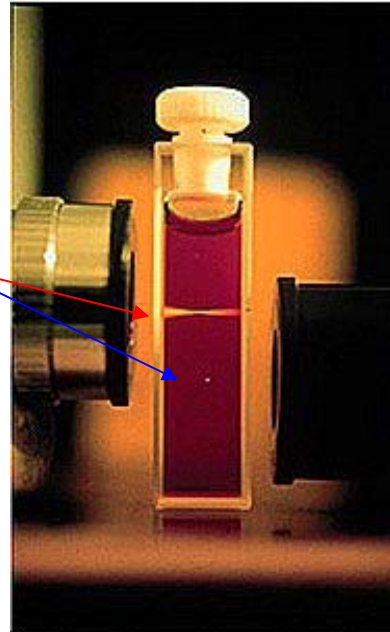
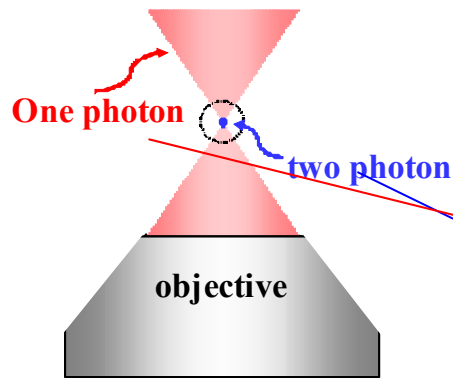


Figure 1.4 | Left, PSFs of several individual Cy3-dyes attached to a coverslip. Right, a Gaussian fit (solid lines) to the PSF circled in the left PSF plot. The center of the Gaussian distribution is determined to be 1.3 nm. The Gaussian fit contains small systematic errors because of the difference between a Gaussian and Airy function.  $\chi^2_r = 1.48 > 1$ .

## 2-photon optical sectioning



- **inherent spatial resolution**

Figure 1.5 | Comparison of one-photon excitation field and two-photon excitation field.

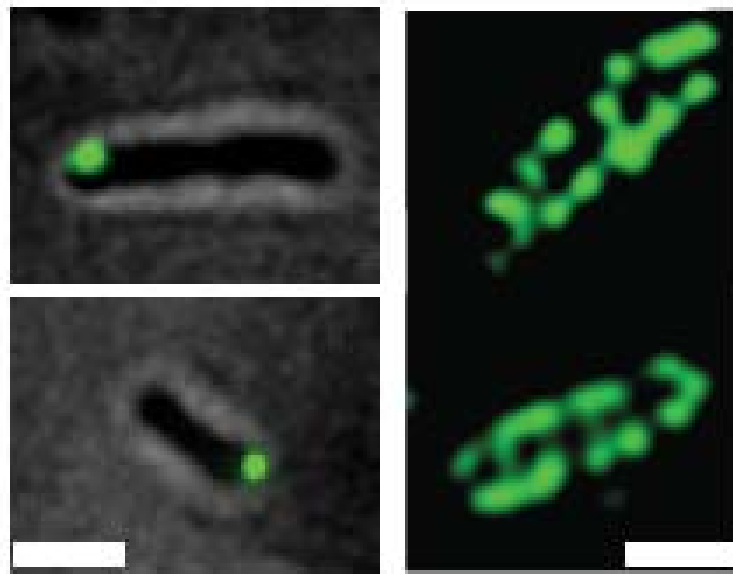


Figure 1.6 | Biotinylated LamB (bio-LamB) receptors labeled with QD655-streptavidin conjugate at different labeling levels. Left, cells labeled at single molecule level, with QD655 at 100 pM. Single LamB receptors were labeled (green spots). Right, the cell labeled at high density of quantum dots of 10nM. LamB receptors were labeled extensively, providing the visualization of the spatial organization of the LamB receptor network (green bands). The spatial pattern of LamB receptors could be bands, rings and helices and combinations thereof. (Scale bar = 2  $\mu\text{m}$ )

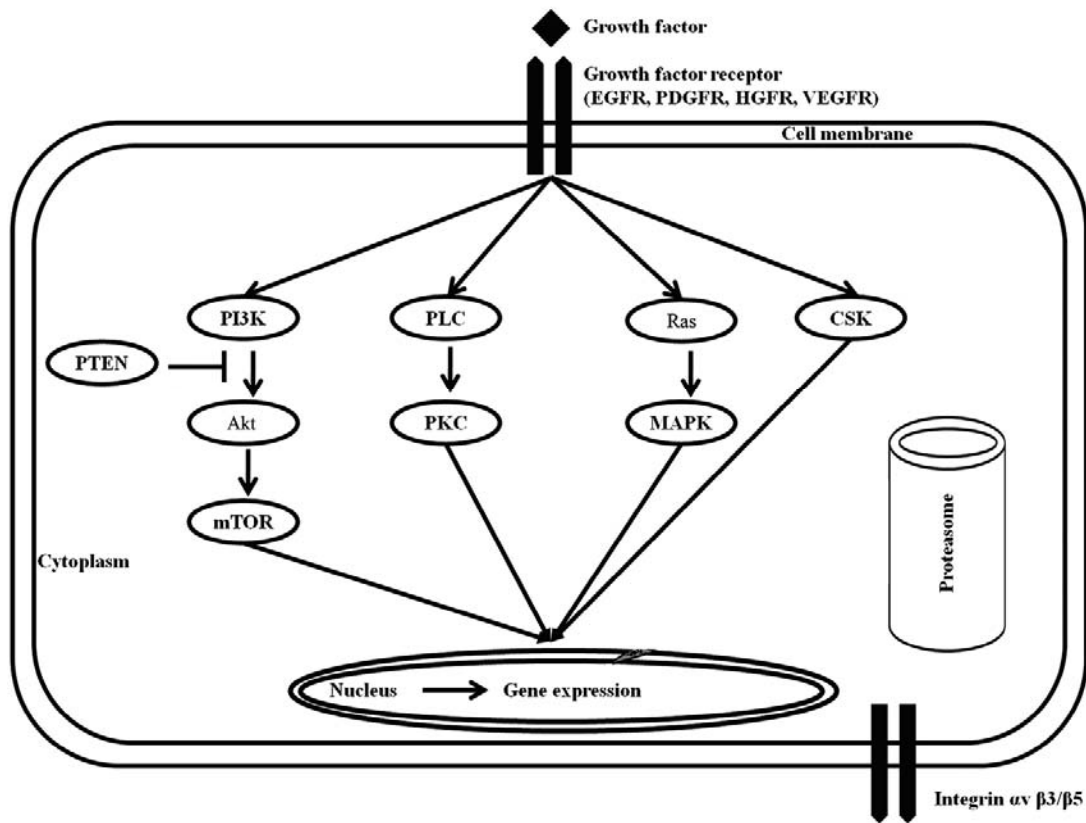


Figure 1.7 | Cascades of signaling pathways of various growth factors. Abbreviations: Akt, v-akt murine thymoma viral oncogene homolog 1; CSK, c-Src kinase; EGFR, epidermal growth factor receptor; HGFR, hepatocyte growth factor receptor; MAPK, mitogen-activated protein kinase; mTOR, mammalian target of rapamycin; PDGFR, platelet-derived growth factor receptor; PI3K, phosphatidylinositol 3'-kinase; PKC, protein kinase C; PLC, phospholipase C; PTEN, phosphatase and tensin homolog; SAHA, suberoylanilide hydroxamic acid; VEGFR, vascular endothelial growth factor receptor.

## Chapter II

# Two-photon Excitation of Quantum Dots Under Ambient Condition

The studies in various biological subjects rely more and more on gaining clear and accurate fluorescence microscopic images of the whole sample in all three dimensions. However, not all widely used fluorescence excitation methods can satisfy the expectation. The wide-field excitation causes high fluorescence background and unwanted photo-damage to the sample, though it can excite fluorophores deep inside the sample. In contrast, the TIRFM offers a highly discriminative excitation field and a clear background, but the imaging depth is very limited to the vicinity of the surface. Two-photon (2P) excitation, with its intrinsic unique characteristics, is able to fulfill the both requirements of discriminative excitation and large excitation depth, and therefore becomes a promising tool for cell and tissue imaging. When the excitation volume is confined to a diffraction limited spot, the fluorescence background is significantly reduced and the photo-damage to the rest area of the sample is minimized.

However, unfortunately, most organic fluorophores as well as fluorescent proteins, which are the two biggest classes of probes in most fluorescence imaging experiments, have very small cross sections under 2P excitation, and

are literally not bright enough to be imaged at single molecule level and thus incapable of super-resolution microscopy which is accomplished by accurately localizing the stochastically “on” or “off” individual fluorophores. In this chapter it will be shown that single quantum dots (QDs) can be excited and imaged in aqueous solution with 2P excitation, and localized down to nanometer spatial accuracy and millisecond temporal resolution. The intermittence of quantum dot emission (i.e. “blinking”) can be well suppressed by small thiol group-containing reductants, so that it can be used in motion tracking. The utilization of the unique character, blinking, of quantum dots will be further discussed in latter chapters. This advancement will greatly broaden the application of two-photon microscopy in biological researches.

## 2.1 Quantum Dots

Quantum dots (QDs), also known as nanocrystals, are a special class of semiconductors. They are small spheres, the semiconductor core of which are typically 2 – 10 nm in diameter. Therefore, different with bulk semiconductors, excitons of the quantum dot are confined in all three spatial dimensions. The electronic and optical properties of a quantum dot are basically dominated by its material, size and shape. There are many energy band gaps in one quantum dots. A larger quantum dot has more energy levels and smaller energy band gaps, so the energy required to excite the quantum dot as well as the energy emitted in relaxation is less, which means the quantum dot has redder excitation and emission spectra. Quantitatively, the band gap energy was reported

inversely proportional to the size of the quantum dot. Recent researches suggested that the shape (e.g. the ratio between the length and the width of a quantum rod) might also affect the coloration. Moreover, it was reported that the lifetime of the fluorescence emission is related to the size of the quantum dot, too [49], because larger quantum dots have more densely spaced energy levels so that the electron-hole pairs have more chances to be trapped and therefore survive longer in larger quantum dots.

Quantum dots can be synthesized in colloidal solutions by chemical aggregation, or by lithography for the purpose of more precise control over product size. The common materials of the semiconductor nanocrystal cores are cadmium mixed with selenium or tellurium (CdSe or CdTe). Recently more and more cadmium-free quantum dots have been invented and used because the heavy metal (e.g. cadmium) is banned in many human-related applications by more and more countries. Most commercially available quantum dots for lab researches are provided with thick shells (e.g. CdSe nanocrystals with ZnS or CdS shells). The shell thickness has been shown directly correlated to the fluorescence lifetime and intensity. Figure 2.1 shows a scheme of the structure of a commercial quantum dot (Qdot, Invitrogen). The core contains from several hundred to several thousand atoms, making its size range from a couple of nanometers to more than 10 nanometers, so the color of the quantum dot can vary from very blue to very red (Fig. 2.2).

Quantum dots have huge superiorities to the organic-based fluorophores which are its incomparable brightness and near-infinite lifetime (under normal

experimental one-photon excitation power). It was estimated that quantum dots are 20 times brighter and 100 times more stable than traditional fluorescent probes [50]. Thus the quantum dots have been playing more and more important roles in cellular imaging as well as *in vitro* and *in vivo* single molecule experiments [50] [51-56].

Quantum dots have also been used in tumor targeting and imaging. They can be surface-modified to conjugate with binding ligands to receptors on cancer cells (e.g. as used in this thesis), which is called active targeting. On the other hand, passive targeting can also be used that quantum dots permeate into the cell body since the cancer cell membrane has much higher permeability than healthy cell membrane. Once bound, the quantum dots can localize the specific receptors, revealing its various information such as localization, transportation, aggregation, etc., which will be further discussed in the thesis.

## 2.2 Individual Quantum Dots Imaged with 2-Photon Excitation in Aqueous Solutions

One-photon (1P) microscopy of individual quantum dots (QDs) has become routine [52, 57, 58]. In contrast, two-photon (2P) microscopy has not had the same success. This, despite the many advantages that 2P microscopy offers: reduced scattering, deep sample penetration, and intrinsic confocality when excited with point excitation [32]. Only in artificial environments, such as air-dried samples of QDs [59], or at cryogenic temperatures [60], has individual 2P QD-microscopy been possible. 2P microscopy of individual organic-based

fluorophores has similarly been problematic since most fluorophores have very small 2P absorption cross-sections, as well as poor photostability [61, 62].

We report the application of 2P microscopy to individual QDs in a biological setting with nanometer spatial accuracy and millisecond temporal resolution, both *in vitro* and *in vivo*. In part, this is possible by realizing that emission is very strong, and hence a much lower amount of excitation light is needed as compared to organic fluorophores. In fact, at the usual excitation level needed for 2P excitation of organic fluorophores, the QDs tend to bleach rapidly. Furthermore, the photophysical properties of QDs under 2P excitation were improved by adding reductants to the imaging buffer, resulting in increased photostability and near complete suppression of blinking. This was true for widefield excitation (which is not possible for 2P microscopy of conventional fluorophores), and also in a scanning mode excitation.

The image of the fluorescence of individual QDs with a widefield 2-photon excitation is shown in figure 2.3. Figure 2.4 shows the quadratic power ( $I^2$ ) dependence on the excitation light, indicating 2P excitation. At an IR laser flux of  $\geq 250 \text{ kW/cm}^2$ , saturation begins to take place, accompanied by significant photobleaching. We note that for our measured QDs, the 2P excitation threshold where photobleaching occurs is about 20 times lower than the 2P excitation levels reported for organic dyes [32, 63]. This relatively low saturation threshold of QDs may clarify why single-QDs 2P imaging, under ambient conditions, has not been reported: QDs would immediately photobleach under the 2P excitation power typically used with conventional organic-based fluorophores.

We are quite clearly observing single QDs, as shown by figure 2.5. It shows the intensity trace vs. time of a single QD, where the excitation intensity is increased in a stepwise manner, resulting in a stepwise increase in the emission intensity until saturation is reached and subsequent photobleaching. In addition, the emission intensity traces of the single fluorescent spots exhibit a distinct fluorescence intermittency (blinking) behavior (Fig. 2.8), characteristic of single QDs emission [64]. Figure 2.6 shows the corrected excitation spectra, ranging from 760 nm to 1000 nm, for three different QDs samples with peak emissions at 525 nm, 585 nm and 655 nm. The spectra of all three samples displayed highly efficient excitation from 760-900 nm, enabling simultaneous multicolor imaging.

Not very surprisingly, we also noticed that single quantum dots can be well excited and imaged with 2-photon under TIR condition (Fig. 2.7), as long as the laser power is sufficient.

### 2.3 Suppression of Emission Intermittence of Quantum Dots

Blinking was decreased by adding 1~100 mM Dithiothreitol (DTT) (or 1~10%  $\beta$ -Mercaptoethanol), resulting in almost complete suppression of blinking events (> 90%) (Fig. 2.8). Figure 2.9 shows the effect of DTT on the averaged emission intensity of >100 individual QDs, where an increase in DTT concentration clearly results in an increase in average emission intensity due to suppression of blinking and elimination of non-emitting “off” states.

Other reductants, such as glutathione, tris(2-carboxyethyl)phosphine (TCEP) and 6-hydroxy-2,5,7,8-tetramethylchroman-2-carboxylic acid (Trolox,

Hoffman-LaRoche), were also tested. However, none of them can reduce the blinking. It can be noticed that the tentative rule here is the reductant must contain a thiol group and must be small in molecular size, e.g. the DTT and the BME. The thiol-containing but large reductants such as the glutathione will not work. Neither will the carboxylic reductants such as TCEP and Trolox. We reason it is because the thiol group ( $-SH$ ) is required to bind to and heal the surface of the quantum dots, and small molecular size allows (a sufficient number of) reductants to approach the surface.

## 2.4 Myosin V Stepping Assay with Wide-field 2-Photon Excitation

The wide-field excitation was then applied in stepping assay of individual myosin V molecules labeled with a QD. The myosin V was labeled with a 655 nm QD at its C-terminus, the cargo domain (Fig. 2.10a). We expected the step size to be  $\sim 36$  nm based on previous results from optical trapping [65] and 1P-FIONA data [1]. Figure 2.10b shows the point spread function (PSF) excited with 1P at  $0.4 \text{ kW/cm}^2$  and 2P excitation at  $200 \text{ kW/cm}^2$ . At 30 ms exposure time, under 2P excitation, we detected  $\sim 25,000$  photons and achieved 0.9 nm accuracy, while under 1P excitation we detected  $\sim 20,000$  photons and achieved 1.1 nm. Figure 2.10c shows myosin V walking with 2  $\mu\text{M}$  ATP, integrated every 50 ms, and excited either with 1P or 2P. With 1P, we measured  $35.4 \pm 7.0$  nm, and with 2P, we measured  $35.8 \pm 6.3$  nm. These are in excellent agreement with each other and consistent with the expected value. The motor protein stepping rate is apparently not affected by strong IR power used in 2P excitation. We also note

that TIR or near-TIR [4, 66] was not required here because of the exceptional brightness and signal-to-noise of the QDs.

## 2.5 Materials and Methods

*Flow chamber and in vitro QD samples:* A glass slide (Fisher Scientific) with two holes was made, drilled at 1.5 – 2 cm separation. A glass coverslip (Fisher Scientific) with two strips of double-stick tape was added to form a flow chamber, followed by 5 Minute Epoxy (ITW Devcon) to seal the side of the flow chamber. 100  $\mu$ L of 1 mg/mL BSA-biotin in pH 7.0 Phosphate Buffered Saline (PBS) buffer was flowed over the coverslip and allowed to sit for 10 min at room temperature (RT), and then washed with 60  $\mu$ L PBS buffer. 100  $\mu$ L of 100 pM Qdots (525/565/585/605/655 nm, Invitrogen) in PBS buffer was flowed into the chamber and let sit at RT for 10 min. To photostabilize the QDs, 100  $\mu$ L 100 mM DTT (or 10% 2-Mercaptoethanol, or other reductants at various concentrations as tested in experiments) was flowed through the chamber to wash away non-immobilized QDs. Otherwise, PBS buffer was used.

*Wide-field microscope:* The 2-photon widefield microscope was basically the same as a 1-photon widefield microscope, except a wavelength-tunable IR laser, Mai Tai HP (SpectraPhysics), was used as excitation source instead of visible lasers. Briefly, the microscope was based on an Olympus IX-71 inverted microscope, the laser was directed by dielectric mirrors (BB1-E03 and BB2-E03, Thorlabs) and focused by a 300 mm focus length (f) lens (AR-coated at 650-1050 nm, Thorlabs) into the back aperture of a 100 $\times$  1.45 numerical aperture (NA)

achromatic objective (Olympus) and collimated through it. A 60× 1.2 NA achromatic lens (Olympus) A 725nm short-pass or a 650nm short-pass dichroic (Chroma) was used in the microscope. Emission filters such as HQ610/130M, HQ535/50M and ET750SP (Chroma) were selected according to QD emission spectra and inserted into the microscope to filter out excitation laser.

*Excitation Spectra:* We took widefield images of 1  $\mu\text{M}$  QDs which densely covered the imaging area of the glass surface. The sample was made by dropping 4  $\mu\text{L}$  1  $\mu\text{M}$  QD onto a glass slide and then clamped by an 18 mm  $\times$  18 mm cover slip and sealed by 5 Minute Epoxy. We varied the excitation laser wavelength and recorded the excitation power and the emission intensity. To correct the excitation spectra, we obtained the emission intensity per unit excitation power by  $E_{m_0} = E_m/E_x^2$ , where the  $E_m$  is the original emission intensity.

*Myosin V stepping assay:* Myosin V was labeled on its cargo-binding domain with a 655 nm QD via anti-GFP antibody. F-Actin was polymerized at 1:20 biotinylation ratio (1 biotin/20 actin monomers) and immobilization onto glass coverslip surface via BSA-biotin-NeutrAvidin (Invitrogen)[1]. Myosin V was then flowed into the sample chamber, excess myosin washed away, and a solution containing 1  $\mu\text{M}$  ATP and 100 mM DTT was added. The sample was excited by 2-photon widefield, at 840nm and 300 mW, and the fluorescence emission was imaged onto the EMCCD camera. The images were taken at 30 msec exposure time, 10 MHz readout rate, 5.2× pre-gain and 40 EM gain. With

250× total magnification (100× objective plus 2.5× additional tube lens), the effective pixel size was 64 nm.

*Stepping data analysis:* Detailed description about the 2D FIONA analysis, can be found in the Yildiz et al paper [1]. Localization accuracy is the standard error of the mean of the center of the Point Spread Function (PSF). The step size was determined by student's t-test in a program written in IDL.

## 2.6 Figures

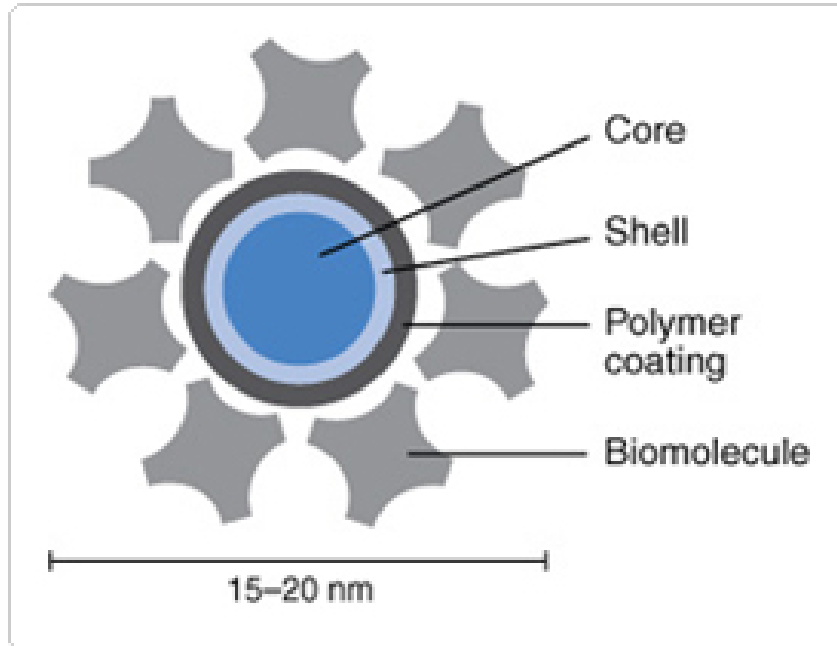


Figure 2.1 | Scheme of the structure of a commercial quantum dot. (Picture from Invitrogen)

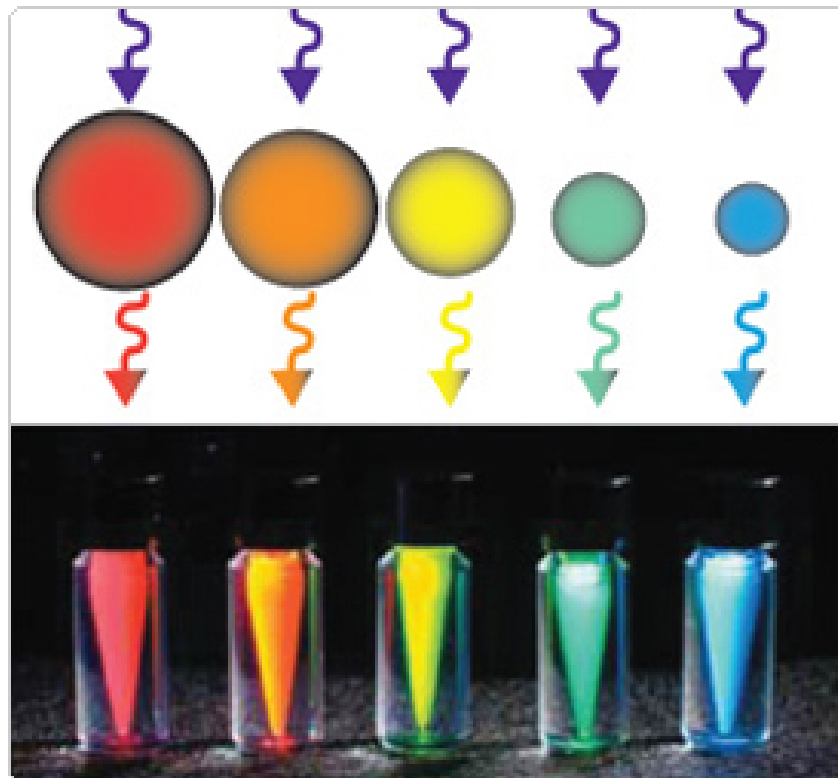


Figure 2.2 | Five different quantum dot solutions are shown excited with the same UV lamp. The size of the nanocrystal determines the color. (Picture from Invitrogen)

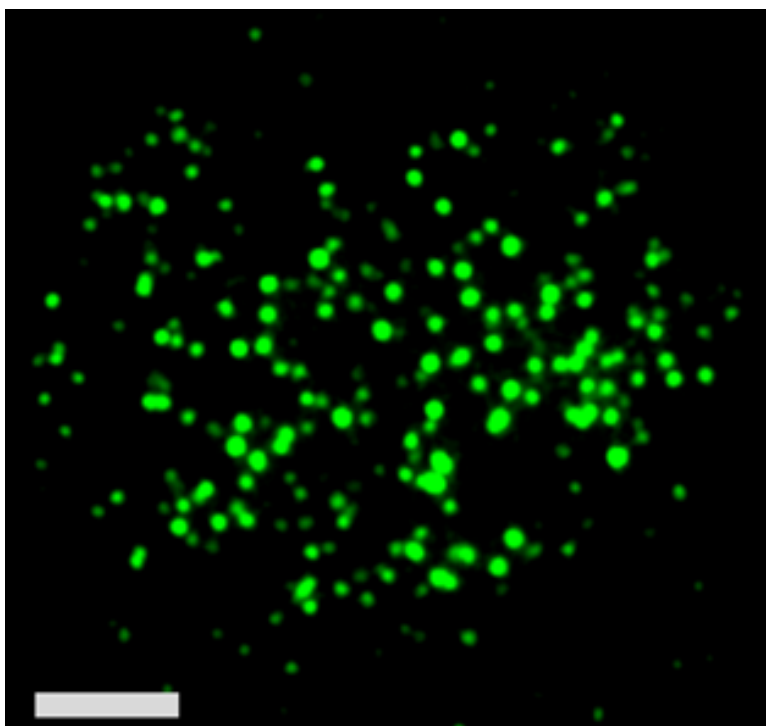


Figure 2.3 | An Image of 2P excited individual QD525. QDs were conjugated to streptavidin and tethered to BSA-biotin coated surface. Imaging buffer (DPBS, pH7.5) was supplemented with 50mM DTT. Bar equals to 3  $\mu\text{m}$ .

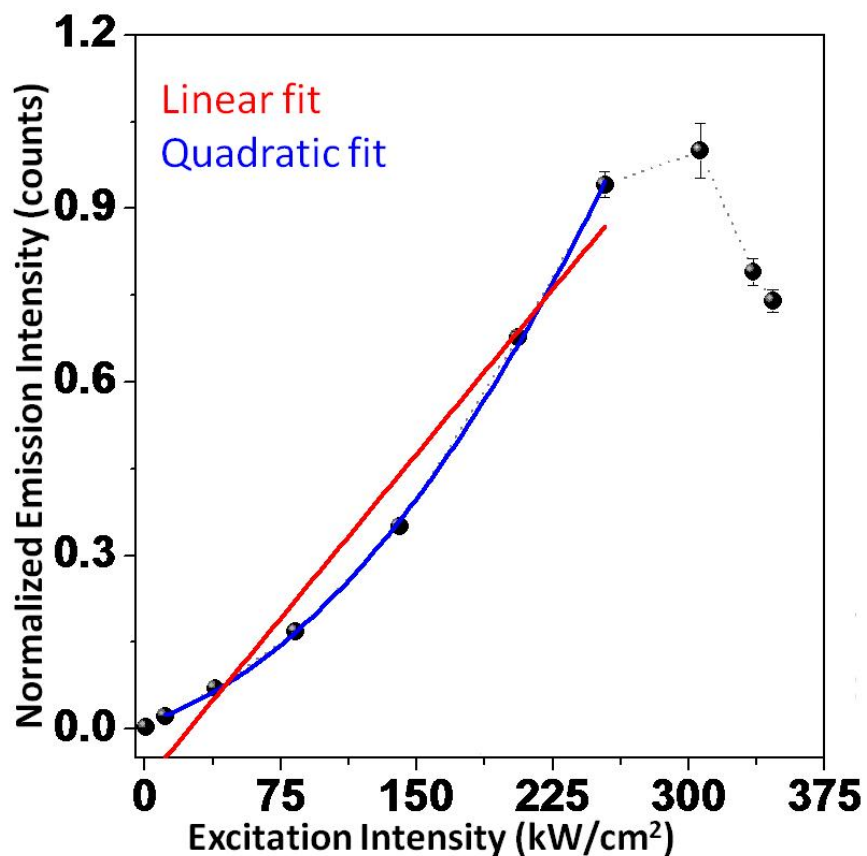


Figure 2.4 | The summed emission intensity of individual QDs plotted versus two-photon excitation intensity. QDs showed a quadratic increase in emission intensity with increase two-photon excitation, in agreement with quadratic power law dependence of two-photon excitation. At higher two-photon excitation power QDs emission reaches maximal response and photobleaching occurs resulting in a plateau and decrease of the response curve.

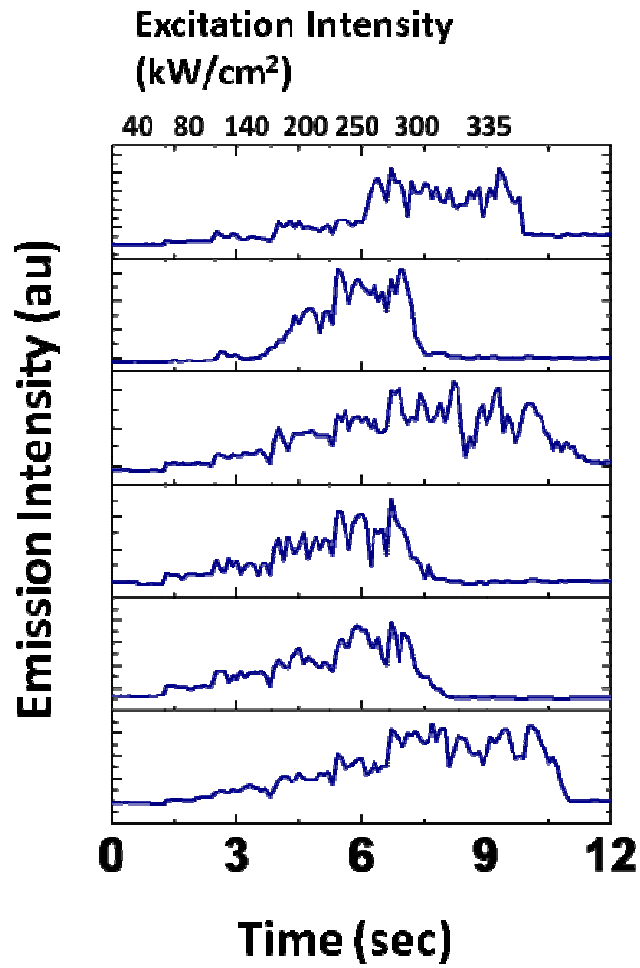


Figure 2.5 | Intensity of single QDs emitting at 525 nm change along with time and excitation power, and photobleach when the power reaches a threshold.

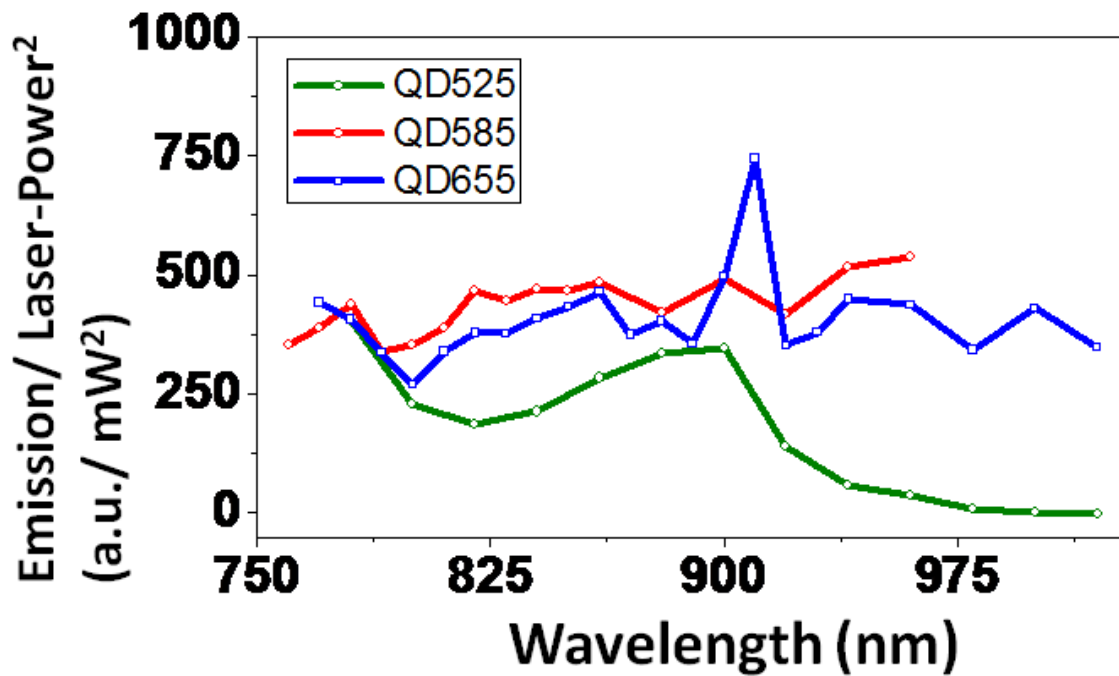


Figure 2.6 | Excitation spectra of three kinds of quantum dots emitting at 525 nm, 585 nm and 655 nm.

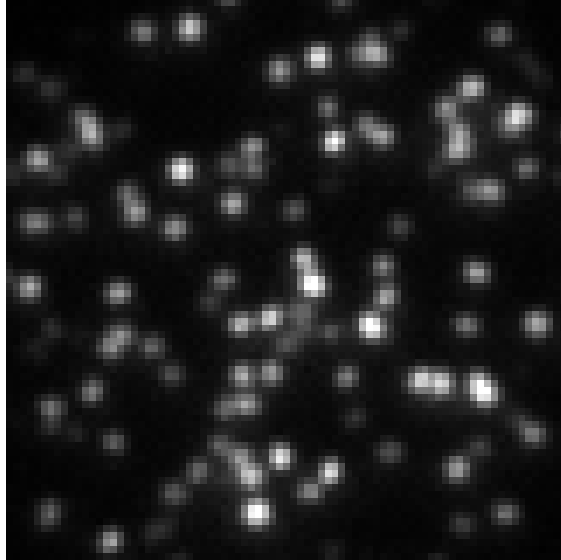


Figure 2.7 | A two-photon TIRFM image of individual QD655. Taken with EMCCD at 29 ms temporal resolution and 100 EM gain. 50 mM DTT in presence.

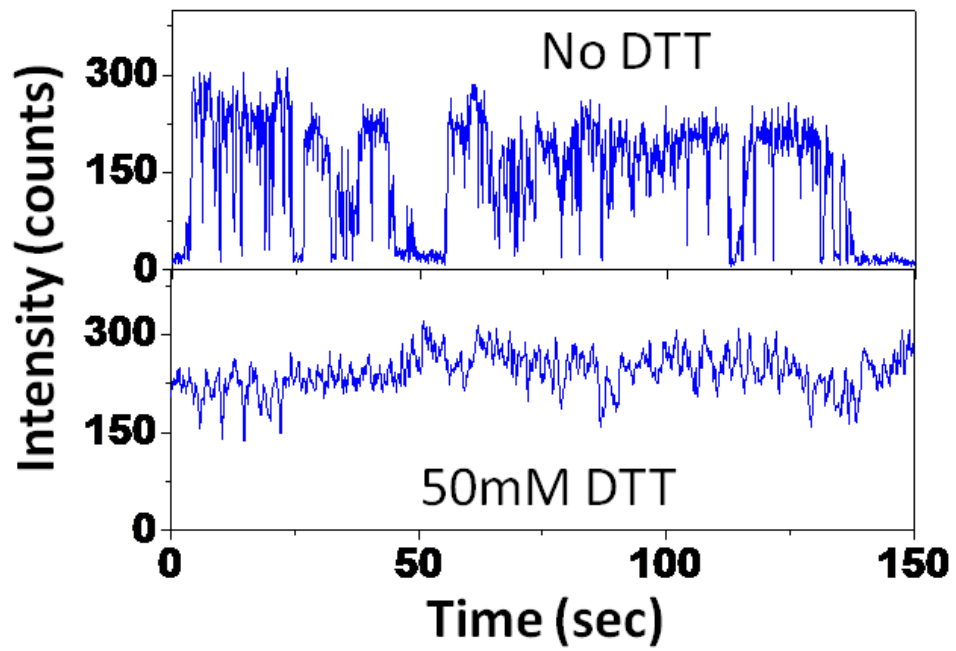


Figure 2.8 | Blinking is near completely eliminated by adding in DTT. Upper panel, the intensity vs. time trace of a QD585 without any DTT. Lower panel, the intensity vs. time trace of the same QD with 50 nM DTT in presence.

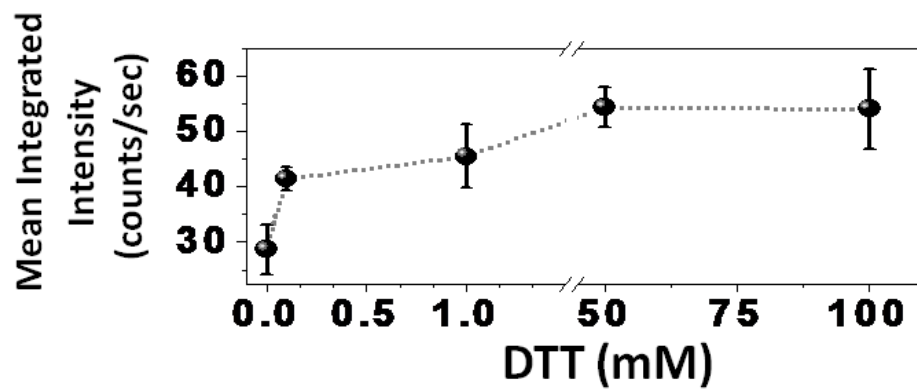


Figure 2.9 | DTT enhances the QD emission more when its concentration increases.

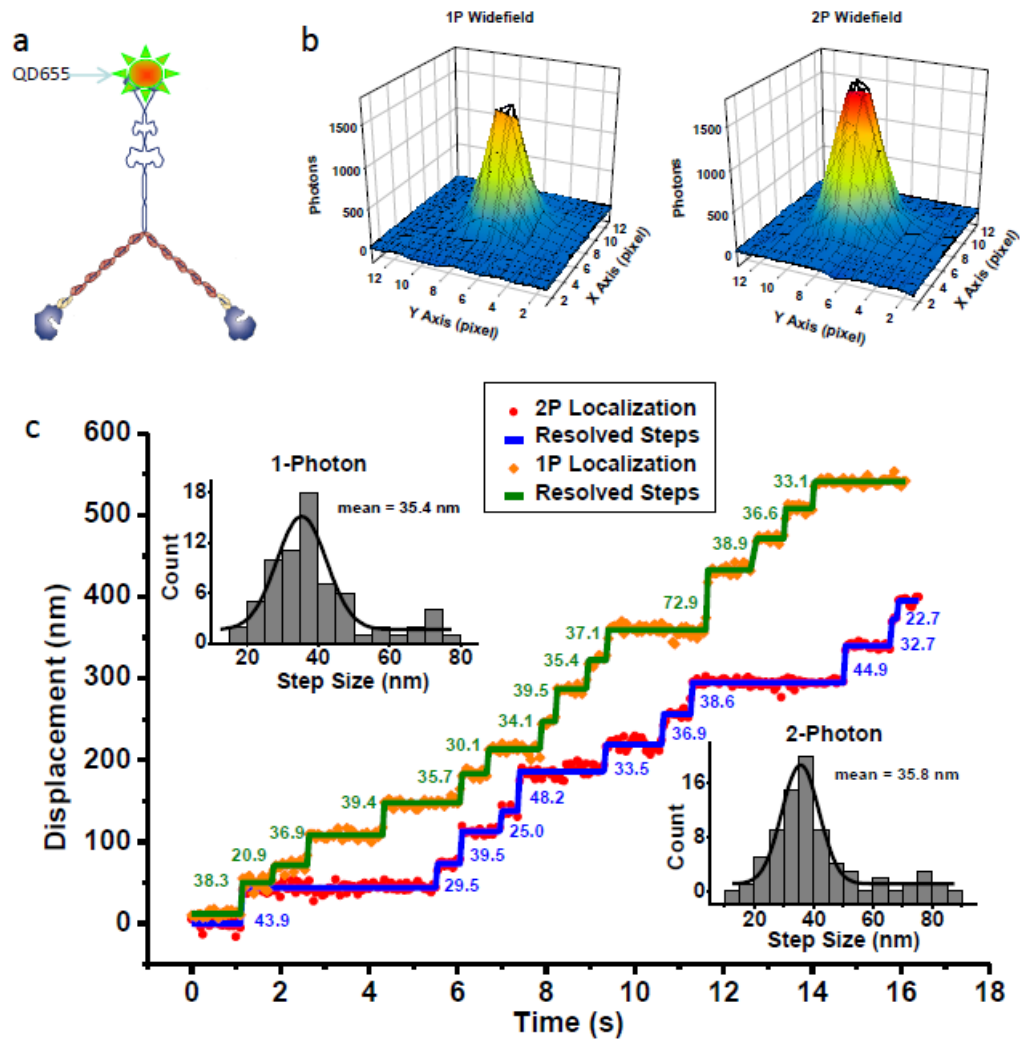


Figure 2.10 | 2P widefield excitation resolves Myosin V step sizes at nanometer accuracy. (a) Labeling of myosin V construct. (b) 1-photon PSF (left) and 2-photon PSF (right) of single QD and the 2D Gaussian fitting. Data taken at 50 ms exposure time and with 100 mM DTT. With collected fluorescence, localization accuracies are 1.1 nm under 1P and 0.9 nm under 2P excitation. (c) Displacements of two myosin V motors resolved at 50 ms temporal and one nanometer spatial resolutions under 1P and 2P excitation. Step sizes are determined by student's t-test, and fitted via Gaussian fit at 35.4 nm and 35.8 nm, respectively.

## Chapter III

# Fast Two-photon 3D Scan Microscopy with Holographic Excitation

The superiority of 2-photon excitation is mostly demonstrated in scanning microscopy with diffraction limited spot excitation, where the localized excitation volume significantly reduces the fluorescence background, increases the signal-to-noise ratio, diminishes unwanted photo-damage, and meanwhile remains high imaging depth. It also has a couple of disadvantages compared to 1-photon excitation. The first is, as discussed in the previous chapter, that most organic dyes as well as fluorescent proteins have very small cross sections under 2-photon excitation and thus are not sufficiently bright for single molecule imaging and super-resolution techniques. Quantum dots can satisfyingly be an alternative probe for the use of 2-photon microscopy, due to its high brightness and long lifetime with 2-photon excitation under ambient conditions.

However, another drawback of 2-photon scan microscopy still remains unsolved that the scan with a single tiny excitation spot over a large 3D space to gain a whole 3D picture is really slow and needs quite a long time. Long imaging time may cause many problems and limit the application of 2-photon microscopy. First, the time resolution is unsatisfying. The conventional scan microscopy can hardly be used to image a relatively dynamic sample, e.g. a live cell. The

biochemical conditions in the live cells, as well as the physical characteristics, are not stationary and might have significant change before the microscope accomplishes one whole scan. Also, the 2-photon scan has intrinsically high excitation depth and should have been potential in 3D FIONA and tracking, but the too long imaging time totally limit its use in this promising field. Second, even for immobilized samples, e.g. a fixed cell, the drift of the sample, caused by various environmental factors, may accumulate to a level that is not negligible. In some cases, the fluorescent probes may even (partially) photobleach due to the oxidization and thus result in a failed experiment.

In sum, increasing the imaging rate is very critical for broadening the application of 2-photon microscopy. This chapter presents a technical innovation that can accelerate the 2-photon scan imaging by 80-fold or potentially more. Briefly, a  $9 \times 9$  matrix of 81 excitation spots, or any reasonable  $N \times N$  matrix, generated by a spatial light modulator (SLM) or a stationary holograph is used to accomplish parallel excitation instead of a single excitation spot. On the other hand, an array detector, EMCCD camera, replaces the conventional point detector, the photomultiplier tube (PMT), to fulfill simultaneous acquisition of the emission from multi-point array excitation.

### 3.1 Configurations of the Microscopy

Several different designs were chosen for the excitation in the 2P microscope (Fig. 3.1).

(a) Due to their large 2P absorption cross section, resulting in highly efficient excitation and apparently reasonable quantum yields, individual QDs could be imaged using widefield epifluorescence excitation (see “Widefield” excitation path, Fig 3.1.1). This is in contrast to 2P excitation of single organic fluorophores, which needs high power density and thus requires that the excitation light be focused to a small spot. Widefield excitation, however, does not produce confocal z-resolution as produced by conventional 2P microscopy.

(b) We therefore constructed a conventional 2P confocal set-up by forming a diffraction-limited spot that was scanned over the sample using x- and y- scan mirrors and a piezo-scanning microscope-objective for the z-axis. (see “Scan” excitation path, Fig 3.1.1).

(c) Highly efficient 2P imaging of individual QDs could be achieved at very low laser powers (usually no higher than 2 mW), so using a single spot 2P confocal excitation leaves a surplus of laser excitation light. Based on this, we used holographic optical components, inserted in the excitation path, to create an array of diffraction-limited spots for simultaneous multipoint excitation. Two different holographic components were used to create passive- or active-multipoint excitation arrays. The first was a diffractive beam splitter (Holo/Or Ltd, Israel) (Fig. 3.1), creating a passive, stationary  $9 \times 9$  holographic matrix (HM) of diffraction-limited spots separated by  $1.6 \mu\text{m}$  (3.2.1). The second was a Spatial Light Modulator (SLM) (Boulder Nonlinear Systems), generating an active holographic matrix which was programmable and scannable (Fig. 3.2). The multipoint scan has previously been done using an array of dichroic mirrors [67], but

here we present a simpler and easier way. We primarily used the diffraction beam splitter and scanned the passive HM by scan mirrors and a piezo-stage. With both the SLM and the HM method, the element was placed at a plane conjugate to the back aperture of the objective via pairs of 4f lenses. The scan rate was increased by the number of spots used simultaneously — for the  $9 \times 9$  HM, it was an 80 fold increase ( $= 9^2 - 1$ , where 1 is because of the missing central spot, Fig. 3.3).

### 3.2 Excitation: the Holographic Matrix

The excitation laser spots were generated by a special light modulator (SLM, Boulder Nonlinear Systems, Inc.) or a diffractive beam splitter (Holo/Or Ltd.). The difference in the beam path is that the SLM reflected the laser beam in the beam path (Fig. 3.2), while the splitter passed it (Fig. 3.1, see “scan” path). The SLM ran on Blink software (BNS, Inc.) and received holograms calculated by a self-developed SciLab (Digiteo) program, and modulate the laser beam wavefront to a  $5 \times 5$  matrix of  $1.5 \mu\text{m}$  line separated beams. The HM was able to split the beam to be a  $9 \times 9$  matrix with  $0.09^\circ$  separation. The line separation could be adjusted to  $1.6 \mu\text{m}$  by adding in an extra pair of 4f lenses with  $0.4\times$  magnification to the scanning beam path (Fig. 3.3). The matrix scan shared the same beam path with the single-point scan, though the images could only be taken by EMCCD camera. Since the matrix scan is a kind of parallel scan, the scan mirrors need only to move over  $1.6 \mu\text{m} \times 1.6 \mu\text{m}$  to cover a  $1.44 \mu\text{m} \times 1.44 \mu\text{m}$  area, an 80-fold increase in imaging rate. Both SLM and beam splitter worked

optimally with 785 nm laser. The intensities of the diffraction-limited excitation spots were found to be fairly uniform with a standard deviation of 15.7% across the entire HM field.

Initially we used the SLM to reduce the required optical elements (e.g. scan mirrors, piezo-stage) because the SLM can create an active excitation matrix and scan it in all three dimensions. However, we soon realized the refreshing rate of the SLM is significantly slower than the scan mirrors and the piezo-stage, so that employing the SLM would actually slow down the eventual imaging rate. We thus decided to use the stationary diffractive beam splitter to generate the passive excitation holographic matrix and scan it with commonly seen scan mirrors and piezo-stage. In this case, the modification to the conventional scan microscopy was minimized and meanwhile the fastest imaging rate was achieved.

### 3.3 Acquisition: EMCCD vs. PMT

We used an electron-multiplying charge-coupled device (EMCCD) for detection, as opposed to the usual single-point detector such as a photomultiplier tube (PMT). An EMCCD has several advantages. It can be combined with the simultaneous multipoint array excitation, providing an 80 times ( $9^2 - 1$ ) increase in imaging speed while maintaining high z-axis discrimination afforded by focused 2P excitation. It is capable of simultaneous multi-color imaging even when the fluorescence emission is divided into multi-channels. Additionally, an EMCCD eliminates spot size-related distortions, likely resulted from chromatic

aberration between excitation and emission wavelengths, as seen with descanned PMT imaging.

In order to get z resolution, one typically focuses the 2P excitation light down to a (near) diffraction-limited spot. The unique quadratic profile of the 2P excitation intensity results in a limited excitation volume, thereby providing an intrinsic confocal effect. Typically, the fluorescence is measured by a single-point detector, a PMT, and the sample is scanned in x, y, and z to generate a 3D image. However, an array detector, e.g. an EMCCD, can also be used [67]. There are a number of advantages of using an EMCCD over a PMT in confocal detection. First, the EMCCD has a relatively high quantum efficiency, > 90%, compared to 10~30% of a PMT. Second, the EMCCD has extremely low dark noise, ~3e/sec, whereas the PMT has considerably higher dark noise (~20-200 counts/sec). Third, and the most important for our excitation design, the PMT is unable to be used when multiple diffraction-limited spots are excited simultaneously, e.g. with the HM. Fourth, the PMT cannot readily correlate two different imaging modalities of the same sample, e.g., fluorescence images overlaid on brightfield images. Fifth, while a single PMT is not capable of simultaneous multi-color imaging, this can be easily accomplished with an EMCCD when used with a multi-channel splitting device (e.g. DualView or QuadView, Photometrics Inc.). Sixth, for single-molecule imaging using a PMT, there is significant issues concerning spot expansion and distortion stemming from chromatic aberrations between excitation and emission (see below). These problems are easily resolved when an EMCCD is used for imaging.

To compare imaging configurations, we used a diffraction-limited spot, scanned over x, y and z by a pair of scan mirrors (x-y axes) and a piezo translation stage holding the objective (z axis). We then imaged with either an EMCCD or a PMT. The x-y and z scan step sizes were 100 nm. This was identical to the effective pixel size (after magnification) of our EMCCD. The minimal residence time of the scan mirrors on each pixel was 0.005 ms, while for the majority of our experiments we used a residence time in the range of 0.02 ~ 1 ms, as needed. The total x-y areas scanned in our experiments was set to  $20\ \mu\text{m} \times 20\ \mu\text{m}$ , or a quarter of it, so that the time length to finish one x-y scan varied from less than a second to tens of seconds. When using a PMT, the collected fluorescence intensity was correlated with the scan such that each scanned coordinate yields a pixel in the image. Imaging with an EMCCD differs as detection is already spatially resolved. Data acquisition was correlated with the scan where the integration time of each EMCCD frame was either a whole x-y scan, or an integral fraction of it, depending on the total time length of the scan. Generally, longer EMCCD frame exposure time caused higher non-fluorescence background because of the non-zero dark noise, and thus the exposure time was kept under 1 sec.

Figure 3.4a-c show images of surface-tethered 565 nm quantum dots, acquired with configurations where an EMCCD was used with either widefield- (Fig. 3.4a) or single-point scanning excitation (Fig. 3.4b), or a PMT was used in the standard single-point scanning (Fig. 3.4c). Fig.3.3.1d shows the overlay, indicating good correlation. Figure 3.4e shows histograms of PSFs from each of

the three imaging configurations. The EMCCD imaging with either widefield or point-scan excitation yielded the narrowest FWHM ( $274 \pm 14$  nm, [black];  $271 \pm 17$  nm [red], respectively). With this FWHM, a localization ability of a ~nanometer can be obtained with an EMCCD and enough photon counts. (For the data shown in the histogram, the total photon number was about 8800; the accuracy was then approximately  $(270/8800)^{1/2} = \sim 2.9$  nm[29].) The PMT, in contrast, produced larger and more asymmetric spots: FWHMs =  $338 \pm 28$  nm in the x-direction (blue), and  $427 \pm 37$  nm in the y-direction (cyan).

With the PMT, the size-expansion and the asymmetry between x and y are functions of the difference between the excitation and emission wavelengths (Fig. 3.5a-b, Fig. 3.6, Table 3.1), and also depend on whether the emitter is smaller or larger than the diffraction limited excitation spot (Fig. 3.7). We have several lines of evidence for this, including PMT vs. EMCCD data where the difference between excitation and emission wavelength varies, and where the size of the emitter varies. For example, when QDs emitting at 525 nm were excited at 850 nm, 800 nm, and 750 nm, the FWHM for the PMT-collected fluorescence spot was 620 nm, 525 nm, and 310 nm, respectively (Fig. 3.5b). In contrast, for the EMCCD data, the PSF was always round and symmetrical, with an average FWHM of 274 nm (Fig. 3.5b). The measured asymmetry, namely the ratio of the x-axis to y-axis was found to be  $\sim 1.25$  for spots recorded with a PMT, and 0.99 for spots imaged with the CCD. However, for QDs emitting at 655 nm, where the emission was closer to the excitation (at 750-850 nm), the expansion,

distortion, and chromatic aberration was small for the PMT data (as well as the EMCCD data). (Fig. 3.6, Table 3.1).

Then we could easily reason that if a non-single molecule sample, significantly larger than diffraction limit, is used, both the PMT and the EMCCD should give the same imaging quality as the scan on PMT reflects the size and shape of the fluorescent object, which was proved by experimental results. For instance, in the image of *E. coli* labeled at the fairly high concentration of 10 nM  $\lambda$  565, all asymmetry vanished (Fig. 3.7a). Another example was fluorescent beads of 2.3  $\mu$ m average diameter, i.e. bigger than the diffraction limit of light. In this case, all elongation and expansion with the PMT (or EMCCD) vanished (Fig. 3.7b). We therefore believe the spot size change, and the asymmetry, is due to the chromatic aberrations in exciting a single molecule sample, likely because the microscope objective has different focal lengths at different wavelengths. In summary, the PMT is inferior in single molecule imaging, but is still good at imaging large biological objects.

### 3.4 Materials and Methods

*Single-point scanning 2-photon microscope:* A wavelength-tunable IR laser, Mai Tai HP (SpectraPhysics), was used as excitation source instead of visible lasers. Briefly, the microscope was based on an Olympus IX-71 inverted microscope, the laser was directed by dielectric mirrors (BB1-E03 and BB2-E03, Thorlabs). One 60 mm fl lens and one 300 mm fl lens (AR-coated at 650-1050 nm, Thorlabs) were used to expand and collimate the IR laser beam. The laser

was focused by a 100× 1.45 numerical aperture (NA) achromatic objective (Olympus) into a diffraction limited excitation spot. A pair of motorized mirrors (ISS Inc., Champaign, IL) and a piezo stage (ISS) under the objective were used to scan the laser in x-y and z axis, respectively, and synchronized by ISS dual clock module. The scan could run at various step sizes (typically at 50 nm, 64 nm or 100 nm), up to 100 µm scan range. A 725nm short-pass or a 650nm short-pass dichroic (Chroma) was used in the microscope. Emission filters such as HQ610/130M, HQ535/50M and ET750SP (Chroma) were selected according to QD emission spectra and inserted into the microscope to filter out excitation laser. For multicolor imaging, a QuadView tube or a DualView tube (Photometrics) was added after the microscope, and FF01-525/565/605/655/15-25 single band emission filters (Semrock) were included in the tube for the four colors of QDs. Images were recorded with an EM gain CCD camera (iXon+, Andor) or a Photomultiplier Tube (H7421-40, Hamamatsu).

*Matrix scanning microscope:* The excitation matrix was generated and scanned as described in 3.2. The scan parameters were set in ISS Vista. For 3D scan, the scan step size in the three dimensions are usually set to be the same, in most cases 64 nm or 100 nm. The scan system sent out trigger signals to start exposure of the CCD camera or the PMT. The correlation is further described in next paragraph, the *image acquisition*.

*CCD/PMT image acquisition and comparison:* The Andor iXon+ EMCCD camera and the Hamamatsu PMT were attached to the microscope through a switchable-mirror C-mount, where the fluorescence was directed to the PMT or

the EMCCD. The EMCCD camera was operated with Andor Solis software but correlated to the ISS scan system. Images were usually taken under kinetic acquisition mode and external trigger. When one x-y scan started the ISS scanner sent out a square wave signal to trigger the EMCCD camera to begin capturing the image. During the x-y scan the wave signal stayed at logic high. When the CCD camera received the trigger signal it opened the internal shutter and started the exposure. During the time that the trigger signal kept logic high, the shutter stayed open and the exposure continued. When the one x-y scan completed and the triggering signal dropped to logic low, the camera closed the shutter and ended capturing the image. So the scanner and the detector worked in correlation. Usually 5.2× pre-gain and adjustable EM gain (up to 300) were used but could be adjusted according to the emission intensity. The PMT ran on ISS Vista software. Both EMCCD and PMT recorded data were saved as tiff files and were primarily analyzed in ImageJ (NIH) or WinView32 (Roper Scientific). Intensity profiles of the fluorescence spots in the images were extracted and analyzed by self-written programs in IDL (ITT VIS) or MatLab (MathWorks, Inc.). The point spread functions were fitted to Gaussian peaks to obtain full width at half maximum (FWHM) as well as localization (see later section). A judgment between the EMCCD and PMT imaging was made by FWHM comparisons. Superimposition of the widefield and scanning images was done in ImageJ.

### 3.5 Figures and Tables

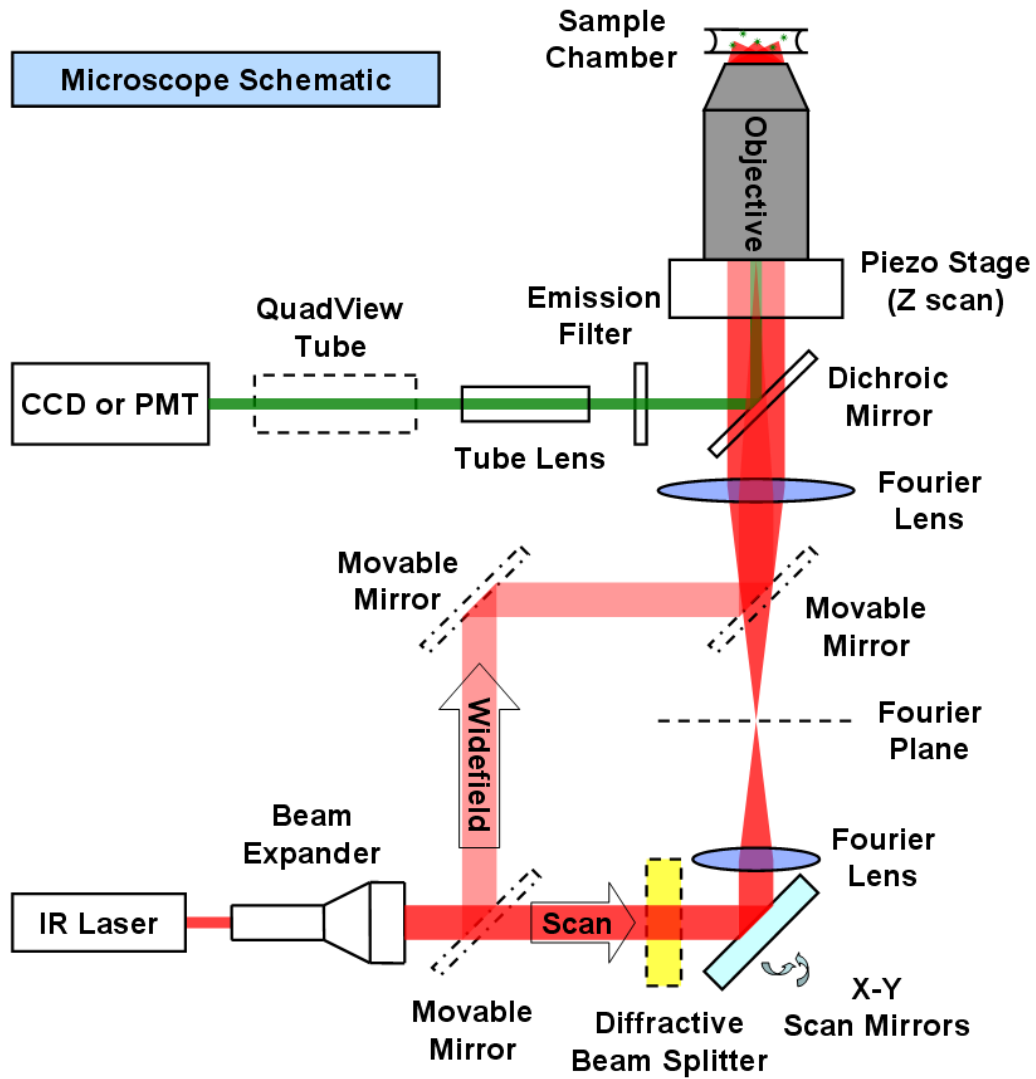


Figure 3.1 | Schematics of the wide-field, the single-point scan and the stationary holograph matrix scan setups. In the sample chamber a 3x3 matrix is illustrated in an exaggerated form.

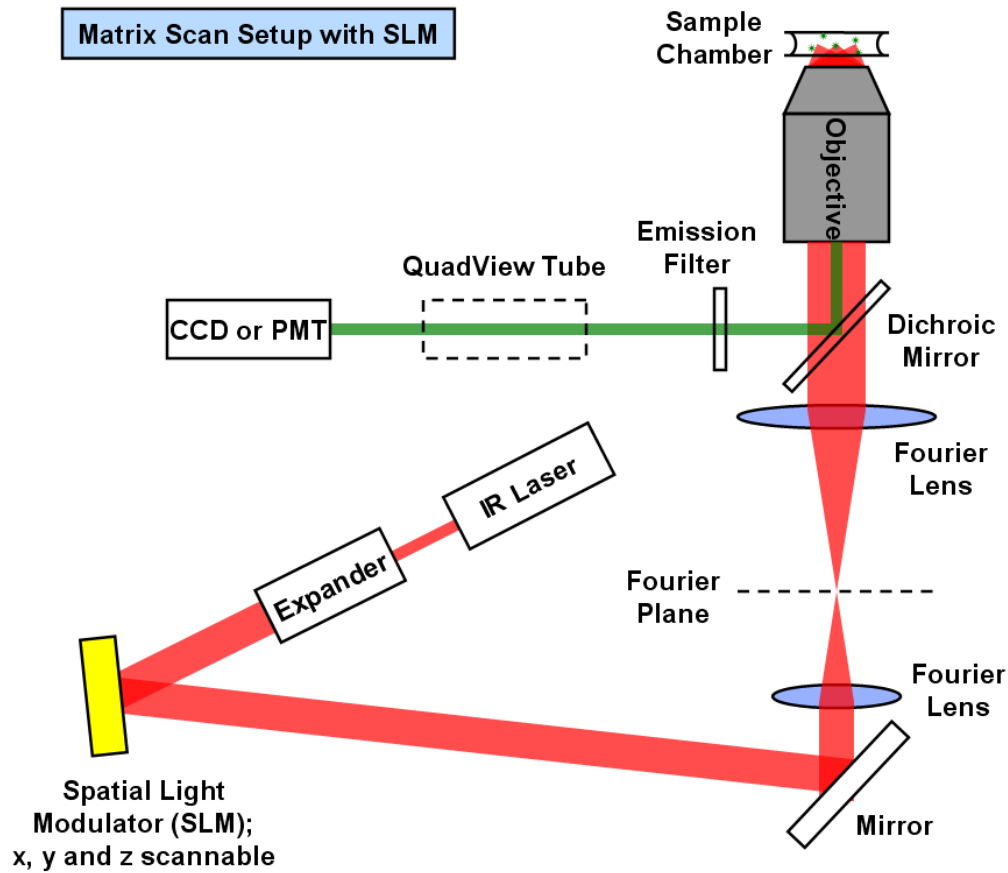


Figure 3.2 | Schematic of multipoint holographic matrix scan setup with spatial light modulator (SLM). The SLM can do scans over x, y and z, and saves the job of the scan mirrors and the piezo translation stage.

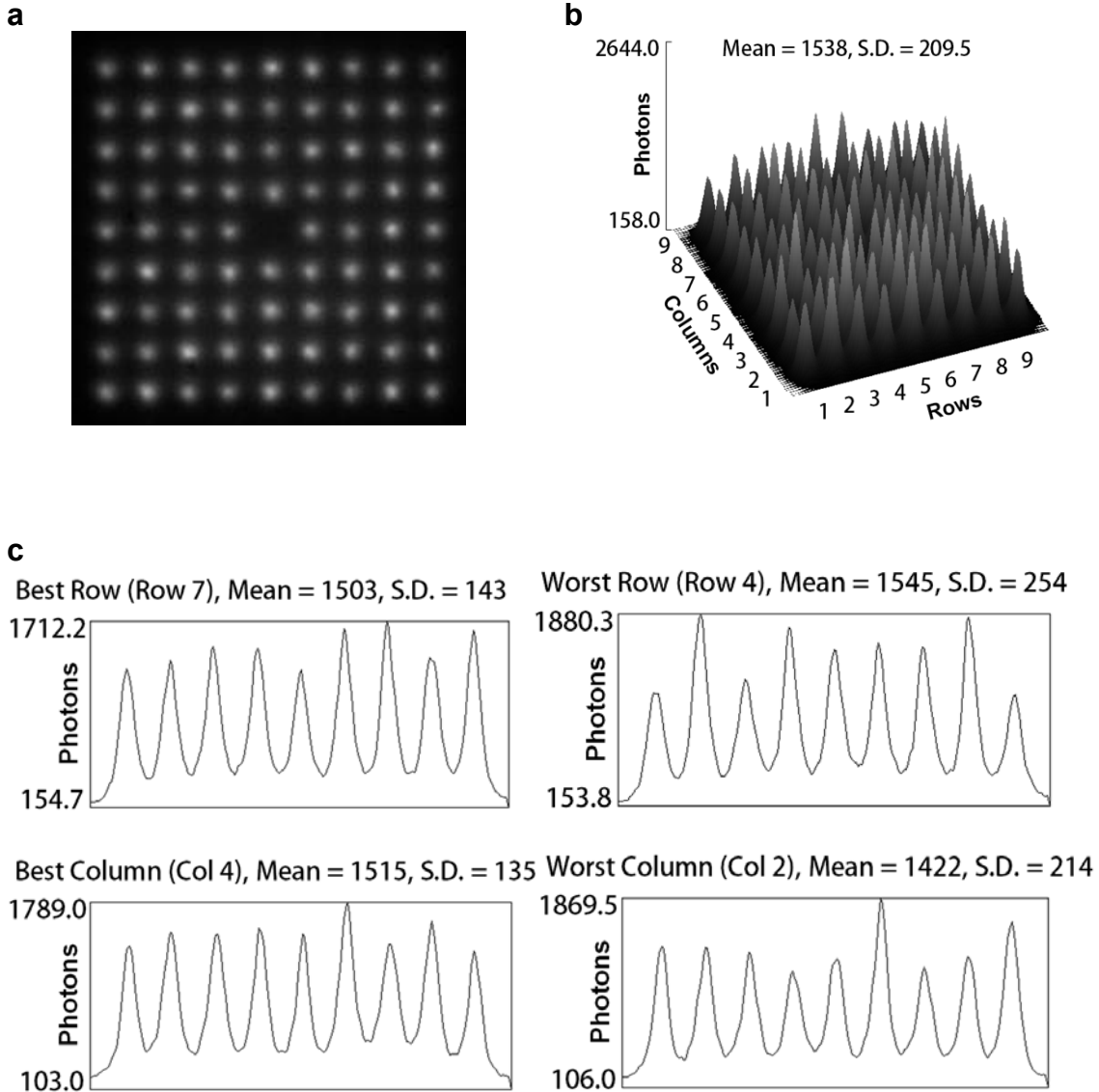
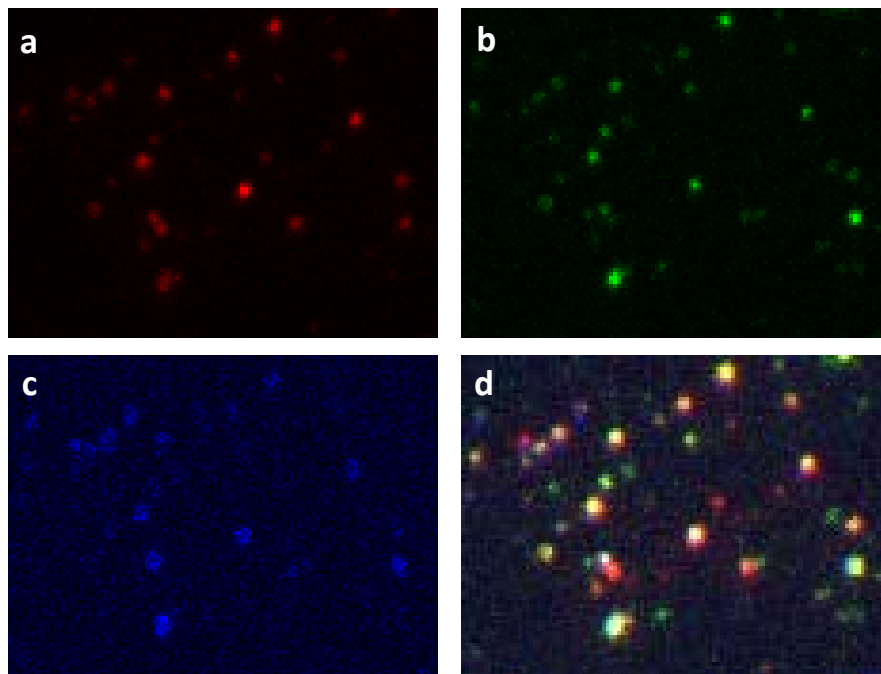


Figure 3.3 | (a) The image of excitation hologram matrix provided by the stationary holograph (Holo/Or). Taken with 1  $\mu$ M Qdot 605, laser at 785 nm. (b) 2D intensity plot of the hologram matrix in (a). SD = 15.7%. (c) Intensity plots of best and worst rows and columns in terms of uniformity.



e

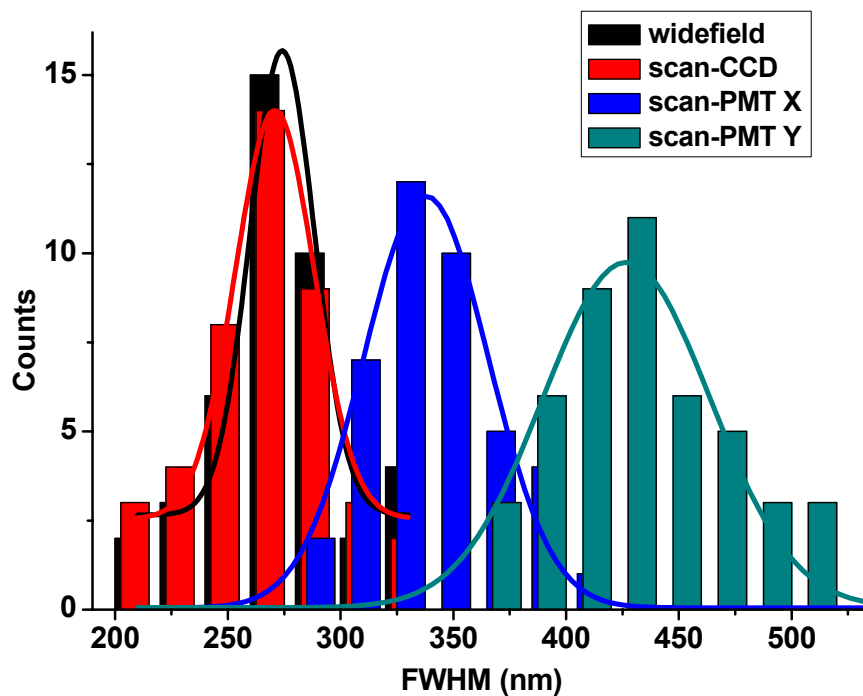


Figure 3.4 | Comparison of EMCCD and PMT imaging of 2P scan excitation. (a) Widefield and EMCCD. (b) Scan and EMCCD. (c) Scan and PMT. (d) Superimposed. (e) The histogram of the PSFs.

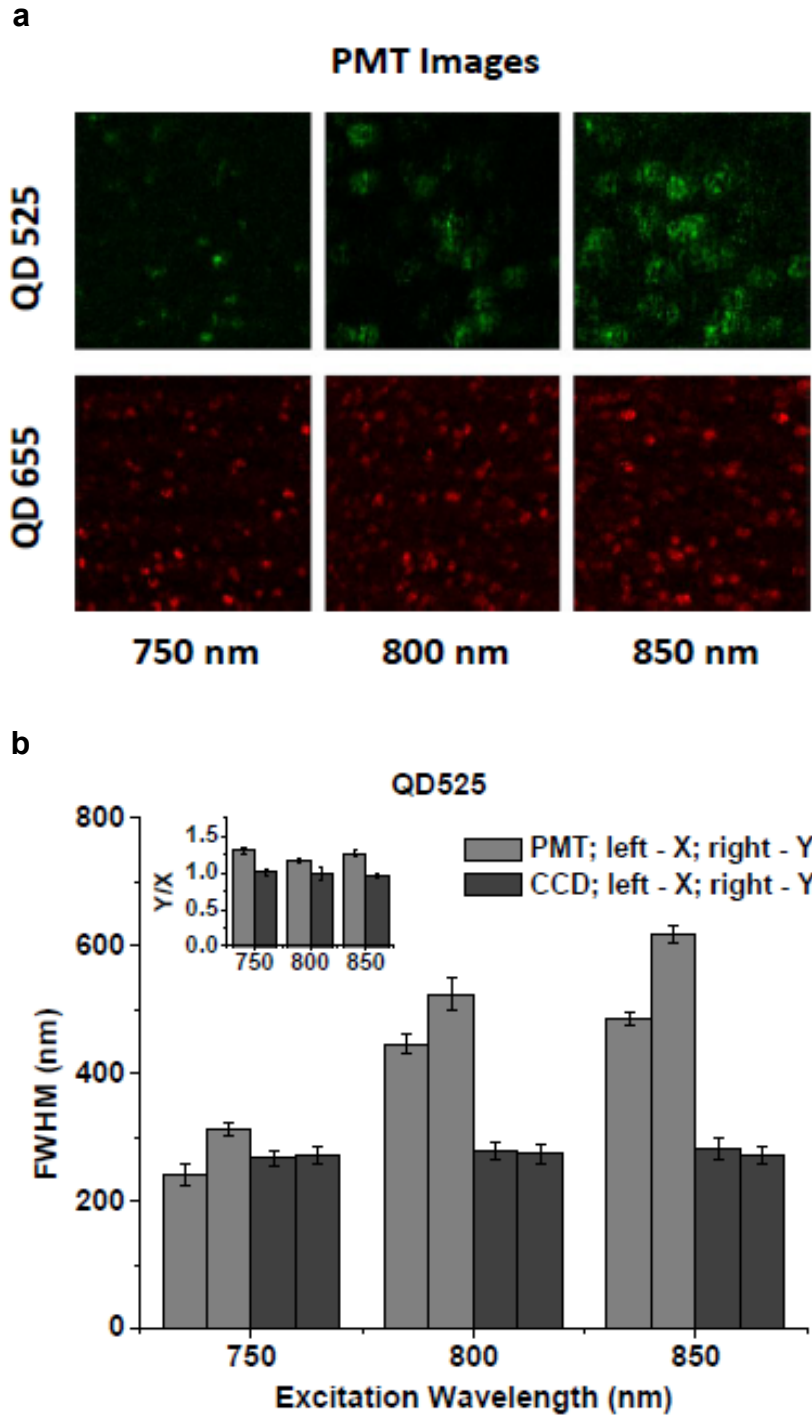


Figure 3.5 | PMT images of QD 525 and 655 at various excitation wavelengths (a) and the FWHM histograms of QD 525 (b) indicate that the expansion and the distortion of fluorescent spots as the difference between excitation and emission wavelengths increases. CCD images are not affected.

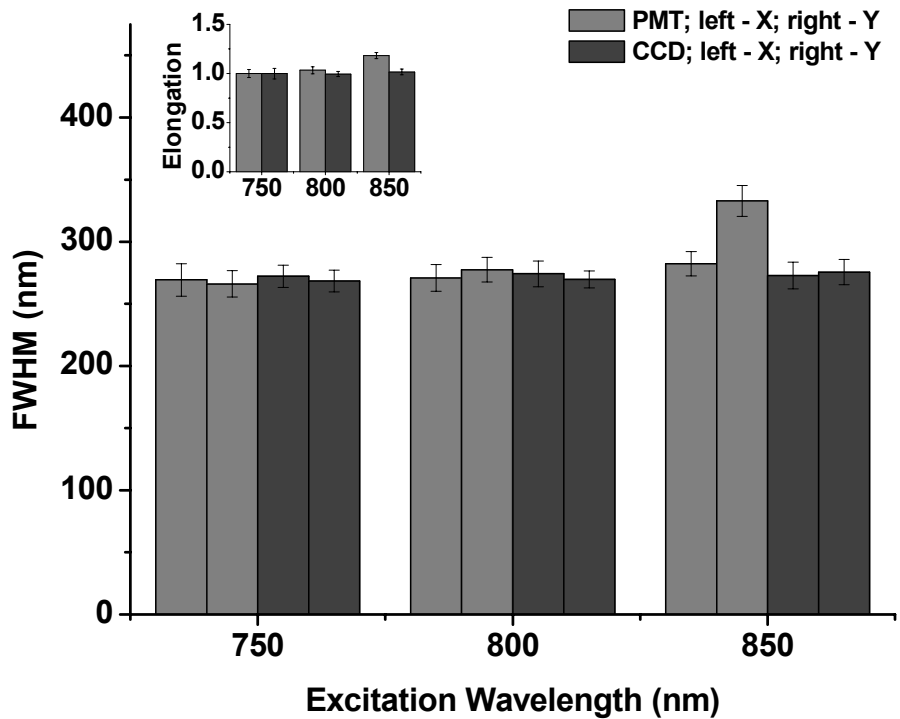


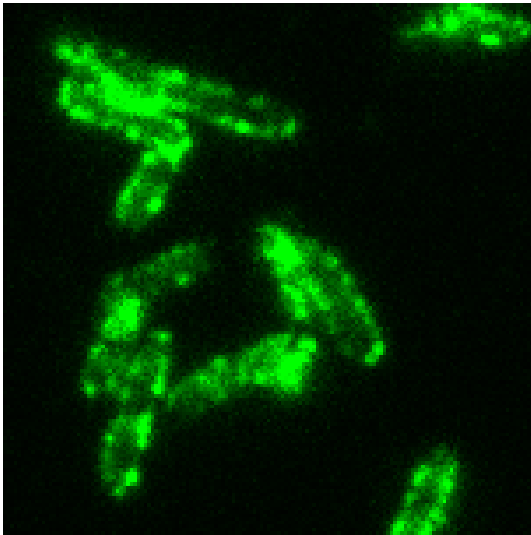
Figure 3.6 | QD655 does not expand or elongate as much as QD525 when the wavelength difference between the emission and the excitation increases.

Elongation	Qdot 525		Qdot 655	
Wavelength	PMT	CCD	PMT	CCD
750 nm	1.31	1.02	1.00	1.00
800 nm	1.17	0.99	1.03	1.00
850 nm	1.28	0.97	1.18	1.02

Table 3.1 | The expansion and elongation of single molecule QD images taken with 2P excitation and PMT.

a

CCD image



PMT image

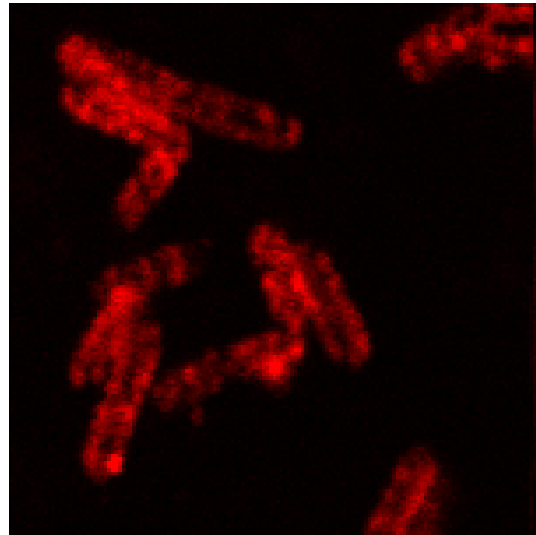


Figure 3.7 | (a) *E.coli* cells labeled with 10 nM QD565, imaged with an EMCCD or a PMT, showing the PMT does not generate any expansion or distortion. Color is false.

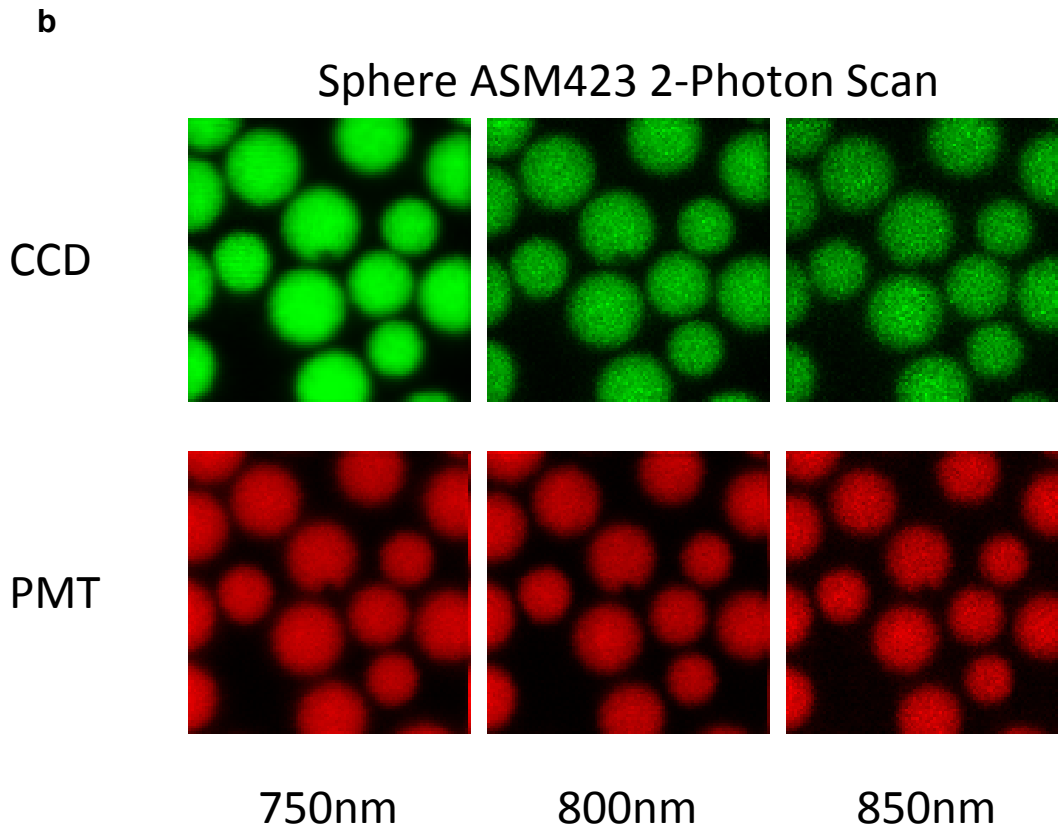


Figure 3.7 (cont.) | **(b)** ASM423 spheres excited by scanning 2P and imaged with CCD or PMT. The spots neither expand nor distort when the laser wavelength increases. Average sphere diameters is 2.31  $\mu\text{m}$ . The samples were liquid. The liquid is made up of two solvents, decalin and tetralin, into which are dispersed the polymethylmethacrylate spheres. The concentration of the two solvents is such that their mixture a refractive index of 1.5 which is the same as the spheres. 4 mL of the ASM423 colloidal solution was dropped onto slide, covered with a coverslip, wait for 5min for the solvent to partly evaporate, and sealed with Epoxy.

# Chapter IV

## Imaging of LamB Receptors on *E.coli*

### 4.1 Introduction

Viral invasion to a host cell starts with targeting and binding to a particular membrane receptor on the cell surface. LamB receptors on *Escherichia coli* (*E.coli*) bacterium has been well known as the target protein for bacteriophage  $\lambda$  to seek and attach to. The finding process may involve different types of motion of phage  $\lambda$  and different kinds of interactions between the invader and the target molecule. It was suggested that the viral motion includes three different modes [47]: free diffusion, motion on the surface of the host cells, and attachment. The model proposes that the virus first approaches a host cell by free diffusion in the aqueous solution, and then it would perform a 2D seeking along the organized LamB receptor aggregates and eventually bind to a LamB receptor with high affinity. In the second stage of the motion, the phage  $\lambda$  is kept in vicinity of receptors by the weak and reversible interaction between them.

A strong evidence of confined motion in the second stage was that the virus' movement trajectories and the spatial arrangement of the LamB receptors on *E.coli* membrane showed the same pattern. However, although the virus trajectories were able to be clearly shown by tracking the localization of a fluorescently labeled virus in a time-lapse movie via 2D FIONA, the spatial

characteristics of the LamB receptors was still imaged vaguely and with question, due to the limitation of the signal-to-noise ratio (SNR) and resolution of the epifluorescence microscopy used in the experiments [Fig. 1.6]. In this chapter, spatial characteristics of LamB receptors on the surface of *E. coli* cells will be imaged through our new 2P QD microscopy at much higher SNR and resolution. Also, in combination with a newly developed computational algorithm, the finer structure of the spatial pattern will be revealed at super resolution beyond the diffraction limit.

## 4.2 Spatial Characteristics of LamB Receptors

An *E. coli* strain, S2188:pLO16, expressing a membrane receptor LamB with a biotin molecule, was chosen [68] (a gift of S. Brown, University of Copenhagen). LamB-biotin receptors were labeled with Qdot605-streptavidin conjugates. The live *E. coli* cells are then immobilized on glass cover slips and imaged by widefield 1P with z sectioning and 2P HM scan microscopy (see Methods). We scanned *E. coli* at the same step sizes and ranges as we did breast cancer cells, taking the same amount of time. Comparing the 1P vs. 2P images (Fig. 4.1a), one can see clearly that the 1P image contains much more autofluorescence, which is virtually eliminated on the 2P image, leading to obviously higher signal-to-noise ratio. We compared the z-profile FWHM of 1P vs. 2P microscopy and found that the 2P FWHM is two times smaller (Fig. 4.1b), showing that our 2P scan method offered significantly better z discrimination. The widths of FWHMs of the spots also indicated that among those measured,

diffusion was not significant. Clear helical pattern of LamB receptors wrapping the *E.coli* cell body can be seen in figure 4.2.

We also explored the capability of our 2P technique to simultaneously image multiple colors of QDs. *E. coli* cells with biotinylated LamB were labeled with QDs emitting at 525 nm, 585 nm, and 655 nm, and excited at 785 nm by HM scan (Fig. 4.3). The emission light was detected by first passing through an Optical Insights QuadView, which splits the light according to color, and was then imaged by the EMCCD. Here just the proof-of-principle of multicolor fluorescence is shown. Neither chromatic aberration nor stage drift was attempted.

### 4.3 Materials and Methods

*Cell strains:* We used S2188:pLO16 *E.coli* to express biotinylated LamB receptors.

*Growth and Labeling of E. coli cells:* *E. coli* cells were picked up from a single colony on an agar plate and grown at 265 rpm rotation and 37°C water bath overnight in 2 mL LB media in a 14 mL Falcon tube with 34 µg/mL antibiotics chloramphenicol. The next day 25 µL incubated cells were taken and added into 5 mL LB media with antibiotics and 100 µM isopropyl-β-D-galactopyranoside (IPTG). It was then grown at 37°C water bath and 265 rpm rotation till the OD of the cell media reached 0.5 – 0.6. Cells were centrifuged in a 15 mL Eppendorf tube at 1000 rcf for 5 min and the pellet was resuspended in 1 mL pH 7.0 PBS buffer. 100 µL of suspended *E. coli* cells in PBS buffer was then added to an appropriate volume of QD-streptavidin conjugates (Invitrogen), and

they were then let sit in RT for 10 min. Different kinds of QDs (525/565/605/655 nm or a combination) were selected as needed. 10 nM QDs were used to get dense labeling, while 1 nM or 100 pM were used to obtain single QD labeling. Labeled cells were centrifuge at 1000 rcf for 5 min and then washed by resuspending the pellet with 200  $\mu$ L of pH 7.0 PBS buffer and repeated 3 to 5 times.

*E. coli and breast cancer cells imaging:* Labeled living *E. coli* cells were self-adhesive to the glass surface, and sealed between a coverslip and a slide. The cell sample was excited by a diffraction-limited excitation spot (single-point scan) or a holographic matrix of multiple spots (multi-point matrix scan), as described in the Material and Methods in the previous chapter. Laser power was tuned to ensure enough emission intensity while keeping excitation outside the diffraction limited spot to minimum. The scan range and step size, were predetermined according to the need of the experiment. Most used scan step sizes are 50 nm, 64 nm, or 100 nm. Residence time on each scan pixel was from 0.02 msec to 1 msec. Brightfield images of cells were also taken to show the profile of the whole cells.

## 4.4 Figures

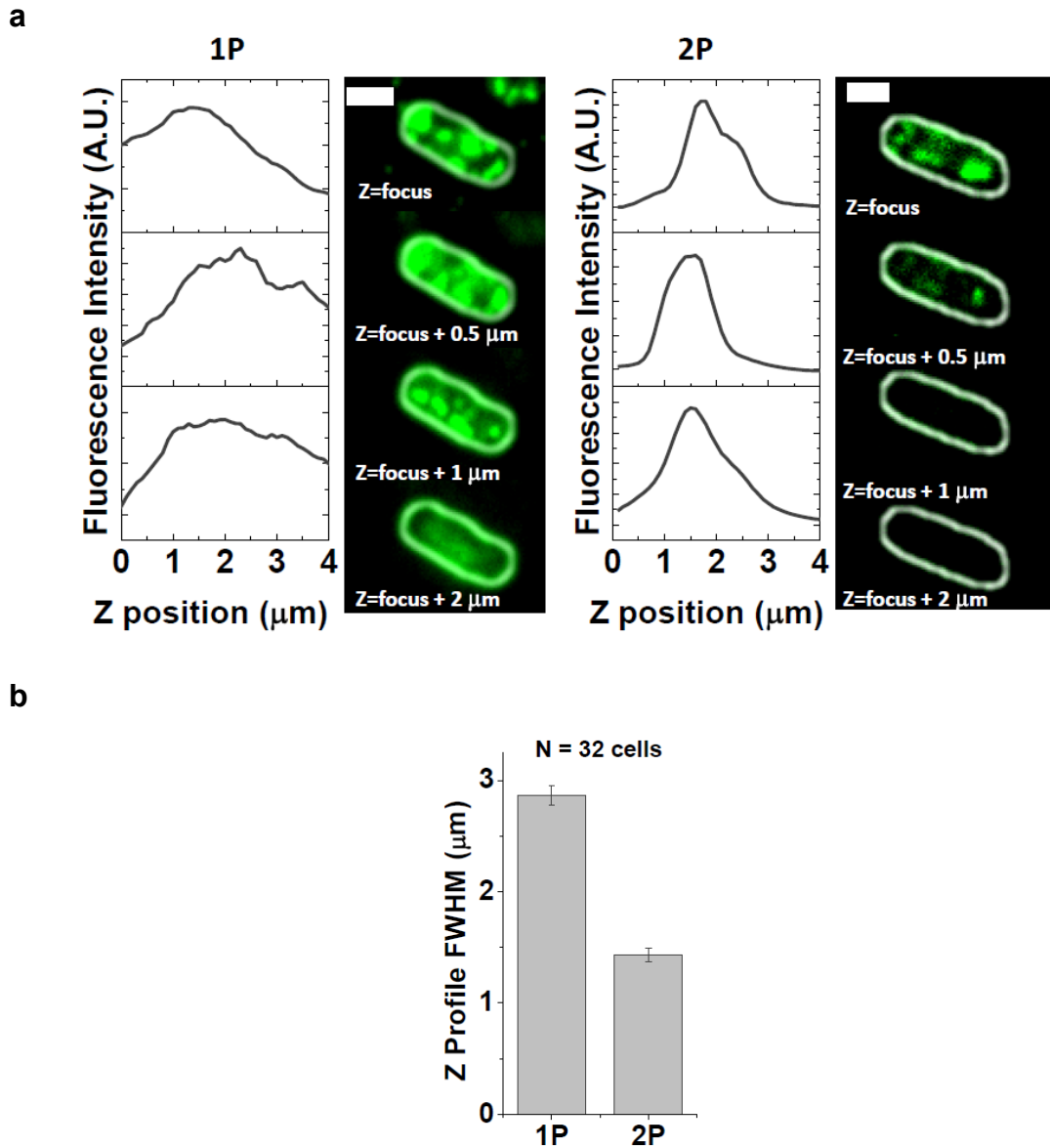
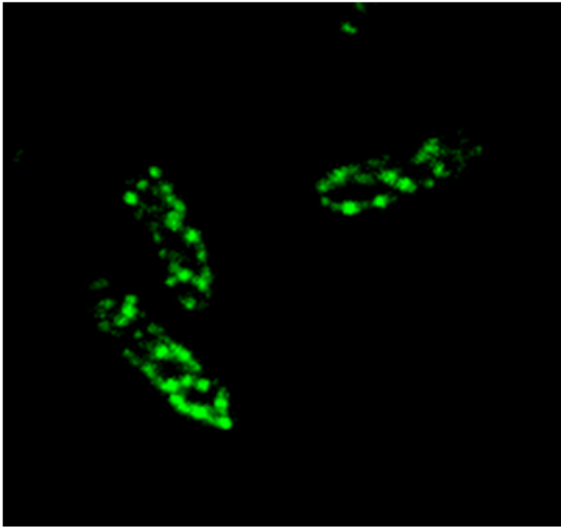


Figure 4.1 | 2-photon matrix vs. 1-photon wide-field sectioning at different z positions of E.coli cells labeled with 10 nM QD655 on LamB receptors. (a) Three representative individual cells from each microscopy. (b) An average of 32 cells from each. The sharper drop-off with z for the 2P indicates that the 2-photon scan excitation yields 2 folds better z discrimination.

## 2-Photon



## 1-Photon

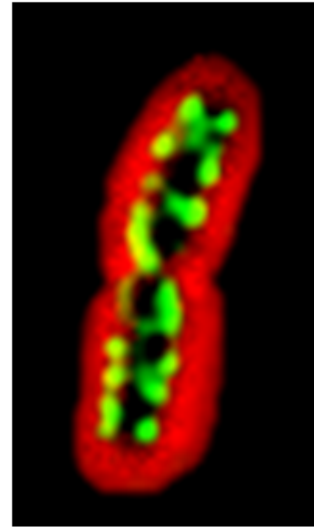


Figure 4.2 | Helical spatial organization of LamB receptors on E.coli cells imaged by 2-photon quantum dot hologram scan microscopy (left) and conventional 1-photon epifluorescence microscopy (right).

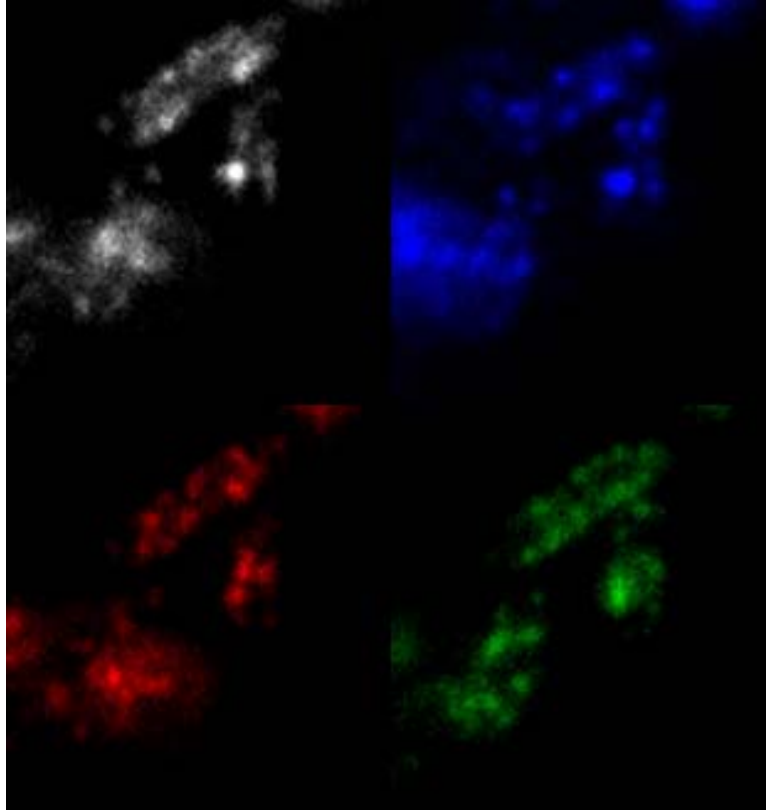


Figure 4.3 | *E. Coli* cells labeled with Streptavidin-QDs (10 nM of each color) emitting at 525 nm (red), 565 nm (blue), 605 nm (green) and 655 nm (red) (artificial colors) and excited with 800 nm. Detection was with a QuadView (Photometrics).

# Chapter V

## EGFR and c-Met in Human Breast Cancer Cells

### 5.1 Introduction

Epidermal growth factor receptor (EGFR, or ErbB-1, or HER-1 in human cells) and hepatocyte growth factor receptor (HGFR, or c-Met) both play important roles in cell growth and life cycles. Dysregulation of the receptors, e.g. over-expression or constitutive activation, can induce malignant proliferation, abnormal angiogenesis and uncontrolled metastasis of cells, promoting formation of tumor. Therefore, both of them have been the hot topics in the researches for cancer pathogenesis and therapy. So far the signal transduction pathways of the two types of receptors have both been well studied. The pathway cascades can be seen in figure 5.1 [69]. Briefly, EGFR and HGFR are both receptor protein-tyrosine kinases (RTK). Inactivated EGFRs are usually trans-membrane monomers. Once bound with EGF, they will homo-dimerize and the intracellular part will take self-phosphorylation on the tyrosines near its c-terminus and get thus activated, and then initiate a cascade of signal transduction, leading to cell growth, mitosis, cell proliferation and metastasis. HGFR, or c-Met, has the similar tyrosine kinase mechanism to regulate a variety of pathways.

A noticeable discovery about the two receptors is that they do not only perform their roles on the cell membrane, but also travel into the cell plasma

while continue to function (Fig. 5.2). The activation of EGFR leads to self-phosphorylation and ubiquitylation of the receptor, which might result in the EGFR dropping out of lipid membrane and internalized into the cell plasma in the form of endosomes (Fig. 5.2a) [70]. In the early endosomes, the tyrosine kinase tail of the EGFR remains active, projecting to cell plasma the outside of the endosome compartment, and continues to function in signal transduction. This is the positive effect of endocytosis on EGFR signaling. The early endosomes then have several choices. They can be either recycled to the cell membrane, or be sorted to the late endosomes. It is suggested that in the late endosomes more vesicles of EGFR are clustered together and formed multi-vesicular bodies, of which the kinase tail of the EGFR is occluded from the cytoplasm into the endosome compartment and thus no signaling pathways can be activated by the EGFR any more. Then the late endosomes will fuse with lysosomes and get degraded, reducing the level of EGFR in the cell, showing down-regulation of EGFR. This degradation is the major negative feedback in the regulatory network of EGFR signaling. A third possibility for the early endosomes of EGFR is that they can be transported into the nucleus. The route still remains unclear, but it may potentially regulate the gene expression and replication directly, playing a very critical role in cell proliferation and differentiation. For c-Met, its endocytosis is required to activate both ERK1/2 and STAT3 signaling (Fig. 5.2b) [71], the latter of which may also involve a microtubule-dependent perinuclear localization of c-Met. In cancer therapy, targeting c-Met is more and more used as a strategy to overcome the resistance to EGFR inhibitor caused by crosstalk activation.

It has been suggested that EGFR and c-Met might form homo-clusters or even co-localize in a hetero-cluster with or without endocytosis activated by ligand binding. Investigation in the dimerization, clustering and transportation of the both receptors will be enlightening for the breast cancer pathogenesis and therapy. Using our high resolution 2-photon quantum dot hologram scan microscopy, we can study the EGFR locations and traffic, would open up the possibility to assess precise monomer-dimer-oligomer transitions of these receptor molecules in live cells in the presence or the absence of stimuli [72-74]. In this chapter, the application of our new 3D 2-photon microscopy on the quantum dots-labeled EGFR and c-Met in unstimulated and stimulated breast cancer cells will be described and discussed. For instance,

## 5.2 Imaging Individual QD-labeled Receptors

We first compared 2P to 1P imaging of single quantum dots labeling EGFRs on fixed breast cancer cells in order to demonstrate the imaging capability of the 2-photon fast scan technique. We chose a basal breast cancer cell line, MDA-MB-468, to express two members of epidermal growth factor receptors family, ErbB1 (EGFR) and ErbB3, which bind to EGF. Cells were grown on glass cover slips, then fixed and stained with a pre-formed complex of EGF-biotin/streptavidin-QD655 before being mounted in CyGEL (Biostatus, Ltd.).

Subsequently, cells were imaged with a widefield 1P setup with 532 nm laser epifluorescence excitation while other cells were subjected to 2P hologram (HM) multipoint scanning microscopy at 785 nm excitation (Fig. 5.3a). In both

cases brightfield images were also taken to provide an overall picture of the cells. All images were recorded with the EMCCD. The x-y and z scan step sizes were 64 nm, scanned for 25 steps, or a total of 1.6  $\mu\text{m}$ , in x-y and 3~4  $\mu\text{m}$  in z. So the x-y coverage is 1.6  $\mu\text{m}$  x 9 = 14.4  $\mu\text{m}$ , enough to cover a whole breast cancer cell. As shown in figure 5.3a, the 1-photon epifluorescence image showed large autofluorescence, which was greatly reduced in 2P scanning. This makes the average signal-to-noise ratio to increase, from 2:1 to 6:1, respectively (Fig. 5.3b). Individual labeled EGFRs were clearly resolved (Fig. 5.3a). A high resolution 2P 3D whole image of an EGF-QD655 labeled breast cancer cell was obtained within a few (2~5) seconds for hologram scanning (depending on the residence time on each pixel), while the regular single-point scanning took 3~7 min.

Cells treated with just quantum dots (not conjugated to EGF) were also tested as a control. No labeling of quantum dots on the cell was observed, proving the quantum dots on the cells represent EGFR molecules.

### 5.3 2P QD Hologram Scan Microscopy in Combination with PhILM

When the fluorophores are at small density, each of them separated more than about 200 nm away, they can be localized with at the resolution much higher than diffraction limit – in fact, one nanometer accuracy can be achieved. This is aforementioned Fluorescence Imaging with One nanometer Accuracy, FIONA. However, when the fluorophores are labeled at high density and separated less than about 200 nm, the fluorescence spots would “overlap” with one another, causing the PSFs in the raw data images not able to be fitted with

2D Gaussian, so that the FIONA cannot be directly applied to get super-resolution of them.

Some advanced techniques have been developed in the past few years to break through the obstacles in obtaining super-resolution fluorescence images. PALM [17], FPALM [18] and STORM [19-21] share the same principle but use different types of fluorophores. The former two use fluorescent proteins while the third uses organic dyes. They all rely on the photoactivatability or the photoswitchability of the fluorophores [75, 76]. At one time, only a small fraction of densely labeled fluorophores are driven from “off” state to “on” state by a burst of the activation laser, and excited by another excitation laser at a different wavelength and imaged. Therefore, the image will contain sparse fluorescent spots which can be localized individually with FIONA. This process will repeat for many cycles and stochastic fractional populations of fluorophores are activated in each cycle so that every single fluorophore, theoretically, will be imaged individually at least once and get localized at super-accuracy. The stack of super-accuracy images of sparse fluorescent spots are summed up and the ultimate super-resolution image of all densely-labeled fluorophores are eventually generated (see figure 5.4 [17] for the example of PALM).

However, the PALM and the STORM are both limited to special subsets of fluorophores as they require the fluorophores can be reliably photo-activatable for many cycles. Only a limited set of fluorophores meet the requirement. Also, the necessity to use double laser increase the complexity of instrumentation and the difficulty for biologists to use in their laboratories. Another powerful super-

resolution technique, stimulated emission depletion microscopy [77], or STED, does not need single molecule imaging but requires even more complicated physics knowledge and optical instrumentation, and may cause severe photo-damage to biological samples.

A new super-resolution technique has been developed in our lab [22] which uses only single laser excitation and does not require particular photo-activatable fluorophores. The technique, photobleaching and intermittency localization imaging, or PhILM, is based on an earlier developed sub-diffraction limit distance measurement technique developed in our lab, single-molecule high-resolution imaging with photobleaching, or SHRImP [26]. The flowchart in the figure 5.5 [22] explains the principle of PhILM algorithm. Briefly, for two closely located fluorescent spots, one of them may naturally photobleach first or take a blink at one time point, and left the other as a single fluorescent spot that can be accurately localized by normal FIONA. Then by subtracting the PSF of the remained spot from the total two-spot PSF in the image before photobleaching or blinking, we can obtain the single-spot PSF of the gone spot itself, and localize it again with FIONA. In the computation program, a series of new images are first generated by backwards-subtraction (step 2 in Fig. 5.5) of the original time-lapse image stack (step 1 in Fig. 5.5) to find the single-spot PSFs of individual fluorophores as mentioned above (step 3 in Fig. 5.5), and each of them is then fitted by FIONA for accurate localizations (step 4 and 5 in Fig. 5.5). Eventually, we are able to determine the distance between the two close and “overlapping” spots and generate a super-resolution image of both of

them (step 6 in Fig. 5.5). The ultimate super-resolution image of tons of densely labeled fluorophores can be obtained with the same algorithm.

Attributed to the intrinsically stochastic blinking characteristic of quantum dots, they are superb fluorescent probes to reach super-resolution through image analysis of stochastic events [78, 79], e.g. PhILM technique. Here the intermittency, instead of photobleaching in the images of organic-based fluorophores, becomes the predominant source of stochastic single molecule localization to produce the super-resolution. Thus the photo-damage to the fluorescently labeled samples is minimized and the sample could be used for more than once. The 2-photon quantum dot scan microscopy, in combination with PhILM, provides a way to look into the deep inside of biological samples with high resolution.

PhILM, currently still limited to 2D resolution, requires a stack of images at the one focal plane. So the scan and acquisition modes are modified that at each z position, 100 or 200 repeats of whole x-y 2D scan were completed and recorded as a 100 or 200-frame stack of images, and then the piezo-stage steps to the next z and repeat the multi-frame scan and data acquisition. The scan step size in all three dimensions are set to be all 64 nm or all 100 nm. 2D PhILM is applied on the stack of images at each z section to generate a “semi-3D” super-resolution image composed of a stack of 2D super-resolution images at all z positions.

## 5.4 Endocytosis of EGFR

To validate the endocytosis of EGFR, the imaging tool must be able to clearly discriminate fluorophores at different z heights as well as x-y positions. Conventional wide-field microscopy cannot satisfy the need. Our 2-photon 3D fast hologram scan microscopy is potent in locating the positions of a particular fluorescent spot not only in x-y planes but also in z direction, so as to determine whether it is on the top membrane, on the bottom membrane, on the side membrane or inside the cytoplasm of the cell.

We first treated the living breast cancer cells with 4 nM QD605-EGF conjugates to activate the EGFR, and then fixed the cells and mounted with CyGEL. Images were taken with 2-photon 3D hologram scan microscopy. For the purpose of doing PhILM, at each z section, the x-y scan was repeated for 100 times and 100 frames of images were acquired accordingly by the EMCCD camera. Figure 5.6a upper panel shows the receptors at different z planes. The image at  $z = 0 \mu\text{m}$  shows the first plane in the scan where tons of receptors locate in-focus, indicating the bottom membrane of the cell. The image at  $z = +0.8 \mu\text{m}$  proves the existence of endosomes of EGFR. The QD-labeled receptors on the edge of the image might still be argued as attaching on the side membrane of the cell, but the receptor clusters in the middle are clearly located in the cytoplasm and are endosomes of EGFR. The third image at  $z = +1.3 \mu\text{m}$  apparently represents the EGFR on the top membrane of the cell.

Two-dimensional PhILM was then applied to the stacks of images at each z section, giving super-resolution images of all EGFR molecules on the cell

surface or in the cytoplasm (Fig. 5.6a, lower panel). Apparently, in the stimulated cell, almost all EGFR molecules formed multi-receptor clusters. The super-resolution structure of an EGFR endosome, marked in the yellow square in figure 5.6a, is shown in figure 5.6b. The big single fluorescent spot in the original 2-photon scan microscopic picture is revealed to contain 6 activated EGF receptors. The 2D positions of them, as well as the distances of them (more accurately, their projections in this x-y plane), are listed in the table 5.1. From the FWHM we can tell the third and the sixth (counting from left to right) receptors may be out of focus, suggesting that they are actually located in other planes. The accurate z position can be localized by comparing the broadened FWHM of the defocused spots, though a simpler and more direct method to determine the z positions will be discussed in next chapter. The resolution reaches 20 nm, indicating our 2-photon quantum dot hologram scan microscopy, in combination with PhILM, is satisfyingly capable of resolving the structure of the EGFR clusters and the separation between the receptor monomers.

## 5.5 Colocalization of EGFR and c-Met in Clusters

The HGF receptor, c-Met, plays a similarly important role in tumor development with EGFR. Actually, in cancer therapies, targeting c-Met is increasingly used to avoid crosstalk-related drug resistance to EGFR inhibitors. However, it still remains ambiguous whether the two receptors meet together to signal the cascade of pathways.

We applied our 2-photon hologram scan microscopy on breast cancer cells whose EGFR and c-Met were labeled with two colors of quantum dots. To compare the distributions of them before and after activation, we made and imaged two kinds of cell samples. The stimulated cell sample was first treated and stimulated with both QD605-EGF and QD655-HGF conjugates, and then were fixed and mounted in CyGEL. The unstimulated cells were first fixed and then stained with QD605-EGF and QD655-HGF, and mounted in CyGEL. Figure 5.7 shows the images of both cell samples. It is very clear that in the unstimulated cell, most EGFR and c-Met distribute in different locations, except only a few of them are co-located in the same clusters (Fig. 5.7a). In contrast, surprisingly, the stimulated cell has almost all activated EGFR and c-Met trafficked to and aggregated in the same clusters (Fig. 5.7b).

The control experiment showed no fluorescence leaking between the 605 nm channel and the 655 nm channel, proving that the observed colocalization of the two types of receptors were not caused by experimental error.

Our results clearly indicate that the activated EGFR and c-Met move to the same locations to signal the cascade of pathways. How this phenomenon is triggered remains yet to be studied. The discovery shed a light on the understanding of the mechanism of the two receptor tyrosin kinases in tumor pathogenesis and therapy.

## 5.6 Materials and Methods

*Cell strains:* We used MDA-MB-468 adenocarcinoma as an example of a human breast cancer cell line expressing elevated levels of EGFR.

*Breast Cancer Cell Growth and Labeling:* MDA-MB-468 cells were cultured in L-15 medium (PAA, Farnborough, UK) supplemented with 10% fetal calf serum. Cells were plated onto sterile glass cover slips, fixed with 4% (w/w) paraformaldehyde for 15 min at RT before being treated with sodium borohydride (1 mg/mL in PBS, pH 7.4) to reduce free aldehyde groups, and blocked with 1% bovine serum albumin containing 100 nM streptavidin for 30 min at RT. Subsequently, cells were stained for 45 min at RT in the dark with 1 nM pre-formed EGF-Qdot complexes, which were prepared using EGF-biotin and a streptavidin-QD655 conjugate (both from Invitrogen, Paisley, UK) as described earlier[80]. Cells were extensively washed with PBS (5 times) before they were mounted in CyGEL (Biostatus Limited, Leicestershire, UK).

*Breast cancer cells imaging:* Fixed labeled breast cancer cells were mounted in CyGel and sealed between coverslip and slide. The cell sample was excited by a diffraction-limited excitation spot (single-point scan) or a holographic matrix of multiple spots (multi-point matrix scan). Laser power was tuned to ensure enough emission intensity while keeping excitation outside the diffraction limited spot to minimum. The scan range and step size, were predetermined according to the need of the experiment. Most used scan step sizes are 50 nm, 64 nm, or 100 nm. Residence time on each scan pixel was from 0.02 msec to 1 msec. Brightfield images of cells were also taken to show the profile of the whole

cells. For two-color imaging of QD605 and QD655 labeled cells, a DualView tube (Photometrics) was installed to the microscope, and FF01-605/15-25 or FF01-655/15-25 single band emission filters (Semrock) were included in the tube for the dual color filtering of QD605 and QD655.

## 5.7 Figures and Tables

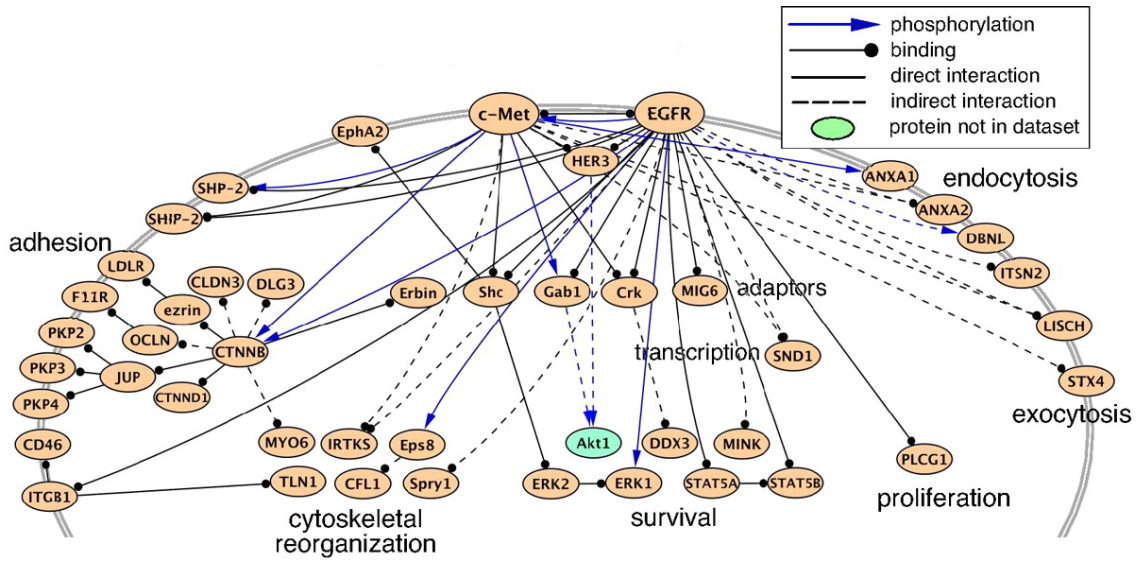


Figure 5.1 | Regulatory networks sensitive to EGFR and c-Met in H3255 and MKN45 cells. Signaling pathway connections are from PhosphoSite (31), with additional protein–protein interactions extracted from PROTEOME.

a

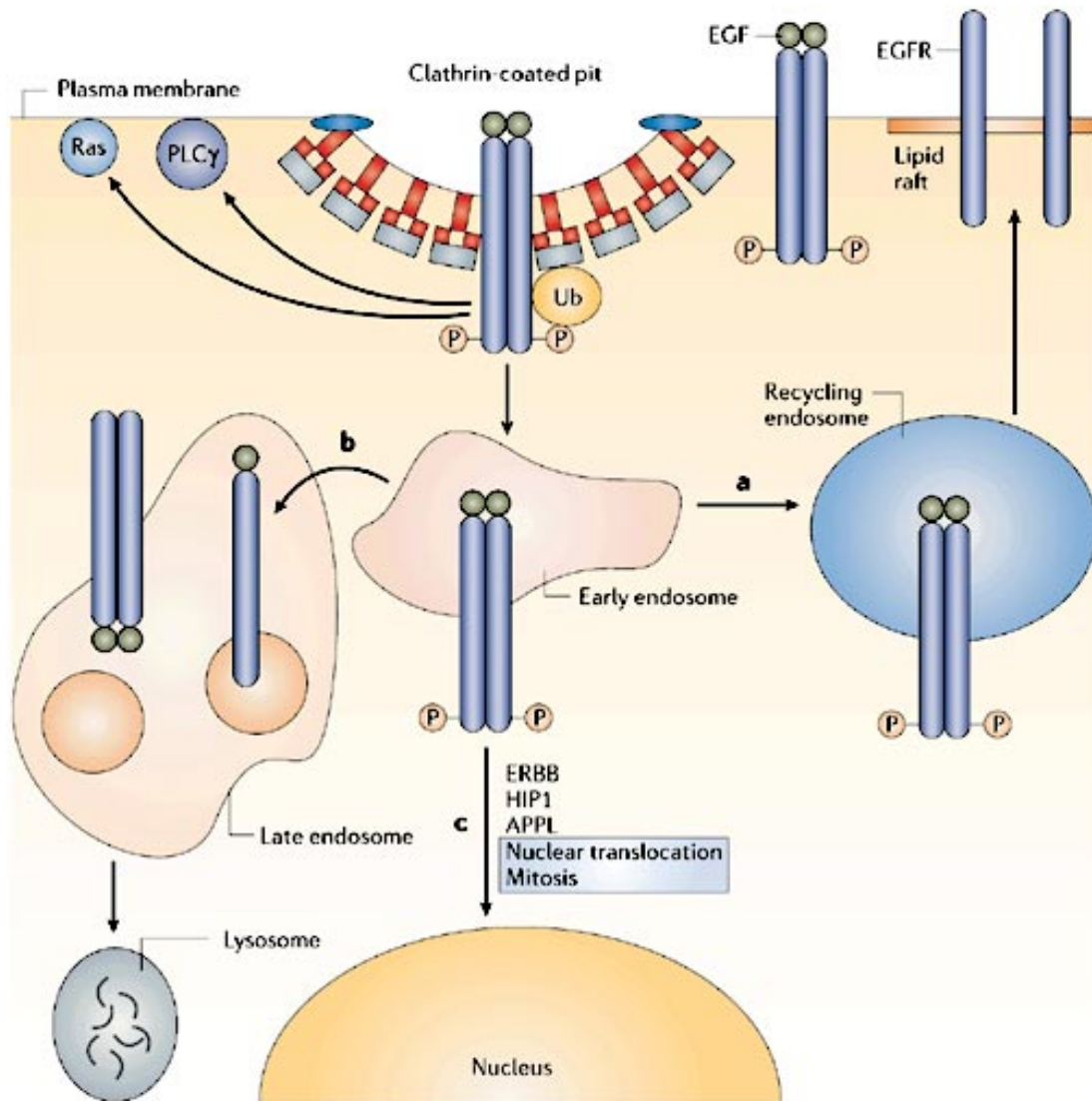


Figure 5.2 | (a) EGFR trafficking. EGF binding causes the receptors to form homodimer and perform auto-phosphorylation and ubiquitylation. The activated EGFRs are endocytosed as early endosomes, in which the EGFR continue to signal. Then the internalized EGFRs are either recycled to the cell surface, or sorted into late endosomes and degraded, or transported into nucleus, directly regulating gene expression and replication there.

b

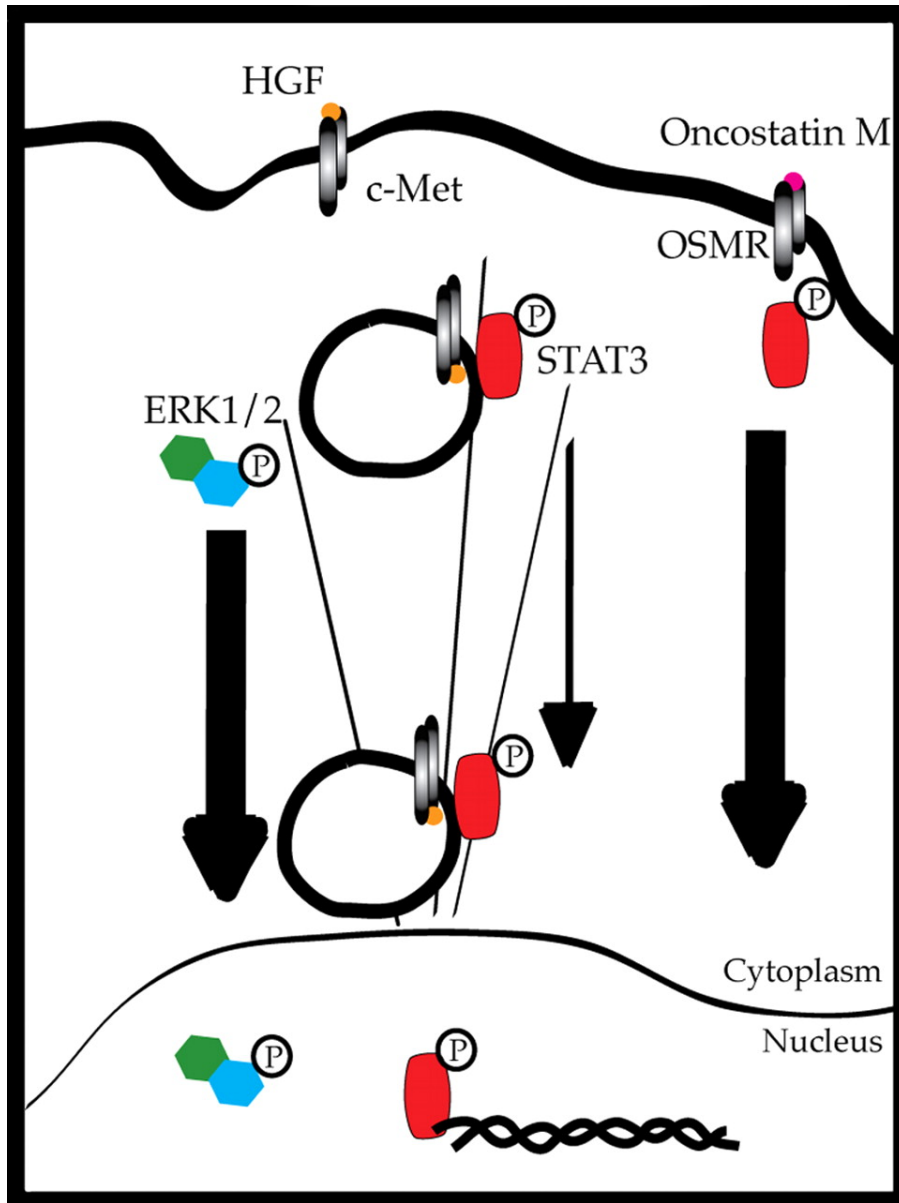


Figure 5.2 (cont.) | (b) The endocytosis of HGFR, c-Met, is required for both ERK1/2 and STAT3 signaling. The signal strengths are different for the two pathways. The ERK1/2 signal is strong and can proceed with cytosolic diffusion, whereas the STAT3 signal is weak and thus requires a microtubule-dependent perinuclear localization of c-Met.

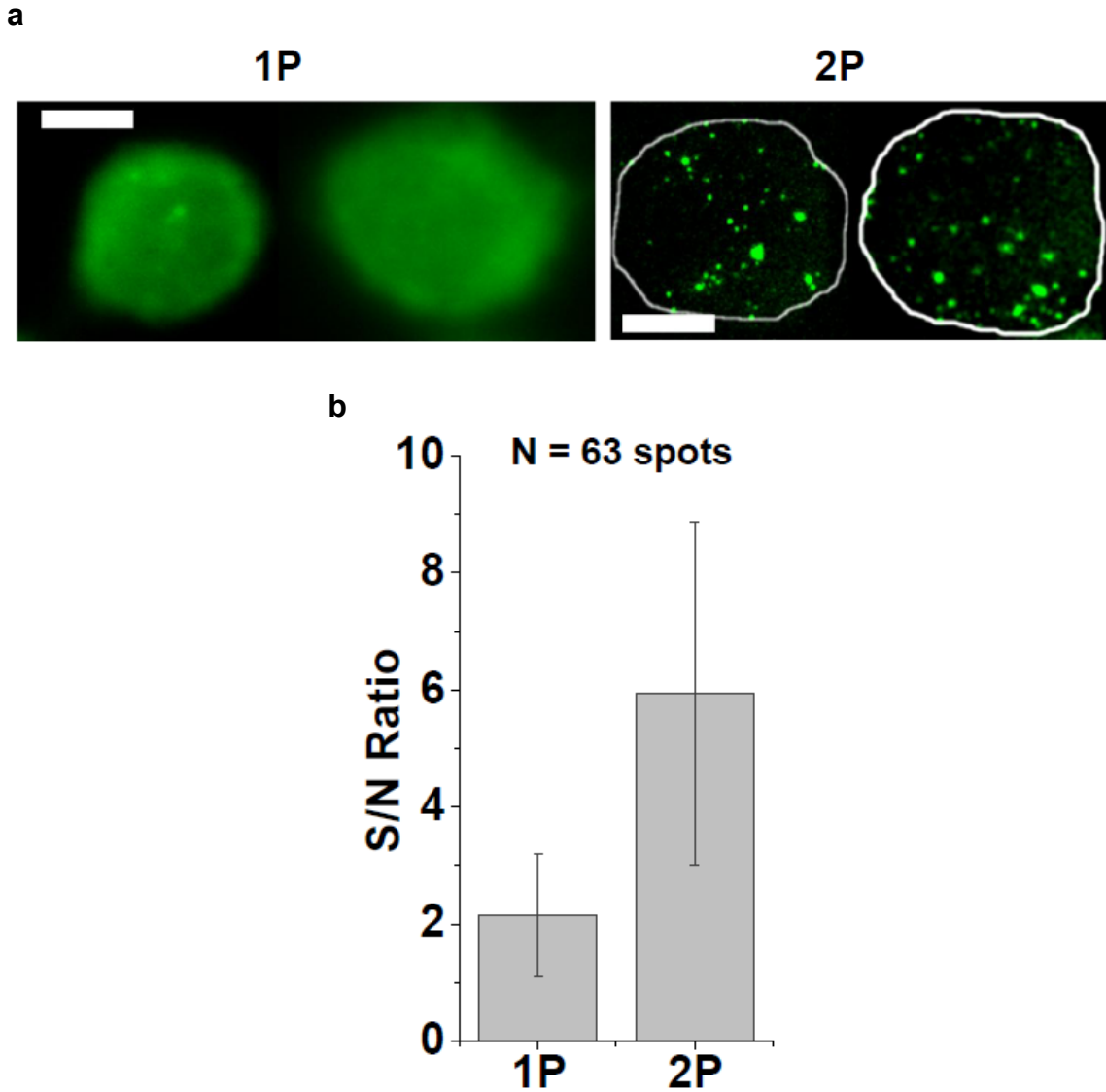


Figure 5.3 | QD-labeled breast cancer cell imaging by 2-photon hologram scan and 1-photon widefield excitations. **(a)** Fixed breast cancer cells labeled with EGF-QD655 conjugate. With 1-photon, there is a tremendous amount of autofluorescence. With 2-photon microscopy (hologram scan method), the autofluorescence background is significantly diminished and individual EGF-QDs can be visualized. **(b)** Signal to noise ratio is increased from 2:1 to 6:1.

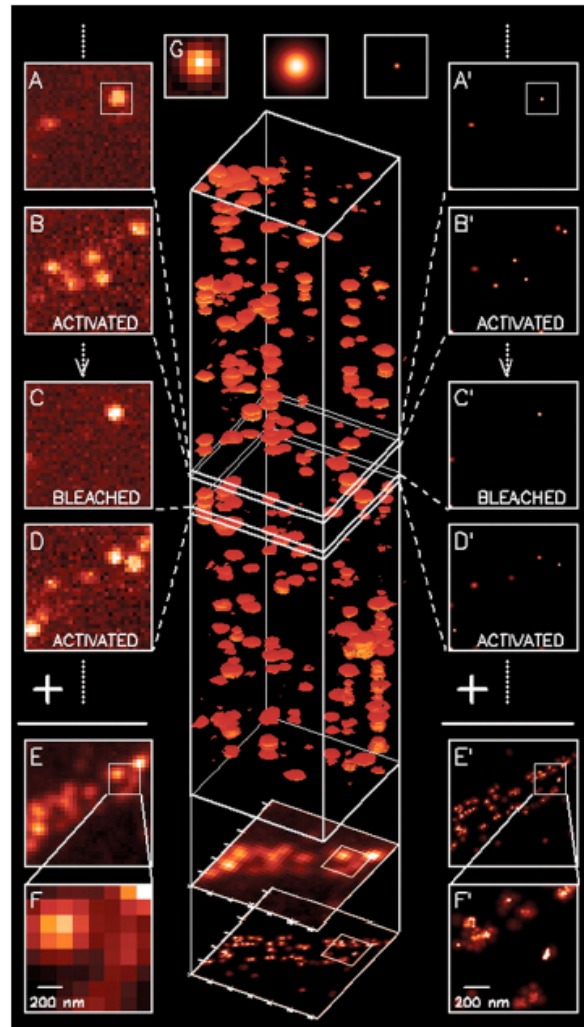
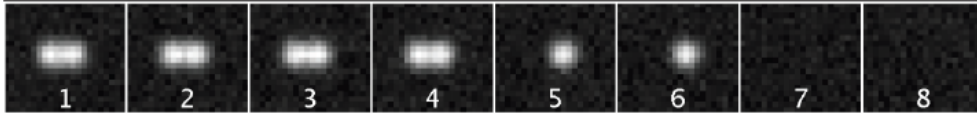


Figure 5.4 | A flowchart illumination of PALM principles. (A – D) Each time a small subpopulation of photoactivatable fluorescent proteins are activated, imaged and bleached. The process repeats for many cycles to produce a summed image of all densely labeled fluorophores (E, F). (G) One single fluorescent spot can be fitted with 2D Gaussian, localized to high accuracy via FIONA and then plotted. (A' – D') Localizing and plotting all the single fluorescent spots in each imaging cycle will result in the ultimate super-resolution image with all densely labeled fluorescent proteins finely localized.

## The PhILM algorithm

Simple example:

1. Start with a two-fluorophore image sequence with photobleaching (frames 4 and 6):



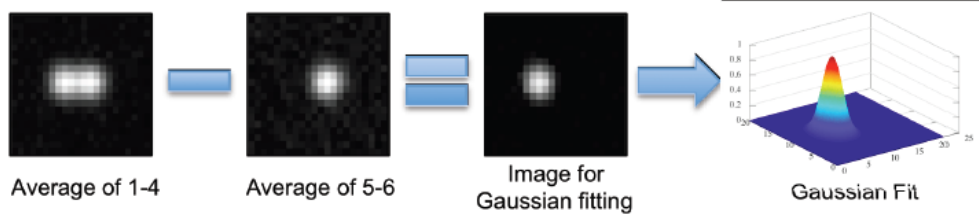
2. Create the backwards-subtracted image sequence by subtracting frame 8 from 7 to get new frame 7', 7 from 6 to get new 6', etc.:



3. Locate spots in the backwards-subtracted image sequence. These show when and where photobleaching occurred (here, frames 4 & 6):



4. Localize the first photobleaching fluorophore by subtracting the average of frames 5-6 from the average of frames 1-4, then fitting to a weighted 2-dimensional Gaussian:



5. The center of the Gaussian fit is the location (within fit error) of the fluorophore. Repeat for the second fluorophore but subtract the average of frames 7-8 from the average of 5-6.

6. Plot the locations of the fluorophores in the new, super-resolution image!

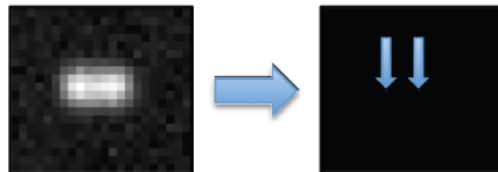


Figure 5.5 | Algorithm of PhILM. A set of Images containing a subpopulation of the fluorophores that switch from on to off (photobleaching and blink on) or switch from off to on (blink on or photoactivation) before and after the cut-point of image subtraction can be generated (step 1 – 3). The sparse spots in the subpopulation are then localized to high accuracy via FIONA and plotted (step 4 – 6).

**a**

### EGFR in Stimulated Breast Cancer Cell

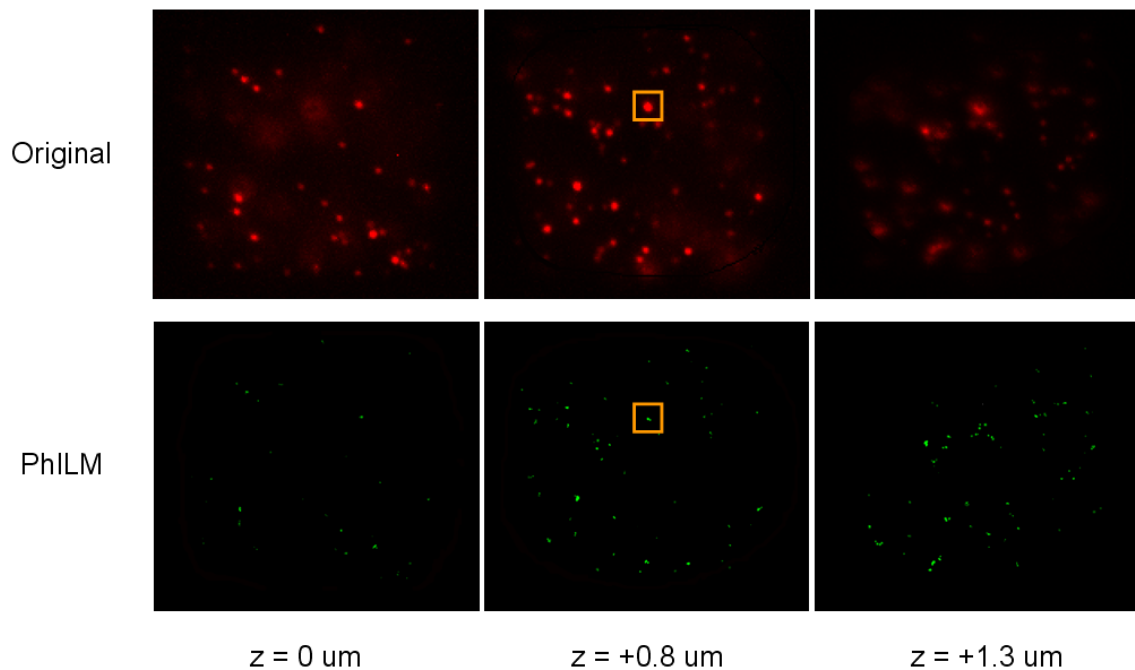


Figure 5.6 | Ligand-activated EGFR are endocytosed in an EGF stimulated breast cancer cell. **(a)** Images at different z sections. Image at  $z = 0 \text{ um}$  shows the bottom membrane of the cells. Image at  $z = +0.8 \text{ um}$  indicates EGFR clusters in the plasma of the cell, i.e. they are endocytosed. Image at  $z = +1.3 \text{ um}$  shows the top membrane of the cell. PhILM was applied to generate super-resolution images for all z sections. The cell sample was first treated with 4 nM QD605-EGF to stimulate and activate the EGFRs, and then the cells were fixed and mounted in CyGel.

**b**

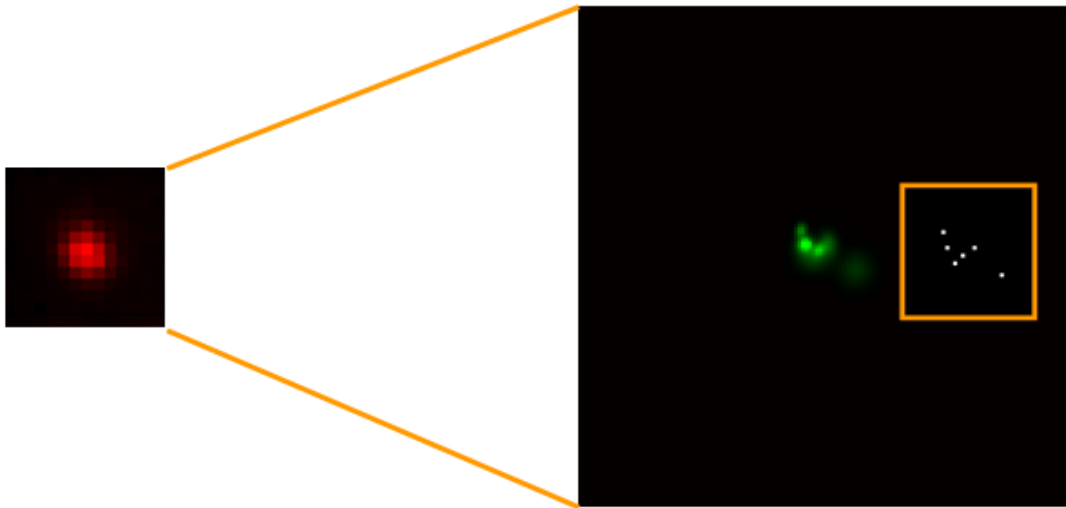


Figure 5.6 (cont.) | **(b)** A particular endosome of EGFR in the plasma. The PhILM image reveals it contains 6 receptors, the spatial arrangement marked as white dots in the yellow square on the side of the PhILM spots. Localizations of the spots and distances between them can be found in Table 5.1.

**c**

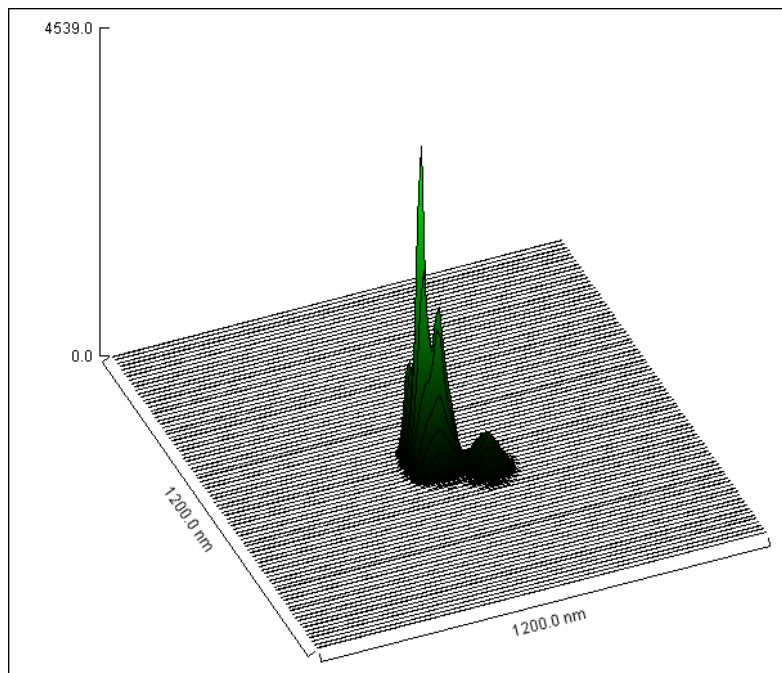
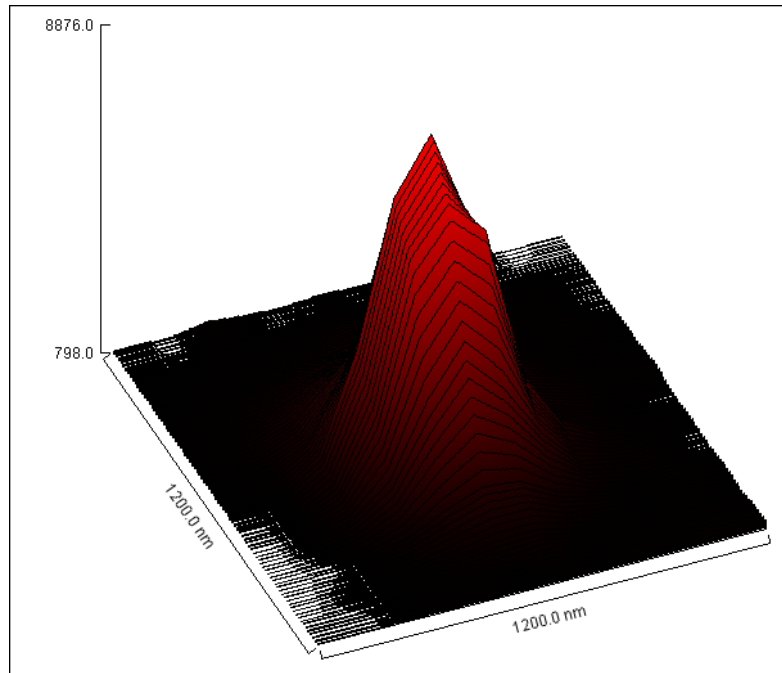


Figure 5.6 (cont.) | (c) PSF of the EGFR endosome in (b). The upper plot shows the PSF of the original 2-photon hologram scan image, and the lower plot is the the PSF of the PhILM super-resolution spots.

x (nm)	y (nm)	FWHM-x (nm)	FWHM-y (nm)	Distances (nm)
505.3	614.8	24.4	31.3	N/A
517.1	655.2	19.7	20.1	42.1
539.6	694.7	56.9	71.6	45.5
555.8	670.8	25.1	32.1	28.9
581.9	654.2	40.1	55.0	30.9
659.9	725.5	74.2	76.5	105.7

Table 5.1 | Two-dimensional localizations of the 6 receptors in the EGFR endosome marked in figure 5.6. Rows from top to bottom correspond to the localized spots in the endosome from left to right (Fig. 5.6b). From the FWHM we can tell the third and the sixth receptors may be out of focus, indicating they are actually located in other planes. The distances are the ones between two neighbor receptors.

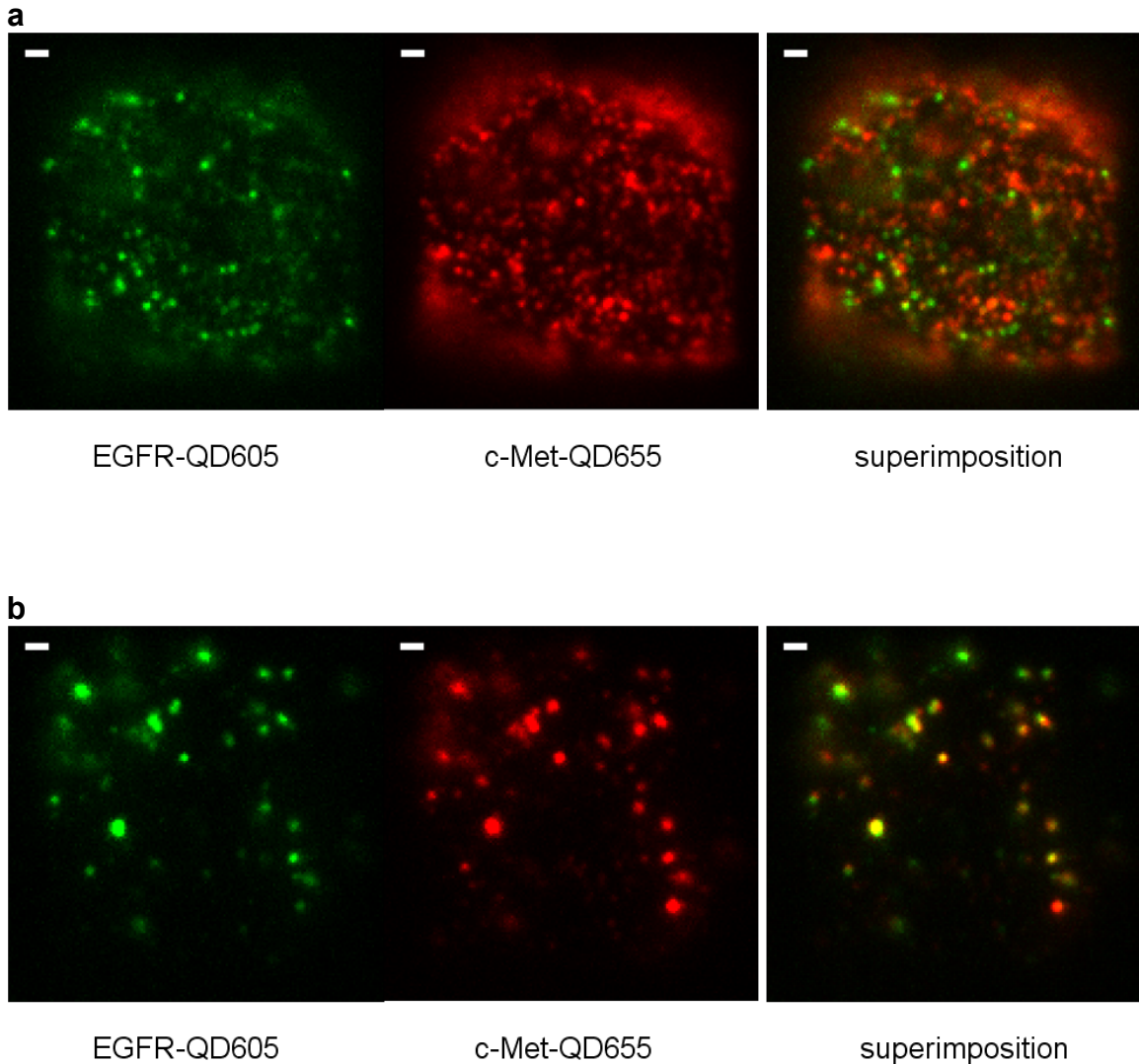


Figure 5.7 | Colocalization of EGFRs (ErbB-1) and HGFRs (c-Met) in fixed basal breast cancer cells. EGFRs are labeled with QD605 (green, artificial color) while c-Met are labeled with QD655 (red, artificial color). **(a)** Images of the two types of receptors in an unstimulated cell. Most EGFR and c-Met molecules distribute separately. **(b)** Images of the two types of receptors in a stimulated cell. After bound with and activated by EGF or HGF, the EGFR and the c-Met tend to traffic and co-localize in the same clusters.

# Chapter VI

## FIONA in 3D Space

### 6.1 Introduction

The invention of FIONA makes it possible to accurately localize a fluorescent spot in a two-dimensional space (x-y). Naturally, people would ask the question: how can we determine its z location, i.e. extend the FIONA to three dimensions? This question does not only come from the intrinsic curiosity of scientists, but also makes practical significance. For example, the *in vitro* motor protein tracking is restricted to near the surface of the glass coverslip and can be resolved by 2D FIONA with no question. But the real motion of a single motor protein, as well as the movement of the cargo driven by multiple motor proteins, is actually always three dimensional, which requires the ability of 3D tracking. Moreover, all complicated biological system, such as all cell samples and tissue samples, are three-dimensional. Therefore, many recently developed super-resolution techniques, e.g. PALM [17, 18]] and STORM [19-21], were all restricted to 2D at the beginning of their invention but required to be extended to 3D space. All these can be ascribed to 3D localization of individual fluorophores

So far a few ways to determine the z position of a fluorescent spot have been developed to extend FIONA to 3D. One is developed in our lab, by mathematically fitting the ring profile of the PSF of the defocused spot in a bifocal

image [31]. Figure 6.1 shows the scheme of the optical setup and an example bifocal image. The emission from the fluorophore is split into two channels, at 70 : 30 intensity ratio. The 30% of the emission goes through an additional lens (Lens-3 in the Fig. 6.1a) to be focused to the CCD, leaving the other 70% emission relatively out of focus. For a particular spot, the x-y position is determined by fitting the focused spot from the 30% emission with normal 2D FIONA. Its z position, however, is obtained by fitting the defocused spot to a new function which is essentially a Gaussian peak surrounded by a ring (for equation details see the caption of figure 6.1b). This technique has been successfully applied in 3D particle tracking.

Another example of 3D localization is shown in figure 6.2 [21]. Defocused spot images are also utilized to determine z locations. Instead of directly fitting the defocusing rings, researchers added a cylindrical lens into the optical path of the fluorescence emission, to create elongated spot images. Above or below the focal plane, the spot would stretch to different directions, one perpendicular to the other (Fig. 6.2a). With a standard sample (single Alexa 647 molecules), a calibration curve of the ellipticity of spots at various z planes was derived (Fig. 6.2b). By comparing the real data spots to the calibration curve, researchers could determine the z positions of the fluorophores.

The aforementioned methods to resolve z localization are satisfying in some cases, but still remain some disadvantages. First of all, the defocus of the fluorescence spots would lead to much broadened PSF and thus lower the localization accuracy. In the bifocal method, the split of the emission is a further

loss of the fluorescence emission that could have been used to obtain higher localization accuracy. For 3D STORM, the resolution rapidly gets worse when the spots are located at high displacement from the focal plane, so that, basically, only those within the  $\pm 600$  nm can be localized with satisfying accuracy. This weakness leads to the second limitation of all defocusing methods that their depths of imaging are still quite limited. The third drawback comes from the increasing complexity of the instrumentation required to accomplish the defocus imaging experiments. The setup in figure 6.1a requires dual channel view and an additional defocusing lens, whereas the configuration in figure 6.2a uses a cylindrical lens that is rarely used in routine biological laboratory microscopes. In this chapter of thesis, a new and more direct method to determine the z coordinate of a fluorescent spot is introduced. It does not utilize defocused images and therefore is capable of obtaining similar accuracy with 2D FIONA, and requires no additional lenses but only a typical 2-photon scan microscope.

## 6.2 Three-dimensional FIONA via 2-photon Sectioning

We extended FIONA to three dimensions when with 2-photon scan microscopy using single quantum dots. Significantly greater depth of field was achieved.

We analyzed single QD-605 nm in *E. coli* and QD-655 nm in breast cancer cells excited with 2P HM in 3D. We scanned at 100 nm scan step size and images were taken with 100 nm effective pixel size (after microscopic magnification) by an EMCCD. The 3D spot consisted of a stack of z slices, each

containing an x-y image. The x-y position of the spot can be easily localized by applying 2D FIONA [1]. We then established an x-z (keeping y fixed) or a y-z (keeping x fixed) image (Fig. 6.3) through the center of the brightest x-y image, and then applied 2D FIONA on the x-z or the y-z PSFs (see Methods for details). The plotted data point in figure 6.4a show the 3D positions of a QD-labeled EGF receptor in a representative breast cancer cell. Figure 6.4b shows that the statistical z accuracies found via the x-z or the y-z PSFs are  $3.1 \pm 1.4$  nm and  $3.0 \pm 1.2$  nm, respectively. For the x and y accuracies, we found  $2.0 \pm 0.9$  nm and  $1.9 \pm 0.9$  nm. As can be seen, the average z accuracy is slightly lower than x/y accuracies, by approximately 1 nm at the laser power used. This is expected because the PSF is slightly larger in the z dimension compared to the x-y dimension. Nevertheless, this indicates that we have < 3 nm accuracy in all three dimensions.

We also noticed that the x-y location in different z sections had some drift, likely due to mechanical movement of the microscope stage while scanning. In the data shown in figure 6.5 (red), with >400 nm scan range in z direction, the x-y mechanical drift amounts to about 30 nm for a spot in the fixed breast cancer cell, or up to 100 nm in the live *E.coli* cell. We calibrated the drift via fiduciary markers and reduced it to 5~15 nm (blue).

### 6.3 Discussion

The 3D FIONA uses not the defocused spots but the created in-focus spots in the virtual pixelated x-z or y-z imaging planes extracted from the

sectioned image stack taken by 2-photon 3D scan. The intrinsic sectioning imaging along z axis of the scan microscopy offers the information about the z positions of the fluorophores. Discrete stepping along z direction makes the pixelation of the virtual x-z and y-z imaging planes, and the z step size is naturally the pixel size in z coordinate.

The localization accuracy in z direction of 3D FIONA is comparable to the x-y localization as it does not split the emission and thus lose no photons. Also, in 2-photon scan microscopy, the imaging focal plane always moves along with the z scan, so there is no restriction of the z displacement that it can accurately measure, which is much limited in alternative 3D localization methods [21, 31]. In other words, the localization depth of 3D FIONA is very large, theoretically equal to the imaging depth of the 2-photon scan microscope, around a couple of millimeters.

Furthermore, 3D FIONA finds the base to extend PhILM from 2D to 3D. PhILM, unlike STORM or PALM, uses images that have dense fluorophores in “on” state in a big part of the movie length (photobleaching data such as organic dyes) or throughout the time-lapse data (blinking data such as quantum dots images), so that the background is much higher. In this case, the defocused spot, elliptic or with outer rings, may be easily inundated by the background of focused spots. The 3D FIONA can avoid this danger and generate 3D super-resolution images better resolved in z direction.

## 6.4 Methods

*3D FIONA data analysis:* Detailed description about the 2D-FIONA, can be found in the Yildiz et al paper [1]. Localization accuracy is the standard error of the mean of the center of the Point Spread Function (PSF). For 3D FIONA, the extraction of yz or xz PSF was described in the article. Two adjacent z sections are separated by 100 nm. The localization in z axis was done by fitting the yz or xz PSF to the standard Gaussian functions [1], or fitting 1D z PSF to 1D Gaussian fit. Residuals were plotted and calculated. They showed the fitting of yz/xz/z PSF to Gaussian function were excellent. All analysis was run by in-lab written programs in IDL or MatLab. Getting x-y location ( $x_0, y_0$ ) with nanometer accuracy was done by applying standard 2D FIONA on the PSF in the brightest z slice. To accurately localize the z coordinate of the 3D spot, we established a virtual x-z slice in the PSF and by found the x-z plane through the constant  $y_0$  and extracting intensities on all pixels in the plane. Similarly, a y-z PSF could be drawn. Moreover, we established a z-only one-dimensional PSF by extracting all z pixels at the constant point ( $x_0, y_0$ ). Then we fit x-z and y-z PSF to 2D Gaussian and z-only PSF to 1D Gaussian. Analysis of variance (ANOVA) showed no significant difference in the z localizations determined via the three kinds of PSFs above, as expected from theory.

## 6.5 Figures

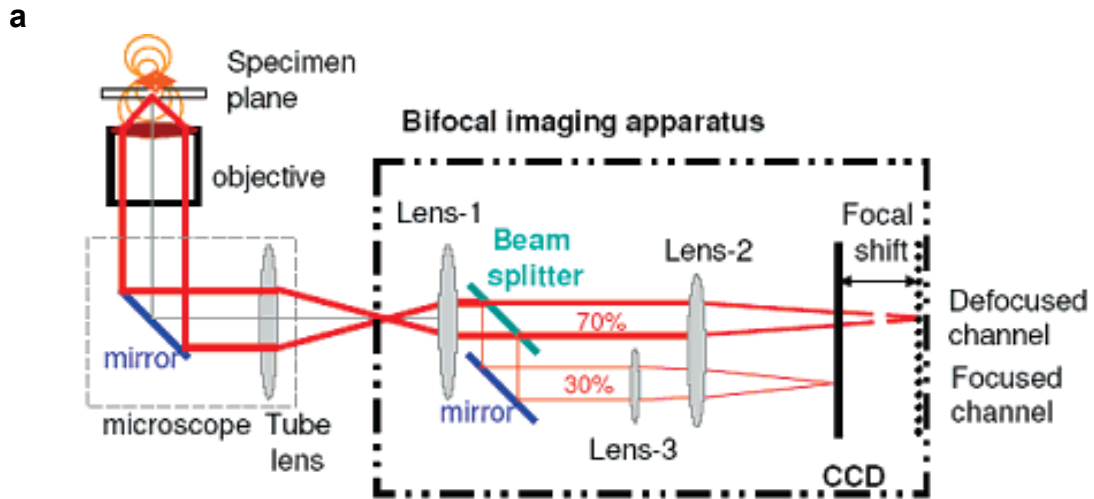


Figure 6.1 | (a) Schematic of the bi-focal microscope. The distance that the delayed focal plane is relatively off the original focal plane is determined by the focal length of lens-3.

**b**

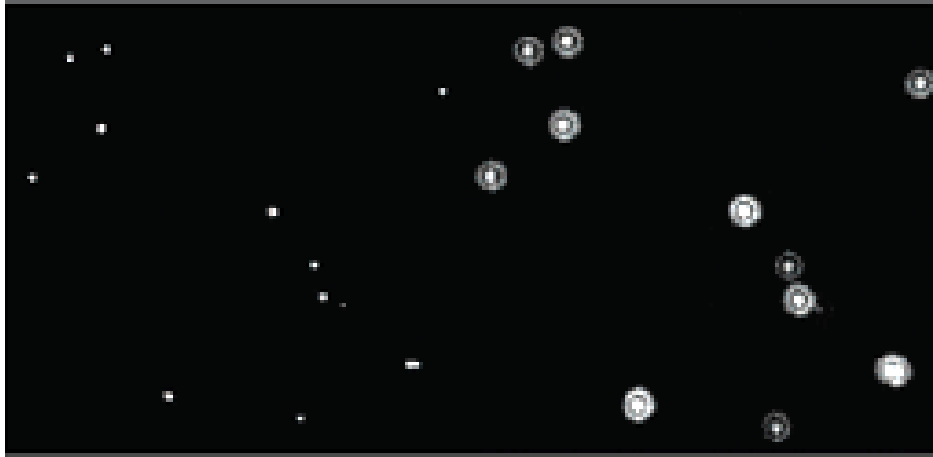


Figure 6.1 (cont.) | **(b)** A typical bi-focal image of 200 nm fluorescent beads. The defocused spots are fitted with  $Z = P_0 + P_1 \cdot \exp[-P_2 \cdot ((x - x_0)^2 + (y - y_0)^2)] + P_3 \cdot \exp[-P_4 \cdot (((x - x_0)^2 + (y - y_0)^2)^{1/2} - R_0)^2]$ , which is essentially a single Gaussian peak surrounded by a circle with radius =  $R_0$ , which depends the z displacement from the focal plane. The (x,y) position of the particle can be derived from 2D Gaussian fitting of the corresponding focused spots in the focused image, or determined from fitting the defocused spots with the above equation and getting  $x_0$  and  $y_0$ . Reasonably, Gaussian fit to focus images gives 2-fold higher accuracy.

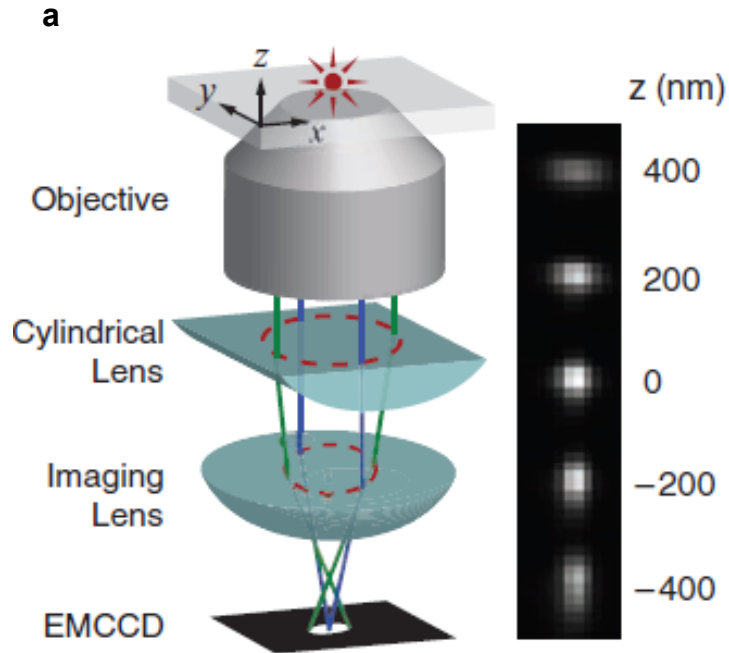


Figure 6.2 | The configuration of 3D STORM. (a) Scheme of the setup and typical images of individual fluorophores located at various  $z$  planes. The added cylindrical lens elongated the defocused spots, in two perpendicular directions for the spots above or below the focal plane. The ellipticity of standard samples (single Alexa 647 molecules) can be calibrated as a function of  $z$  displacement to the focal plane

**b**

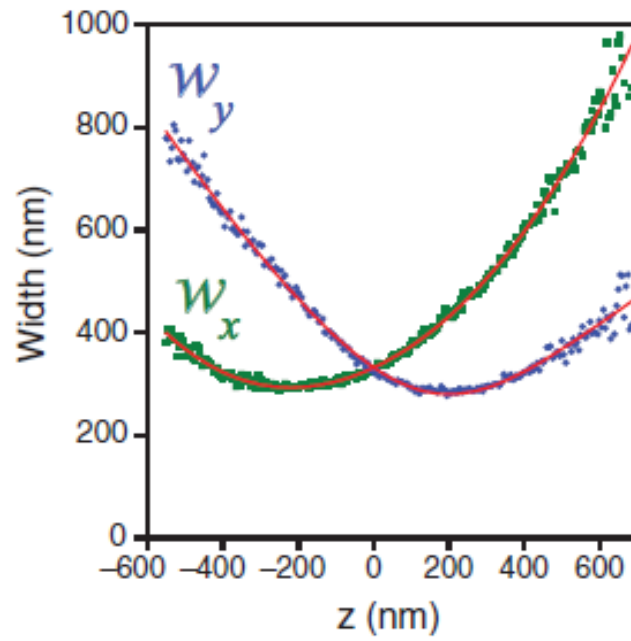


Figure 6.2 (cont.) | **(b)**. Then the  $z$  position of a spot from the real sample can be determined by fit to the calibration curve.

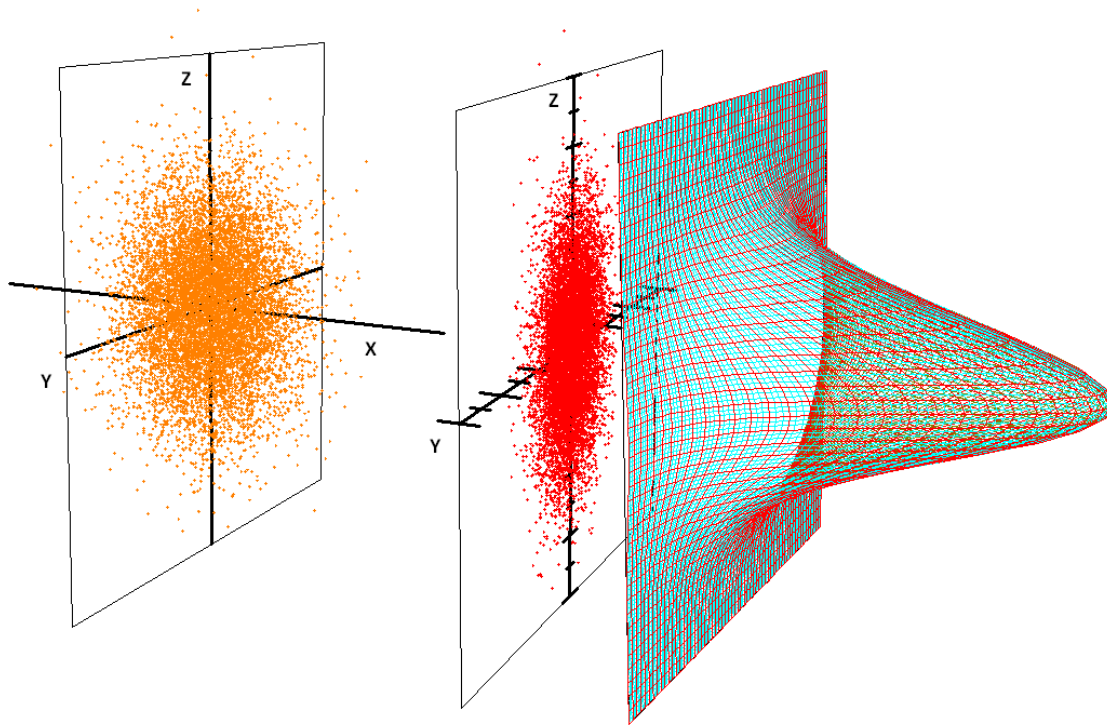


Figure 6.3 | A simulation of emitted photon distribution of a single quantum dot in 3D space (left, yellow dots), its projection on yz plane (middle, red dots) and the Gaussian Fit of the drawn virtual 2D yz point spread function (right, mesh plot).

a

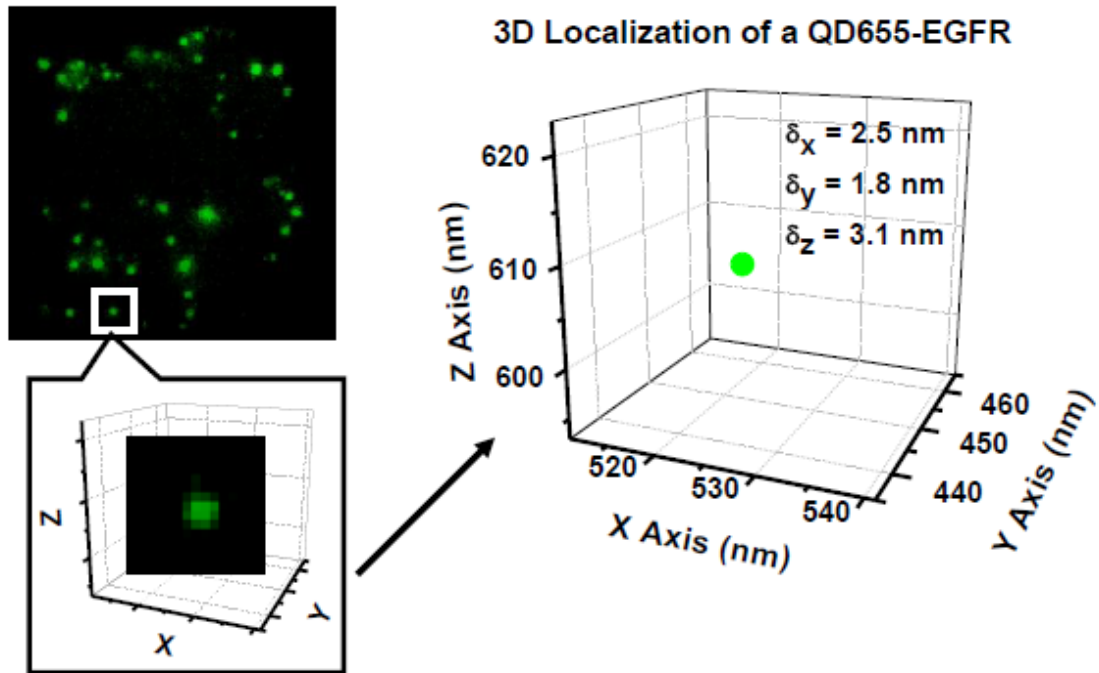


Figure 6.4 | 3D FIONA of single QDs. (a) A QD655-labeled EGF receptor in a breast cancer cell localized in 3D space.

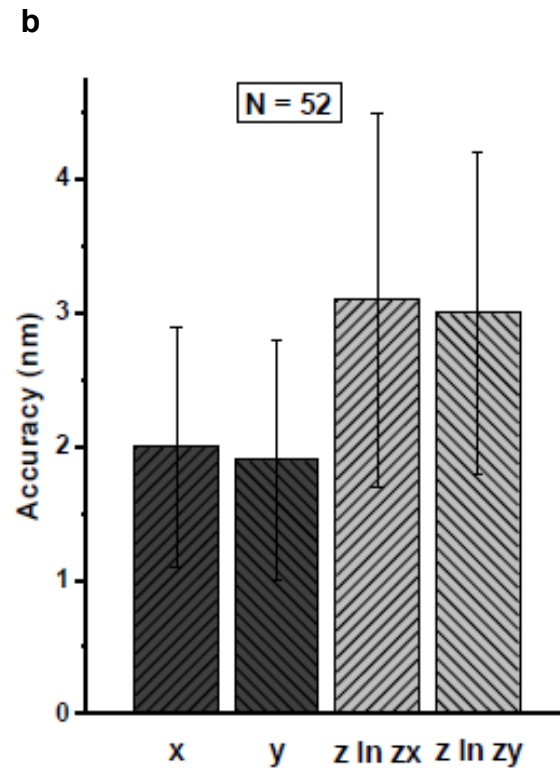
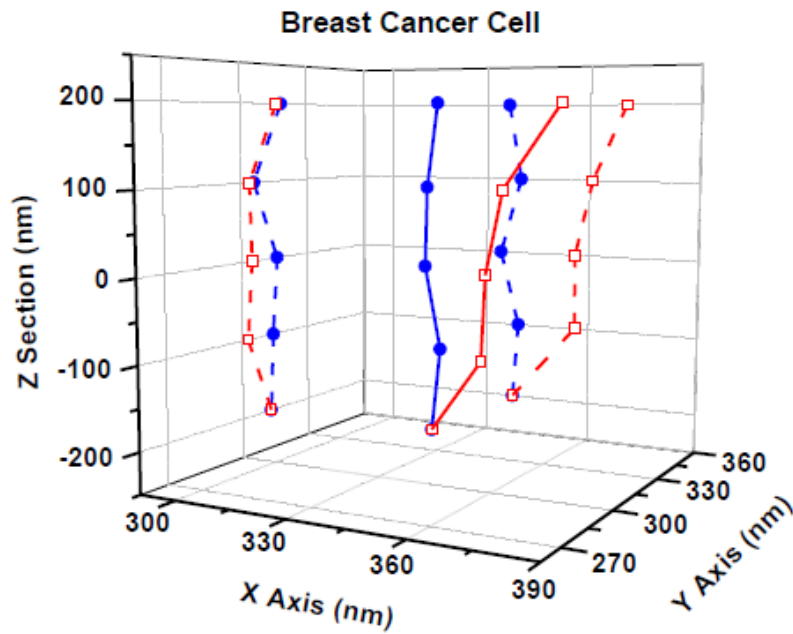


Figure 6.4 (cont.) | (b) In a 3D FIONA fitting, the average z accuracy is usually slightly lower than the average x and y accuracies.

a



b

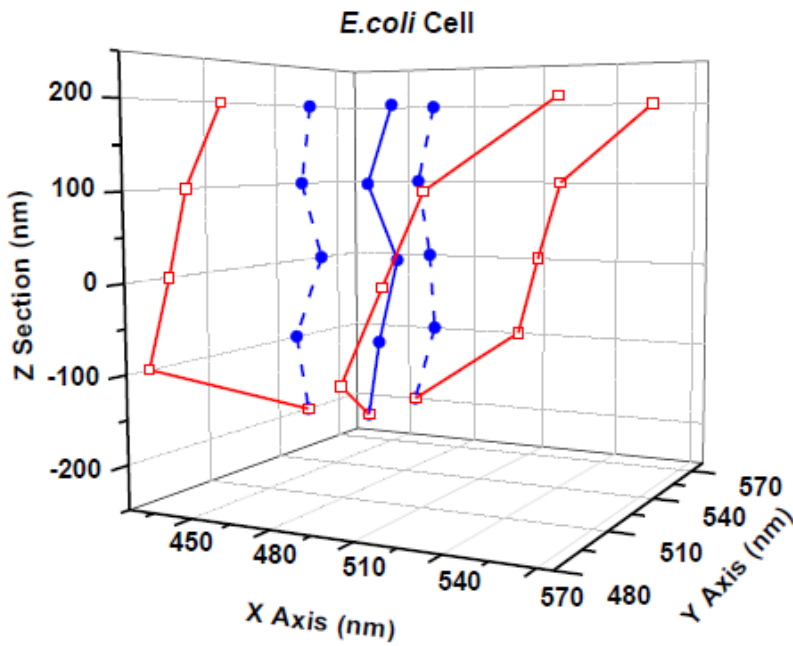


Figure 6.5 | The xy localizations of two single quantum dot labeled receptors in a fixed breast cancer cell (a) and living *E.coli* cell (b), before (red squares) and after (blue spheres) drift calibration in different z sections (solid) and projections (dash) in x-z and y-z planes.

## References

1. Yildiz, A., et al., *Myosin V Walks Hand-Over-Hand: Single Fluorophore Imaging with 1.5-nm Localization*. Science, 2003. **300**: p. 2601-2605.
2. Yildiz, A., et al., *Kinesin Walks Hand-Over-Hand*. Science, 2004. **303**: p. 676-678.
3. Yildiz, A., et al., *Myosin VI steps via a hand-over-hand mechanism with its lever arm undergoing fluctuations when attached to actin*. J. Biol. Chem., , 2004. **279**: p. 37223-37226.
4. Kural, C., et al., *Kinesin and Dynein Move a Peroxisome in Vivo: A Tug-of-War or Coordinated Movement?* . Science, 2005. **308**(5727): p. 1469-1472.
5. Tan, E., et al., *A Four-way Junction Accelerates Hairpin Ribozyme Folding via a Discrete Intermediate*. Proceedings of National Academy of Science, 2003. **100**(16): p. 9308.
6. Myong, S., I. Rasnik, C. Joo, T. M. Lohman, and T. Ha., *Repetitive Shuttling of a Motor Protein on DNA*. Nature, 2005. **437**: p. 1321-1325.
7. Myong, S., et al., *Spring-loaded Mechanism of DNA Unwinding by HCV NS3 Helicase*. Science, 2007. **317**: p. 513-516.
8. Wang, Y., et al., *Visualization of Mechanical Activation of Src*. Nature, 2005. **434**: p. 1040.
9. Wang, Y., S. Y.J, and S. Chien, *Fluorescence Proteins, Live Cell Imaging, and Mechanobiology: Seeing is Believing*. Annual Review of Biomedical Engineering, 2008. **10**: p. 1-38.
10. Nguyen, Q.T., et al., *Surgery with molecular fluorescence imaging using activatable cell-penetrating peptides decreases residual cancer and improves survival*. Proceedings of National Academy of Science, 2010. **107**: p. 4317-4322.
11. Hirschfeld, T., *Optical microscopic observation of single small molecules*. Appl. Opt., 1976. **15**(5): p. 2965-2966.
12. Moerner, W.E. and L. Kador, *Optical detection and spectroscopy of single molecules in a solid*. Phys. Rev. Lett. , 1989. **62**: p. 2535-2538.
13. Orrit, M. and J. Bernard, *Single pentacene molecules detected by fluorescence excitation in a p-terphenyl crystal*. Phys. Rev. Lett. , 1990. **65**, **2716-9(1990)**: p. 2716-2719.

14. Shera, E.B., et al., *Detection of single fluorescent molecules*. Chem. Phys. Lett., 1990. **174**: p. 553-557.
15. Peterman, E.J.G., H. Sosa, and M.W. E., *Single-molecule fluorescence spectroscopy and microscopy of biomolecular motors*. Annu. Rev. Phys. Chem., 2004. **55**: p. 79-96.
16. Weiss, S., *Fluorescence spectroscopy of single biomolecules*. Science 1999. **283**: p. 1676-1683.
17. Betzig, E., et al., *Imaging intracellular fluorescent proteins at nanometer resolution*. Science, 2006. **313**: p. 1642-1645.
18. Hess, S.T., T.P.K. Girirajan, and M.D. Mason, *Ultra-High Resolution Imaging by Fluorescence Photoactivation Localization Microscopy*. Biophysical journal, 2006. **91**(11): p. 4258-4272.
19. Rust, M.J., M. Bates, and X. Zhuang, *Sub-diffraction-limit imaging by stochastic optical reconstruction microscopy (STORM)*. Nature Methods, 2006. **3**: p. 793-796.
20. Bates, M., et al., *Multicolor super-resolution imaging with photo-switchable fluorescent probes*. Science, 2007. **317**: p. 1749-1753.
21. Huang, B., et al., *Three-Dimensional Super-Resolution Imaging by Stochastic Optical Reconstruction Microscopy*. Science, 2008. **319**(5864): p. 810-813.
22. Simonson, P.D., E. Rothenberg, and P.R. Selvin, *Super-resolution without single-molecule imaging*. Nature Methods, Submitted.
23. Funatsu, T., et al., *Imaging of single fluorescent molecules and individual ATP turnovers by single myosin molecules In aqueous solution*. Nature, 1995. **374**: p. 555-559.
24. Moerner, W.E. and D.P. Fromm, *Methods of single-molecule fluorescence spectroscopy and microscopy*. Rev. Sci. Instrum., 2003. **74**: p. 74, 3597-3619.
25. Ambrose, W.P., P.M. Goodwin, and J.P. Nolan, *Single-molecule detection with total internal reflection excitation: Comparing signal-to-background and total signals in different geometries*. Cytometry, 1999. **36**(224-231).
26. Gordon, M.P., T. Ha, and P.R. Selvin, *Single Molecule High Resolution Imaging with Photobleaching*. Proceedings of National Academy of Science, 2004. **101**: p. 6462-6465.

27. Churchman, L.S., et al., *Single molecule high-resolution colocalization of Cy3 and Cy5 attached to macromolecules measures intramolecular distances through time*. PNAS, 2005. **102**(5): p. 1419-1423.
28. Bobroff, N., *Position Measurement with a resolution and noise-limited instrument*. Rev. Sci. Instrum. , 1986. **57**: p. 1152-1157.
29. Thompson, R.E., D.R. Larson, and W.W. Webb, *Precise nanometer localization analysis for individual fluorescent probes*. Biophysics Journal, 2002. **82**(5): p. 2775-2783.
30. Kural, C., et al., *Tracking melanosomes inside a cell to study molecular motors and their interaction*. Proceedings of National Academy of Science, 2007. **104**: p. 5378-5382.
31. Toprak, E., et al., *Three-Dimensional Particle Tracking via Bifocal Imaging*. Nano Letters, 2007. **7**(7): p. 2043-2045.
32. Denk, W., J.H. Strickler, and W.W. Webb, *Two-Photon Laser Scanning Fluorescence Microscopy*. Science, 1990. **248**(4951): p. 73-76.
33. Smith, A.E. and A. Helenius, *How Viruses Enter Animal Cells*. Science, 2004. **304**(5668): p. 237-242.
34. Marsh, M. and A. Helenius, *Virus entry: open sesame*. Cell, 2006. **124**(4): p. 729-740.
35. Mudhakar, D. and H. Harashima, *Learning from the Viral Journey: How to Enter Cells and How to Overcome Intracellular Barriers to Reach the Nucleus*. AAPS Journal, 2009. **11**(1): p. 65-77.
36. Skehel, J.J. and D.C. Wiley, *Receptor binding and membrane fusion in virus entry: the influenza hemagglutinin*. Annual Review of Biochemistry, 2000. **69**: p. 531-569.
37. Dimitrov, D.S., *Virus entry: molecular mechanisms and biomedical applications*. Nature Review Microbiology, 2004. **2**(2): p. 109-122.
38. Li, E., et al., *Adenovirus endocytosis requires actin cytoskeleton reorganization mediated by Rho family GTPases*. The Journal of Virology, 1998. **72**: p. 8806.
39. Schwartz, M., *Reversible interaction between coliphage lambda and its receptor protein*. Journal of Molecular Biology, 1975. **99**(1): p. 185-201
40. Schwartz, M., *The adsorption of coliphage lambda to its host: effect of variations in the surface density of receptor and in phage-receptor affinity*. Journal of Molecular Biology, 1976. **103**(3): p. 521-536.

41. Luria, S.E. and M. Delbrück, *Mutations of Bacteria from Virus Sensitivity to Virus Resistance*. Genetics, 1943. **28**(6): p. 491-511.
42. Berg, H.C. and E.M. Purcell, *Physics of chemoreception*. Biophysical Journal, 1977. **20**(2): p. 193-219.
43. Berkane, E., et al., *Interaction of bacteriophage lambda with its cell surface receptor: an in vitro study of binding of the viral tail protein gpJ to LamB (Maltoporin)*. Biochemistry, 2006. **45**(8): p. 2708-2720.
44. Moldovan, R., E. Chapman-McQuiston, and X.L. Wu, *On kinetics of phage adsorption*. Biophysical journal, 2007. **93**: p. 303-315.
45. Wang, J., et al., *Cloning of the J gene of bacteriophage lambda, expression and solubilization of the J protein: first in vitro studies on the interactions between J and LamB, its cell surface receptor*. Research in Microbiology, 1998. **149**(9): p. 611-624.
46. Edgar, R., et al., *Bacteriophage infection is targeted to cellular poles*. Molecular Microbiology, 2008. **68**(5): p. 1107-1116.
47. Rothenberg, E., et al., *Viral Target-Finding via Receptor-Dependent Spatial Focusing*. In preparation.
48. Idbaih, A., et al., *Therapeutic Application of Noncytotoxic Molecular Targeted Therapy in Gliomas: Growth Factor Receptors and Angiogenesis Inhibitors*. The Oncologist, 2008. **13**(9): p. 978-992.
49. Driel, A.F.V., *Frequency-Dependent Spontaneous Emission Rate from CdSe and CdTe Nanocrystals: Influence of Dark States*. Physical Review Letters, 2005. **95**(23): p. 236804.
50. Walling, M.A. and S. Novak, *Quantum Dots for Live Cell and In Vivo Imaging*. International Journal of Molecular Sciences, 2009. **10**(2): p. 441-491.
51. Tokumasu, F., et al., *Band 3 modifications in Plasmodium falciparum-infected AA and CC erythrocytes assayed by autocorrelation analysis using quantum dots* Journal of Cell Science, 2005. **118**: p. 1091-1098.
52. Dahan, M., et al., *Diffusion Dynamics of Glycine Receptors Revealed by Single-Quantum Dot Tracking* Science, 2003. **302**(5644): p. 442-445.
53. Howarth, M., et al., *Monovalent, reduced-size quantum dots for imaging receptors on living cells*. Nature Methods, 2008. **5**(5): p. 397-399.
54. Akerman, M., et al., *Nanocrystal targeting in vivo*. Proceedings of the National Academy of Sciences, 2002. **99**(20): p. 12617-12621.

55. Dwarakanath, S., et al., *Quantum dot-antibody and aptamer conjugates shift fluorescence upon binding bacteria*. Biochemical and biophysical research communications, 2004. **325**(3): p. 739-743.
56. Ballou, B., et al., *Noninvasive imaging of quantum dots in mice*. Bioconjugate chemistry, 2004. **15**(1): p. 79-86.
57. Chan, W.C.W. and S. Nie, *Quantum Dot Bioconjugates for Ultrasensitive Nonisotopic Detection* Science, 1998. **281**(5385): p. 2016-2018.
58. Michalet, X., et al., *Quantum Dots for Live Cells, in Vivo Imaging, and Diagnostics* Science, 2005. **307**(5709): p. 538-544.
59. Rothenberg, E., et al., *Two-Photon Fluorescence Microscopy of Single Semiconductor Quantum Rods: Direct Observation of Highly Polarized Nonlinear Absorption Dipole*. Journal of Physical Chemistry B, 2004. **108**(9): p. 2797-2800.
60. Verberk, R., A.M.v. Oijen, and M. Orrit, *Simple model for the power-law blinking of single semiconductor nanocrystals*. Physical Review B, 2002. **66**(23): p. 233202.
61. Sanchez, E.J., et al., *Room-Temperature Fluorescence Imaging and Spectroscopy of Single Molecules by Two-Photon Excitation*. The journal of Physical Chemistry C, 1997. **101**(38): p. 7019-7023.
62. Mertz, J., C. Xu, and W.W. Webb, *Single-molecule detection by two-photon-excited fluorescence*. Optics Letters, 1995. **20**(24): p. 2532-2534.
63. Larson, D.R., et al., *Water-Soluble Quantum Dots for Multiphoton Fluorescence Imaging in Vivo*. Science, 2003. **300**(5624): p. 1434-1436.
64. Nirmal, M., et al., *Fluorescence intermittency in single cadmium selenide nanocrystals*. Nature, 1996. **383**: p. 802-804.
65. Mehta, A.D., et al., *Myosin-Vis a processive actin-based motor*. Nature, 1999. **400**: p. 590-593.
66. Tokunaga, M., N. Imamoto, and K. Sakata-Sogawa, *Highly inclined thin illumination enables clear single-molecule imaging in cells*. Nature Methods, 2008. **5**(2): p. 159-161.
67. Niesner, R., et al., *The Power of Single and Multibeam Two-Photon Microscopy for High-Resolution and High-Speed Deep Tissue and Intravital Imaging*. Biophys Journal, 2007. **93**(7): p. 2519-2529.

68. Oddershede, L., et al., *The Motion of a Single Molecule, the  $\lambda$ -Receptor, in the Bacterial Outer Membrane*. Biophysical Journal, 2002. **83**(6): p. 3152-3161.
69. Guo, A., et al., *Signaling networks assembled by oncogenic EGFR and c-Met*. Proceedings of National Academy of Science, 2008. **105**(2): p. 692-697.
70. Massie, C. and I.G. Mills, *The developing role of receptors and adaptors*. Nature Reviews Cancer, 2006. **6**: p. 403-409
71. McShane, M.P. and M. Zerial, *Survival of the weakest: signaling aided by endosomes*. The Journal of Cell Biology, 2008. **182**(5): p. 823 -825.
72. Chung, I., et al., *Spatial control of EGF receptor activation by reversible dimerization on living cells*. Nature, 2010. **464**: p. 783-787.
73. Clayton, A.H.A., et al., *Ligand-induced Dimer-Tetramer Transition during the Activation of the Cell Surface Epidermal Growth Factor Receptor-A Multidimensional Microscopy Analysis*. The Journal of Biological Chemistry, 2005. **280**(34): p. 30392-30399.
74. Webb, S.E.D., et al., *Single-Molecule Imaging and Fluorescence Lifetime Imaging Microscopy Show Different Structures for High- and Low-Affinity Epidermal Growth Factor Receptors in A431 Cells*. Biophys Journal, 2008. **94**(3): p. 803-819.
75. Bates, M., T.R. Blosser, and X. Zhuang, *Short-range spectroscopic ruler based on a single-molecule optical switch*. Physical Review Letters, 2005. **94**: p. 108101-108104.
76. Shaner, N.C., G.H. Patterson, and M.W. Davidson, *Advances in fluorescent protein technology*. Journal of Cell Science, 2007. **120**,: p. 4247-4260.
77. Moneron, G. and S.W. Hell, *Two-photon excitation STED microscopy*. Optics Express, 2009. **17**: p. 14567-14573.
78. Lidke, K., et al., *Superresolution by localization of quantum dots using blinking statistics*. Optics Express, 2005 **13**(18): p. 7052-7062.
79. Lagerholm, B.C., et al., *Analysis Method for Measuring Submicroscopic Distances with Blinking Quantum Dots*. Biophysical Journal, 2006. **91**(8):p. 3050-3060
80. Lidke, D.S., et al., *Quantum dot ligands provide new insights into erbB/HER receptor-mediated signal transduction*. Nature Biotechnology, 2004. **22**(2): p. 198-203.